UNIVERSITY OF PRETORIA

Investigating electron-transfer processes of supramolecular donor-acceptor complexes using femtosecond transient absorption spectroscopy

By:

Mr. Arthur J. Harrison

Submitted in partial fulfilment of the requirements for the degree

Magister Scientae

In the Faculty of Natural & Agricultural Sciences

University of Pretoria

Pretoria

Supervisor: Prof. Tjaart P.J. Krüger

Co-Supervisor: Dr. S. G. Radhakrishnan

February 11, 2019

Declaration of Authorship

I, Mr. Arthur J. Harrison , declare that the dissertation, which I hereby submit for the degree Magister Scientae at the University of Pretoria, is my own work and has not previously been submitted by me for a degree at this or any other tertiary institution.

Signed:

_____

Date:

_____

"There are photons that have been travelling for 30,000 years, and I'm... snatching them from this journey and planting them into my digital detector. And then I started feeling bad for the photon, and I said maybe it wanted to continue but I got in its way. But then I said, no, those are probably happier photons than the one that slammed into the mountainside that will go unanalysed and will not contribute to the depth of our understanding of the universe."

Neil deGrasse Tyson

Acknowledgements

I would like to express my utmost gratitude to my supervisors, Prof. Tjaart Krüger and Dr. Shankara Radhakrishnan for providing me with this opportunity and for supporting and guiding me through some of the challenges which I faced. I would also like to thank the biophysics team for their insightful discussions and assistance, especially Mr. Huzifa Elnour for taking the time to teach me everything I know about femtosecond laser spectroscopy. I would also like to acknowledge the Council for Scientific and Industrial Research and the Department of Science and Technology for their invaluable funding. Lastly, I would like to thank my family and friends for their unconditional love and support over the years.

Contents

List of Figures

List of Tables

List of Abbreviations

BO	**B**orn **O**ppenheimer
CPA	**C**hirped **P**ulse **A**mplification
CR	**C**harge **R**ecombination
CS	**C**harge **S**eparation
DFT	**D**ensity **F**unctional **T**heory
EM	**E**lectro**m**agnetic
ESA	**E**xcited **S**tate **A**bsorption
ET	**E**lectron **T**ransfer
FTAS	**F**emtosecond **T**ransient **A**bsorption **S**pectroscopy
GSB	**G**round **S**tate **B**leach
GUI	**G**raphical **U**ser **I**nterface
GVD	**G**roup **V**elocity **D**ispersion
HOMO	**H**ighest **O**ccupied **M**olecular **O**rbital
IR	**I**nfra **R**ed
ISC	**I**nter **S**ystem **C**rossing
JD	**J**ablonski **D**iagram
LUMO	**L**owest **U**noccupied **M**olecular **O**rbital
NDF	**N**eutral **D**ensity **F**ilter
NOPA	**N**oncolinear **O**ptical **P**arametric **A**mplification
OD	**O**ptical **D**ensity
PA	**P**roduct **A**bsorption
SE	**S**timulated **E**mission
SFG	**S**um **F**requency **G**eneration
SHG	**S**econd **H**armonic **G**eneration
SNR	**S**ignal to **N**oise **R**atio
SPM	**S**elf **P**hase **M**odulation
THG	**T**hird **H**armonic **G**eneration
TPP	**T**etra**p**enyl**p**orphyrin
WL	**W**hite **L**ight
XPM	**C**ross **P**hase **M**odulation
ZnTPP	**Z**inc **T**etra**p**enyl**p**orphyrin

For Melissa and my parents, Arthur & Henda.

Abstract

A femtosecond transient absorption spectroscopy system was developed and used to characterize the charge-transfer processes which take place between photo-excited porphyrin and C_{60}-fullerene supramolecular donor-acceptor complexes, specifically the free-base (TPP) and zinc metal porphyrins (ZnTPP). A comprehensive photophysical characterization of the TPP-C_{60} and ZnTPP-C_{60} complexes, along with the individual moieties, was performed which included ground-state absorption, steady-state fluorescence, and femtosecond transient absorption spectroscopic data, from which Jablonski diagrams and kinetic models could be constructed. The electron transfer processes were monitored along spectral traces at 1000 nm in the difference absorption spectra, where the $C_{60}^{-\bullet}$ anion appears. Upon photo-excitation at 387.5 nm with pulses of 150 fs time-duration and pump beam fluency of 1.02 mJ/cm^2, the kinetic rates of charge-separation (κ_{CS}) from donor to acceptor were determined to be 8.3×10^{11} s^{-1} (1.2 ps) and 5.5×10^{11} s^{-1} (1.8 ps) for the TPP-C_{60} and ZnTPP-C_{60} complexes, respectively. Charge-recombination (κ_{CR}) rates from the acceptor to donor were 8.4×10^{9} s^{-1} (119 ps) and 5.4×10^{9} s^{-1} (183 ps) for the TPP-C_{60} and ZnTPP-C_{60} complexes, respectively. The ratio of charge-separation and charge-recombination kinetic rates (κ_{CS}/κ_{CR}) exceeded 100 for both TPP-C_{60} and ZnTPP-C_{60} complexes, showing that these simple, self-assembled, supramolecular complexes have the ability to extend the process of charge-recombination after fast separation, a key characteristic necessary for an effective solar cell.

Chapter 1

Introduction

One of the most pressing issues facing the current and future population is the global energy crisis, which broadly speaking refers to three main questions:
"Will we run out of energy?",
"How secure is our access to energy?",
"How does climate change affect the energy we use?".
Rapid population growth, a dwindling supply of easily accessible fossil fuels and global warming associated with burning fossil fuels are main reasons for a strong global transition towards clean, renewable and sustainable energies [1–4]. The challenge of providing clean, renewable and sustainable energy can only be accomplished through extensive academic research, global collaborations which will eventually lead to innovation at an industrial scale. Apart from fossil fuels, there are a number of alternative energy sources such as solar, wind, geothermal, hydroelectric, but there is only one truly inexhaustible source of energy available on earth which is solar energy. The broad spectrum of photons emitted by the sun has shaped and moulded life on Earth - through the process of photosynthesis over billions of years, which has inspired humankind to mimic nature giving birth to the field of artificial photosynthesis which has been a major topic of interest over the past two decades [5–7]. Understanding the fundamental process and mechanisms of

the natural photosynthetic process holds the key to unlocking the true potential of harvesting limitless amounts of solar energy. In the following section, the photophysical properties and unique characteristics of carbon-based fullerene, free-base and metal porphyrins are introduced within the context of artificial light-harvesting. Specifically, in the form of donor and acceptor supramolecular organic systems, inspired by the charge-separation processes that occur in the main light-harvesting complex LHCII.

In the next section, a mathematical description of femtosecond (fs) light pulses is provided with specific attention to spectral and temporal features. The important physics applicable to light-matter interactions most relevant to femtosecond transient absorption spectroscopy (FTAS) will be made clear to the reader. The aim is to explain the important photophysical events preceding a spectroscopic measurement and to provide a general mathematical interpretation where necessary.

1.1 The Physics of Light-Matter Interactions

1.1.1 Electromagnetic Waves

The simple definition of a *wave* is a periodic oscillation that transmits energy through space that can be characterized by wavelength ($\lambda = 2\pi/\kappa$), frequency ($\nu = \omega/2\pi$) and amplitude (A).

$$f(x) = Acos(\kappa x - \omega t + \delta) \tag{1.1}$$

Where κ is the wavenumber, ω the angular frequency and δ the phase term. Sound waves propagate energy through space in the form of periodic oscillations caused by the compression of matter. In contrast, energy that propagates in the vacuum is known as electromagnetic (EM) radiation and has a constant velocity ($c = 2.99792458$ m·s^{-1}). The electromagnetic spectrum defines the energy of all possible EM radiation and ranges from high-frequency gamma radiation to the lowest frequency radio-waves (figure 1.1). Light quanta, or photons, are elementary particles that exhibit both wave (diffraction and interference) and particle (Compton scattering and the photo-electric effect) properties and are quantitatively expressed

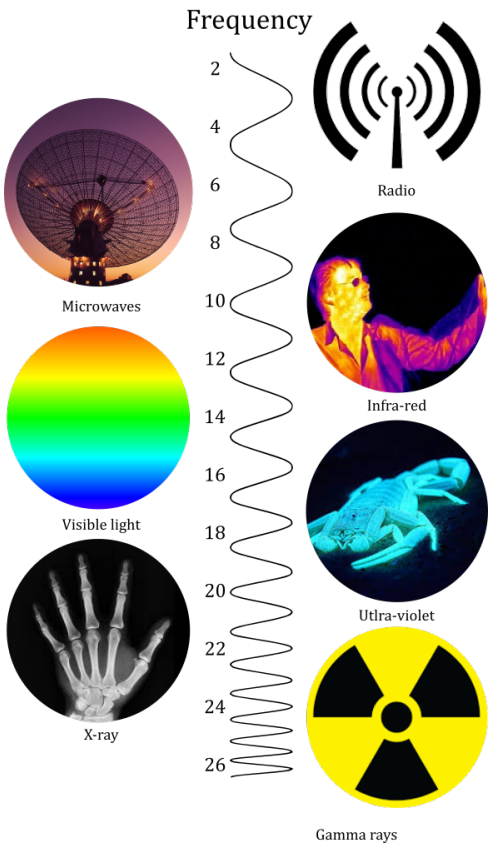

FIGURE 1.1: The electromagnetic spectrum. The numbers on the vertical axis represent the order of magnitude (x10^p).

through the energy $E = h\nu$ and momentum $P = \frac{h}{\lambda}$ relations, where h is Planck's constant. The periodic oscillation of individual monochromatic photons (single oscillating frequency) can be coherently superimposed such that constructive and destructive interference leads to a linear combination of individual oscillation frequencies producing a single wave packet (figure 1.2). Pulses or wave packets, in general, are characterized by the frequency range of constituent photons, and by the duration of the pulse in time. These two characteristics are often referred to as the frequency bandwidth ($\Delta\nu$) and the temporal bandwidth ($\Delta\tau$), respectively, and their product is constrained by Heisenberg's uncertainty principle:

$$\Delta\nu\Delta\tau \geq K$$

If a wave packet consists of a very broad frequency range ($\Delta\nu \sim large$) then the uncertainty principle states that the time duration must be appropriately small since K is a fixed value. K is a constant and is unique for every transform-limited pulse shape.

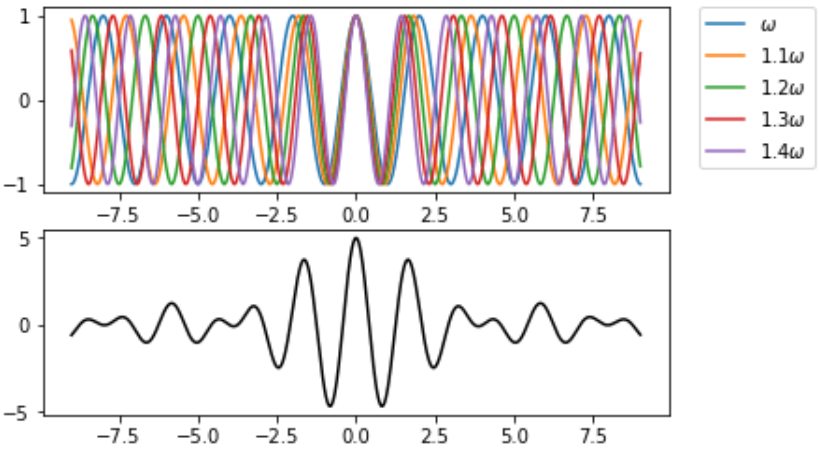

FIGURE 1.2: Linear combination of harmonic waves of varying angular frequencies (top), coherently superimposed to produce a localized wave packet (bottom). The ω units are arbitrary, i.e. $\omega = 1$.

The Wave Equation

A fs time-duration pulse is an EM wave and as such can be fully characterized in both time and space by a *wave function* that satisfies Maxwell's second order partial differential wave equation. A propagating wave can be fully visualized using the harmonic wave function (equation 1.1) and although simple and elegant, the harmonic description of a wave can become very tedious to manipulate when considering more complex wave structures, such as pulses. For this reason, Euler notation is often used to express the harmonic wave functions as complex exponential functions. Over small regions in space, the plane wave approximation can be used to describe *any* non-spherical wave, given that the wavelength is much smaller than the radius of curvature.

A generalized plane wave propagating in the positive z-direction with arbitrary polarization vector $\hat{\mathbf{n}}$ is defined as follows [8].

$$\tilde{\mathbf{F}}(t) = \tilde{\mathbf{A}} e^{(\kappa z - \omega t)} \hat{\mathbf{n}} \quad \text{where} \quad \tilde{\mathbf{A}} = \tilde{A}_x^o e^{i\delta} \hat{\mathbf{x}} + \tilde{A}_y^o e^{i\delta} \hat{\mathbf{y}} \tag{1.2}$$

In this general equation, the phase term (δ) has been absorbed into the complex amplitude. To examine the physical properties of the wave only the real component of the wave function $\mathbf{F}(t) = \Re[\tilde{\mathbf{F}}(t)]$ is considered. The complex amplitude term contains the imaginary quantities and cannot be measured physically. The polarization state of a pulse is indirectly determined by its effect on the observed intensity when passed through a polarizing medium. It is common to express, and often easier to visualize, a wave function in the temporal domain $f(t)$, as it propagates in time, but the wave function can be equivalently expressed in the frequency domain $f(\omega)$, and vice versa, by

using the mathematical Fourier Transform relation:

$$\tilde{\mathbf{F}}(t) = \frac{1}{\sqrt{2\pi}} \int_{-\infty}^{\infty} e^{i\omega t} \tilde{\mathbf{F}}(\omega) d\omega \tag{1.3}$$

and the inverse Fourier transform

$$\tilde{\mathbf{F}}(\omega) = \frac{1}{\sqrt{2\pi}} \int_{-\infty}^{\infty} e^{-i\omega t} \tilde{\mathbf{F}}(t) dt \tag{1.4}$$

An exact wave function describing both time and frequency variables $f(t, \omega)$ is not possible. Heisenberg's uncertainty principle states that there must be a discrepancy in attainable information between temporal and frequency domains [9].

Gaussian Shaped Pulses

The plane wave equation (1.2) is an idealized mathematical solution that describes only infinitesimal regions of a wavefront and does not describe the properties of femtosecond pulses produced in a laboratory environment. The most appropriate representation of the electric field for a pulsed laser is the Gaussian distribution shape in the following general complex form [10]:

$$\tilde{\mathbf{E}}(t) = \mathbf{E}_o e^{-i\omega t - 1.177(1+ia)\left(\frac{t}{\tau_p}\right)^2} \tag{1.5}$$

where τ_p represents the temporal bandwidth of the pulse and a is a frequency chirp parameter ($a < 0$ negative chirp and $a > 0$ positive chirp). Pulses that do not have chirp $(a \neq 0)$ are called transform-limited (TL) pulses and represent the lowest limit in the duration-bandwidth product. A pulse becomes *chirped* when the oscillating frequency envelope varies non-linearly as a function of time [10, 11]. Group velocity dispersion caused by the propagation of polychromatic light in condensed transparent media is the main source of

chirp. The temporal and spectral characteristics of an electric field are related to each other directly through the Fourier transform and may not vary independently (figure 1.3). To express the time-dependent electric field of equation(1.5) in the frequency domain, we simply substitute the electric field into equation(1.4) and solve the integral:

$$\Delta\nu_p \Delta\tau_p = 0.44\sqrt{1+a^2} \tag{1.6}$$

For TL optical pulses in the femtosecond ($\Delta\tau_p \sim 100 \times 10^{-15}$s) domain we obtain an appreciably large frequency bandwidth ($\Delta\nu_p \sim 4.4 \times 10^{12}$Hz $\rightarrow$ $\Delta\lambda \sim 8.8 \times 10^{-9}$m) which makes femtosecond pulses particularly susceptible to chromatic aberrations [12]. The intensity of the pulse is equal to the absolute square of the electric field ($I \propto |\mathbf{E}\bar{\mathbf{E}}|$) and is a real-valued function.

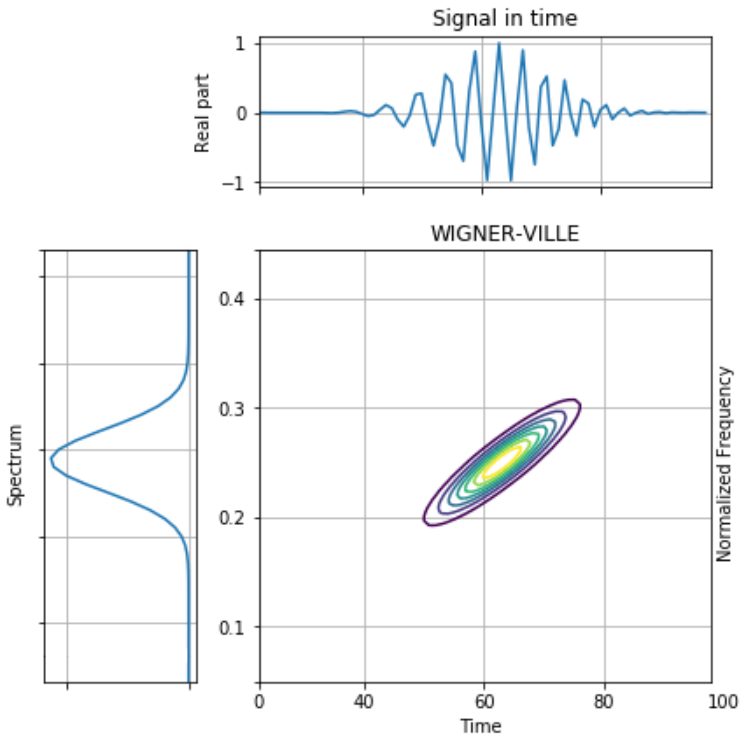

FIGURE 1.3: A Wigner-Ville contour plot (centre) of a linearly chirped Gaussian pulse centered at (60,0.25), the colour scaling of the contour lines run from yellow (high) to purple (low). The pulse shape cross-sections are plotted in the temporal (top) and frequency (left) domains with arbitrary units.

1.1.2 The Transition Dipole Moment

Electromagnetic radiation consists of perpendicularly oscillating electric $\mathbf{E}(t)$ and magnetic $\mathbf{B}(t)$ fields. The electric field interacts with charged particles such as the nucleus and orbiting electrons. Consider a molecule as a collection of charged particles with resultant electric dipole $\boldsymbol{\mu} = \sum_i q_i \mathbf{r_i}$ impinged by a linearly polarized electric field $\mathbf{E}(t) = \mathbf{E_0}\cos(\omega t)$, where q_i and $\mathbf{r_i}$ represent the i^{th} particle's charge and separation vector, respectively. This light-matter interaction is expressed as a time-dependent perturbation $\hat{H}_1(t) = -\boldsymbol{\mu} \cdot \mathbf{E}(t)$ of the system Hamiltonian which can be solved by the time-dependent Schrödinger equation [13]:

$$i\hbar \frac{\partial \Psi(t)}{\partial t} = \hat{H}\Psi(t) = (\hat{H}_o + \hat{H}_1(t))\Psi(t) \tag{1.7}$$

where $\Psi(t)$ represents a complete set of eigenfunctions Φ_k with time-dependent coefficients $C_k(t)$:

$$\Psi(t) = \sum_k C_k(t)\Phi_k e^{\frac{-iE_k t}{\hbar}} \tag{1.8}$$

where E_k represents the energy of the k^{th} eigenfunction. Assume that at t=0 the system is in the initial state Φ_1^0 so that $C_1(0) = 1$ and zero elsewhere. Inserting equation (1.8) into (1.7) then yields a set of equations for the time-dependent coefficients:

$$C_k(t) = -\frac{i}{\hbar}\int_0^t e^{i\omega_{k1}t'/\hbar} \left\langle k|\hat{H}_1(t')|1\right\rangle dt' \tag{1.9}$$

The probability of finding the system in an excited state k, after absorbing a photon with energy $\omega_{k1} = (E_k - E_1)/\hbar$, is given by $|C_k(t)|^2 = P_k(t)$. By substituting the perturbation Hamiltonian term into equation (1.9), integrating

and calculating the probability, we obtain the following complete equation:

$$P_k(t) = \frac{1}{\hbar^2} |\langle k|\boldsymbol{\mu}|1\rangle|^2 \frac{|\mathbf{E_o}|^2 \cos^2\theta \sin^2 \frac{1}{2}(\omega_{kl} - \omega)t}{(\omega_{kl} - \omega)^2} \tag{1.10}$$

where θ defines the angle between the dipole and electric field vectors, respectively. In equation (1.10) the quantity $|\langle k|\boldsymbol{\mu}|1\rangle|^2 = |\boldsymbol{\mu}_{k1}|^2$ is defined as the dipole strength and is directly related to the probability $P_k(t)$ of finding the system in electronic state k at time t after absorbing a quantum of light. If the final and initial state wavefunctions do not overlap (i.e $|\boldsymbol{\mu}_{fi}|^2 = 0$) then the transition $i \rightarrow f$ will not occur. Transitions with the highest probability are those with strongly overlapping wavefunctions, excited near the resonance frequency ($\omega = \omega_{kl}$) and with dipole interaction occurring at the magic angle ($\theta = 54.7°$). The orientation of the excitation electric field is fixed but the molecules suspended in solution have many possible orientations. Thus, the angle between $\boldsymbol{\mu} \cdot \mathbf{E}$ has many possibilities and can be accounted for by replacing $\cos^2\theta$ in equation (1.10) by a factor of $1/3$ (averaged in 3D). Typically in spectroscopic measurements the excitation frequency of the pulse is polychromatic, therein, integrating equation (1.10) over a band of frequencies and taking the time derivative then defines the rate of change in the population of the level k as a function of frequency [14]:

$$\frac{\mathrm{d}P_k(t)}{\mathrm{d}t} = \frac{\pi}{3\epsilon_0\hbar^2}|\boldsymbol{\mu}_{k1}|^2 W(\omega) = B_{1k}W(\omega) \tag{1.11}$$

where W(ω) is time-averaged energy density distribution. The quantity B_{1k} is often referred to as the Einstein coefficient for absorption from states $1 \rightarrow k$.

1.2 Spectroscopy Fundamentals

1.2.1 The Franck-Condon Principle

In a molecule, the positions of the nuclei are not static but rather vibrate relative to their nearest neighbours. Excitation of electrons between electronic states typically leads to a change in the vibrational state of the molecule due to the rearrangement of charges. The equilibrium bond length of excited electronic states is typically larger than the displacement of the ground state, this due to the formation of anti-bonding pi orbitals. The Born-Oppenheimer (BO) approximation allows for the separation of electronic $|e\rangle$ and nuclear $|\nu\rangle$ wave functions, due to the nucleus of an atom being substantially heavier than the orbiting electrons, thus allowing an analytical solution to Schrödinger's equation (only for very small systems). In addition to the BO approximation, the Franck-Condon principle then states: due to the large difference in mass ($m_{nucleus} \gg m_{electron}$), electronic transitions occur on such short time scales (table 1.1) that the heavy nucleus remains unperturbed during the initial redistribution of electrons [15]. Vibrational transitions can be quantified using a transition dipole moment, determined by the expected value of the dipole operator $\boldsymbol{\mu}_{if}$:

$$\boldsymbol{\mu}_{if} = \langle e_f \nu_f | - e \sum_i \mathbf{r}_i + e \sum_k Z_k \mathbf{R}_k | e_i \nu_f \rangle \tag{1.12}$$

Due to orthogonality of electronic wavefunctions $\langle e_f | e_i \rangle = \delta_{if}$ the nuclear dipole interaction term becomes zero and equation (1.12) simplifies to:

$$\boldsymbol{\mu}_{if} = -e \sum_i \langle e_f | \mathbf{r}_i | e_i \rangle \langle \nu_f | \nu_i \rangle \tag{1.13}$$

$$= \boldsymbol{\mu}_{e_f, e_i} S(\nu_f, \nu_i) \tag{1.14}$$

where μ_{e_f,e_i} represents an orthogonal transition dipole matrix, describing the redistribution of electrons in the molecule and $S(\nu_f, \nu_i)$ is the overlap integral between the initial and final vibrational states. Taking the square of

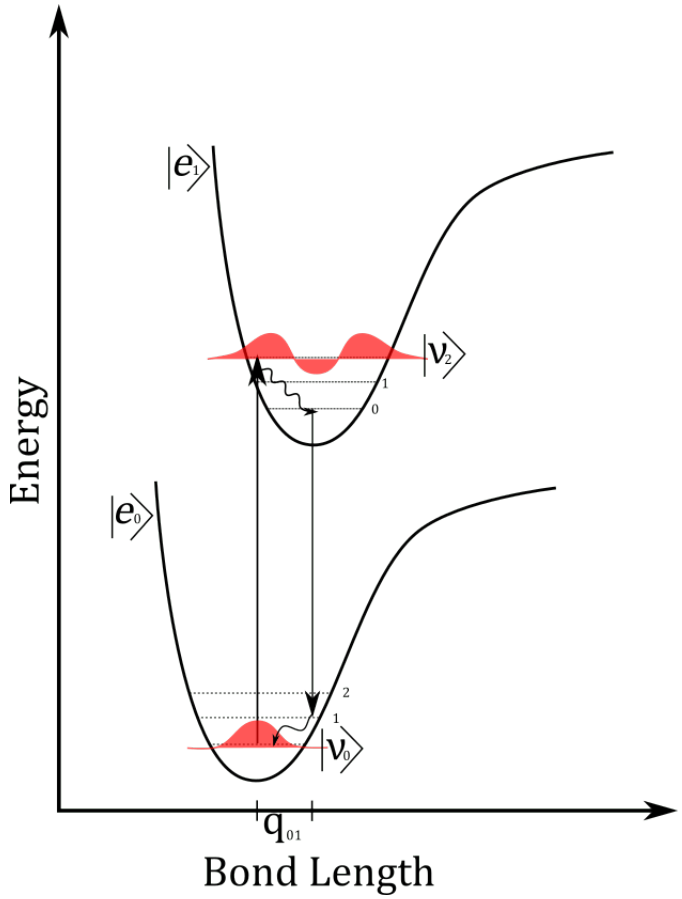

FIGURE 1.4: A potential energy diagram depicting the vertical transition of an electron from the lowest vibrational level in the ground electronic state $S_{0,0}$ to the higher vibrational level in the excited electronic state $S_{1,2}$. The two vibrational wavefunctions $|\nu_0\rangle$ & $|\nu_2\rangle$ have the greatest Franck-Condon factor and is the most likely transition.

the overlap integral $|S(\nu_f, \nu_i)|^2$ determines the intensity or probability for a transition to occur between vibrational levels $i \rightarrow f$ and is referred to as the Franck-Condon factor (figure 1.4). The non-radiative energy dissipation prior to fluorescence causes a redshift in the emission spectrum and is called the Stokes-shift. Stokes-shift is common in nearly all molecular systems because a $S(0,0)$ transition is generally the least probable under normal circumstances [16].

1.2.2 The Beer-Lambert Law

Absorption Spectroscopy is the technique whereby electromagnetic radiation is used to stimulate and probe information about the electronic structure and chemical properties of a molecular system [17]. When electromagnetic radiation (photons) enters a sample it will interact with a molecule and can be absorbed, transmitted or scattered [18]. The Beer-Lambert law determines the ratio of incident to transmitted light intensity through a dilute sample and relates it to an absorption index (in units of optical density OD) logarithmically. Analytical and physical chemists often use absorption spectroscopy to characterize various chromophores (molecules that absorb visible light). Molar quantities (1 mol $= 6 \times 10^{23}$ particles) of a sample material are usually prepared and dissolved in appropriate solvents to increase the concentration with the aim of increasing the number of photo-absorption events occurring.

Formalization of the Beer-Lambert Law

Consider a liquid sample cuvette (made of fused quartz) with area A, thickness x and molecular concentration C. The number of excitable particles in the beam path is $\sigma ACdx$, where σ is the absorption cross-section and defines the probability that a photon will be absorbed by the molecule as it propagates inside the sample holder. The transmitted intensity, in the direction of propagation, is expected to decreases as the light propagates further into the sample [19]. The rate of change in the intensity as a function of distance traversed is as follows:

$$\frac{dI_x}{dx} = -I_x^0 \sigma C$$

Integrating on both sides yields:

$$I_x = I_x^0 e^{-\sigma C x} \tag{1.15}$$

where I_x and I_x^0 represent the final and initial intensities, respectively. The term 'absorption spectroscopy' is slightly misleading because it is actually the transmittance T that is measured by the detector and converted into an absorbance value through the inverse log law:

$$A = -\log T = -\log \frac{I_x}{I_x^0}$$

$$\therefore \quad A = \varepsilon C d$$

In cases where the scattering of incident light is neglected, the sample absorbance index is proportionately equal to the absorption cross-section in which case one describes a linear extinction coefficient (i.e. $\sigma \propto \varepsilon$). Thus the amount of light absorbed in a sample will increase exponentially as a function of depth until it emerges with a reduced transmission intensity. The sample holder is typically a quartz cuvette due to its high transmission coefficient in the visible and near-IR region.

1.2.3 Einstein Coefficients

Spontaneous Emission

Consider an ensemble of atoms at stable room temperature. The Boltzmann-entropy law stipulates that most of the atoms will have all their electrons residing in the lowest electronic energy level (ground state). If an electron was instantaneously raised to occupy a higher excited state, it would spontaneously decay over time and return to the equilibrium ground state without any external influence (figure 1.5). To obey conservation of energy, an electron transition from an upper (u) to lower (l) electronic levels must be coupled with the instantaneous emission of a photon with energy equal to the change in energy levels $E_u - E_l = \Delta E_{ul}$ [20]. The rate of change in excited

state population N_u that decays to lower lying states $i, j, k..$ is described as follows [21]:

$$\frac{(dN_u)}{dt} = -(\kappa_{ui} + \kappa_{uj} + \kappa_{uk} + ...)N_u = -\left(\sum_i \kappa_{ui}\right) N_u$$

$$\therefore\ N_u(t) = N_u^o \exp\left[-\sum_i \kappa_{ui}\right] t = N_u^o \exp\left[-\frac{1}{\tau_u}\right] t$$

where $\sum_i \kappa_{ui}$ represents the summation of all the transitions from upper to lower levels. The decay lifetime of a specific transition is defined as the inverse of its transition rate:

$$\tau_{ui} = \kappa_{ui}^{-1}$$

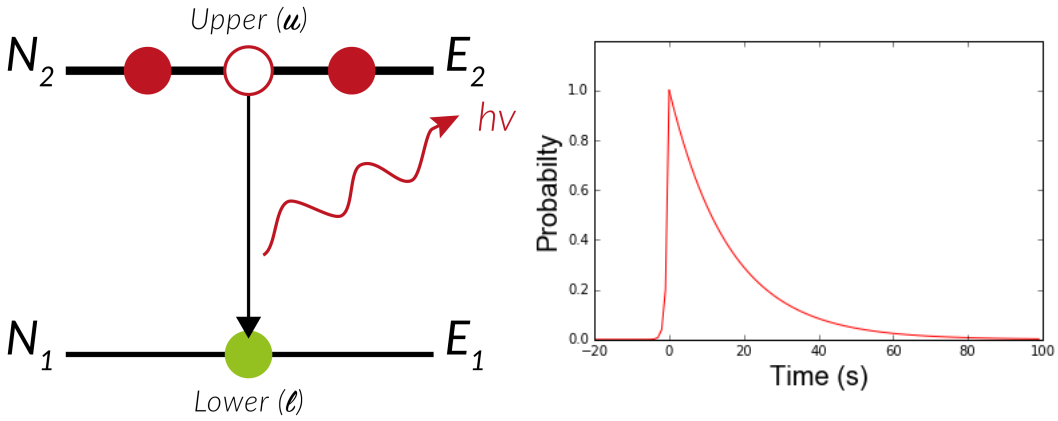

FIGURE 1.5: (left) Spontaneous emission of a photon ($h\nu = \Delta E$) coupled to electron transitions from higher (E_2) to lower (E_1) energy states. (right) Probability distribution of electrons occupying a single excited state (N_2) spontaneously decaying to a lower state (N_1) as a function of time, resulting in a mono-exponentially decreasing distribution of upper excited state population (t = 49 represents the instantaneous excitation event).

Absorption and Stimulated Emission

Apart from the "natural" decay of excited electrons, there are two other electron transition processes which can occur, namely, excitation and de-excitation of electrons, otherwise known as absorption and stimulated emission, respectively. Both processes are induced externally and require the interaction of a photon with appropriate energy [20].

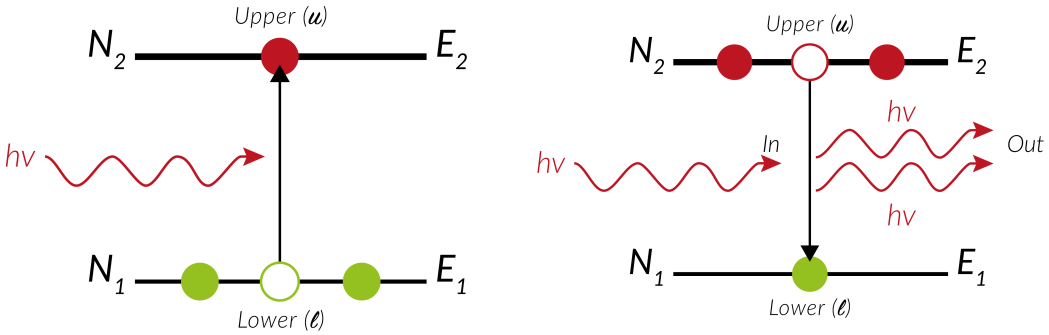

FIGURE 1.6: Absorption (left) and stimulated emission (right) of a photon with energy $h\nu = E_2 - E_1 = \Delta E$.

Albert Einstein contemplated that in an equilibrium environment the number of particles entering a quantum state must be equal to the number of particles exiting and it was this simple energy balancing equation which theorized the existence of a stimulated emission process [22]. Stimulated emission is the inverse process of absorption wherein, instead of promoting an electron from a lower to a higher energy state, an electron can be stimulated from a higher to a lower energy state, thereby emitting a photon with appropriate energy. The transitioning electron emits an identical copy of the photon by which it was stimulated, resulting in the coherent propagation of two identical photons (figure 1.6). It is this exact phenomenon which inspired Charles Hard Townes et al. to theorize and develop the first working laser system in the early 1960s. The rate at which electrons populate energy states during stimulated emission and absorption transition processes can be

generalized as:

$$\frac{dN_f}{dt} = B_{if} W(\omega) N_i$$

where N_f and N_i represent the final and initial state electron populations, respectively, and $W(\omega)$ denotes the energy density of the radiation field as a function of the transition frequency. The coefficient B_{if} represents absorption if $f > i$ and stimulated emission if $f < i$.

In Summary

Consider a 2-level system (N_1 and N_2) as in figure (1.5). In total there are three radiative transition processes that can occur, namely; Absorption B_{12}, stimulated emission B_{21} and spontaneous emission A_{12}. The total rate of electrons populating N_1 from excited state N_2 is a combination of all three processes:

$$\frac{dN_1}{dt} = -B_{12} W(\omega) N_2 + B_{21} W(\omega) N_2 + A_{21} N_2 \tag{1.16}$$

assuming the system is in a steady-state (i.e.$\frac{dN_1}{dt} = 0$) and substituting the Boltzmann-Entropy relation, equation (1.16) can be rewritten as:

$$W(\omega) = \frac{A_{21}}{B_{12}(N_1/N_2) - B_{21}} = \frac{A_{21}}{B_{12}(e^{-\Delta E_{12}/\kappa T}) - B_{21}} \tag{1.17}$$

The result of equation (1.17) must be equal to the Planck radiation law which gives rise to the following steady-state conditions:

$$B_{12} = B_{21} \quad \& \quad \frac{A_{21}}{B_{21}} = \frac{\hbar\omega}{\pi^2 c^3}$$

substitution of these conditions into equation (1.11) allows us to relate any of the three transition processes directly to the dipole strength $|\boldsymbol{\mu}_{12}|^2$:

$$\therefore \quad A_{21} = \frac{\omega^3}{3\pi c^3 \epsilon_0 \hbar} |\boldsymbol{\mu}_{12}|^2 \tag{1.18}$$

1.2.4 The Jablonski Diagram

The so-called Jablonski diagram, named after Polish physicist Aleksander Jablonski, is a schematic that is used to quantitatively represent the various energy de-excitation processes (either radiative or non-radiative) that can occur when a molecule is excited by a photon primarily from the UV→NIR wavelength region. The vertical axis represents energy and bold, horizon-

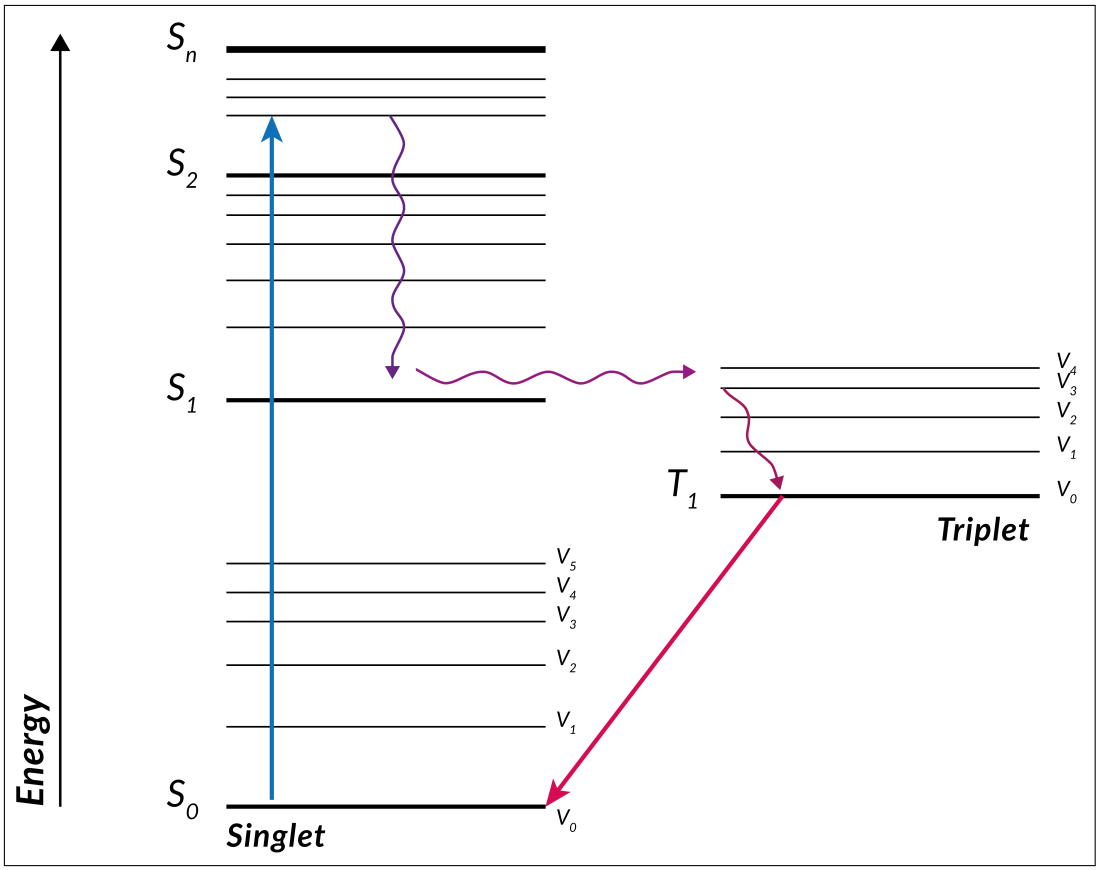

FIGURE 1.7: A Jablonski diagram indicating the radiative (straight arrows) and non-radiative (curved arrows) energy dissipation processes. Absorption ($S_{0,0} \rightarrow S_{2,1}$), Internal-conversion ($S_{2,1} \rightarrow S_{1,0}$), inter-system crossing ($S_{1,0} \rightarrow T_{1,3}$), vibrational relaxation ($T_{1,3} \rightarrow T_{1,0}$) and phosphorescence ($T_{1,0} \rightarrow S_{0,0}$)

tally drawn lines indicate the limits of the electronic states on top of which the respective vibrational states are drawn (figure 1.7). The electronic and vibrational states are grouped into vertical columns according to their spin multiplicity (either singlet or triplet) [23]. Directly after absorption takes

place (typically from the ground state), straight (radiative) and wavy (non-radiative) lines connect various transitions between allowed electronic and vibrational eigenstates. Absorption, fluorescence, and phosphorescence are some of the main radiative processes (radiative because they are energetically coupled to a photon either by absorbing or emitting radiant energy). Internal-conversion, vibrational relaxation, and inter-system crossing are known as the non-radiative processes (i.e. do not involve absorption or emission of photons).

Radiative and Non-Radiative Processes

The Boltzmann entropy law determines the electron population of various energy levels as a function of available energy or temperature of the system. Typically (at room temperature) most molecules will reside in the singlet ground electronic state from which they can be excited into higher electronic and vibrational levels [18]. After excitation (absorption), the molecule quickly relaxes to the lowest vibrational state of the excited electronic state (vibrational relaxation) where it remains for a short period of time before it can emit a photon (fluorescence) and return to the singlet ground state. In some cases, there is a strong overlap of vibrational levels and coupling between distinct electronic states. This can lead to vibrational relaxation occurring between electronic states of the same spin multiplicity $2S + 1$ and is termed internal conversion [24]. Electrons are half-spin particles ($s = \pm\frac{1}{2}$) and occupy electronic states as electron-pairs with opposite spins, as stated by the Pauli exclusion principle [8]. The electronic state wave functions can either be anti-symmetric singlet states with total spin $S = \pm\frac{1}{2} \mp \frac{1}{2} = 0$ or symmetric triplet states with total spin $S = \pm\frac{1}{2} \pm \frac{1}{2} = \pm 1$. Typically, an electron can not change its spin but due to an effect known as spin-orbit coupling an excited-singlet state electron may undergo a spin flip and occupy

Transition	**Rate Symbol**	**Typical Time Scale (s)**
Absorption	κ_{abs}	10^{-15}
Internal Conversion	κ_{ic}	$10^{-14} - 10^{-11}$
Vibrational Relaxation	κ_{vib}	$10^{-14} - 10^{-11}$
Fluorescence	κ_{fl}	$10^{-9} - 10^{-7}$
Inter-system crossing	κ_{isc}	$10^{-8} - 10^{-3}$
Phosphorescence	κ_{ph}	$10^{-4} - 10^{-1}$

TABLE 1.1: Various radiative and non-radiative processes with approximate time-scales [25].

the triplet excited state (inter-system crossing). An excited triplet state can decay back to the singlet ground state (via phosphorescence) or to the triplet ground state. All radiative and non-radiative processes can occur simultaneously within the system and hence are constantly competing with each other [26].

1.2.5 Electron Transfer

The process of photo-induced electron-transfer (ET) within supramolecular assemblies can be described using Marcus theory [27]. In Marcus theory, molecules are drawn as positive parabolas which conform to a simple harmonic oscillator model as a function of the reaction coordinate. The vertical (free energy) and horizontal (reaction coordinate) displacement of each parabola (molecule) impact the electron-transfer kinetic rates between the D-A system. There are two main factors which determine the rate of ET. The first is the Franck-Condon principle which states that electron transfer occurs instantaneously and does not influence the nucleus (i.e. the reaction coordinate). The second is the First Law of Thermodynamics which states that energy must be conserved and implies that ET must be an isoenergetic process, meaning that the system cannot produce more energy than it absorbs. Both of these conditions are satisfied at the point where the parabolas intersect

each other. Within this framework, the kinetic rate (κ_{ET}) of electron-transfer between a donor-acceptor system can be expressed as [28]:

$$\kappa_{ET} = \nu e^{\frac{-\Delta G^{\neq}}{RT}}$$

where R, T and ν are the gas constant, absolute temperature (on the Kelvin scale) and frequency factor, respectively. The frequency factor is defined as a product of the vibrational frequency ν_n for the specific electron transition and the transmission coefficient κ_{el}, which has a value between 0 and 1 that describes the degree of coupling between the electronic orbitals of the donor and acceptor.

The variable $\Delta G^{\neq}$ is defined as the Marcus free energy of activation:

$$\Delta G^{\neq} = \frac{-(\Delta G^0 + \lambda)^2}{4\lambda} \tag{1.19}$$

where ΔG^0 is the free-energy change for the reaction and λ is the reorganization energy, i.e. energy required to "reorganize" the system structure from initial to final coordinates, without making the charge transfer. The reorganization energy is comprised of two contributions ($\lambda = \lambda_{outer} + \lambda_{inner}$). The outer-sphere component describes the external interactions with the surrounding solvent, and the inner-sphere component describes changes to the molecular geometry of the system during the formation of the product state. Both terms (λ_{outer} and λ_{inner}) can be calculated analytically and require detailed information about the complex.

Looking closely at the relationship between ΔG^0 and λ in the parenthesis of equation (1.19), there are three distinct cases which may occur (figure 1.8). The first case is such that $\Delta G^0 < \lambda$, which defines the "normal region" where the rate of ET, κ_{ET}, increases proportionally with an increase in ΔG^0. The

second special case is defined when $\Delta G^0 = \lambda$, which is known as the "activationless" ET region and defines the point where the electron transfer rate between D-A is a maximum such that no additional energy is required for electrons to be transferred. The third case is when $\Delta G^0 > \lambda$, which is defined as the " Marcus inverted region" where, contrary to the first case, an increase in the free energy ΔG^0 causes a decrease in the rate of electron transfer κ_{ET}.

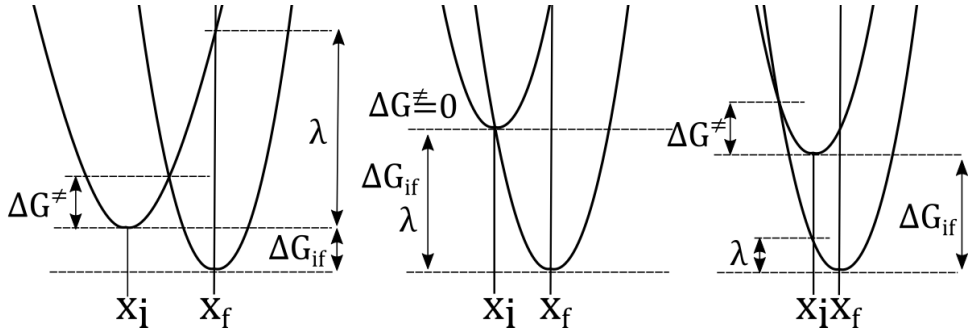

FIGURE 1.8: Parabolas indicating (left) "normal", (right) "inverted" and (middle) "activationless" Marcus electron transfer regions, where $\Delta G_{if} = \Delta G^0$. Reprinted with permission from [29]. Copyright 2007 Royal Chemistry Society. Where x_i and x_f represent the initial and final reaction coordinates, respectively.

1.3 Artificial Photosynthesis

The development of electronic components at a molecular scale is an active area of research and holds great promise for the renewable energy industry. The efficiency of light harvesting in natural photosynthesis depends on two important processes; firstly, photons of various wavelengths (between 350 nm and 700 nm) are absorbed by antenna chromophores (mainly chlorophyll and carotenoid pigments) that funnel the absorbed energy through singlet-singlet energy transfer toward a reaction centre [30]. Secondly, energy arriving at the reaction centre is converted to chemical potential in the form of long-lived charge-separated states which drives other important processes such as the production of glucose [27, 31]. Amazingly, this process

occurs with a quantum efficiency close to 100%, meaning, for every photon absorbed, a charge-separated state is produced. Artificial photosynthesis aims to synthesise simple organic compounds that mimic the natural photosynthetic processes and efficiencies to produce bio-inspired solar cells or are used to drive chemical reactions that produce fuel directly. For an artificial system to be efficient at light harvesting and energy storage, it should mimic the following natural photophysical and electrochemical characteristics of photosynthesis [32]:

(i) Incident visible light must be efficiently captured by the "antenna" chromophores and lead to the formation of a stable excited state with a decay lifetime long enough for electron transfer (ET) to take place.

(ii) The absorption of a photon by the antenna chromophore must result in the transfer of an electron to the bound acceptor molecule to produce a charge-separated state (figure 1.9).

(iii) Electron transfer between donor (D) and acceptor (A) moieties is directional and determined by the overlapping geometry of the respective orbital wave functions which generally depends on the location of the highest occupied molecular orbital (HOMO) and lowest unoccupied molecular orbitals (LUMO).

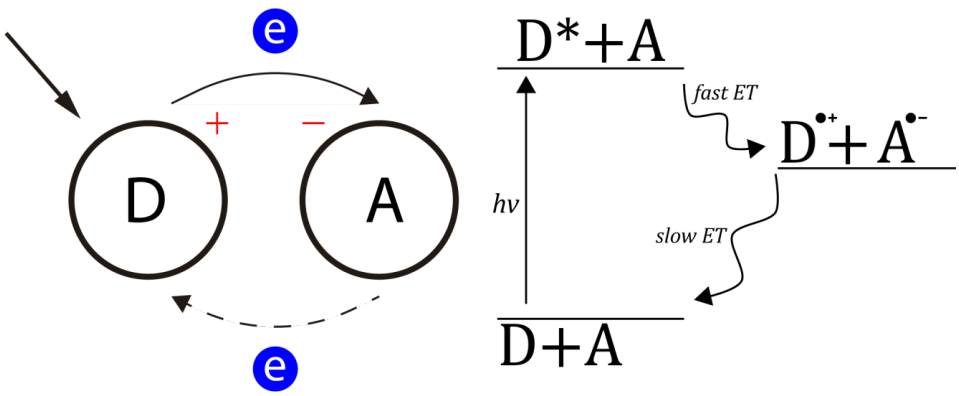

FIGURE 1.9: A depiction of the simplest artificial light harvesting system (left), along with its Jablonski diagram (right) showing the absorption (solid line) charge separation and recombination process (wavy lines)

Donor-Acceptor Systems

The most basic artificial light harvesting system consists of a donor molecule, which absorbs light in the visible wavelength (chromophore), bonded to an acceptor molecule. The choice of donor and acceptor molecules depends on their electrochemical and photophysical properties and, importantly, the method of their attachment. Donor molecules can be covalently attached to acceptors via linker molecules, or spacers which are usually conjugated groups, to form dyads with varying D-A separation distances, size and complexity [30]. Covalently linked systems generally undergo electron transfer (ET) from the triplet excited state to the acceptor resulting in slow charge-separation (CS) rates (table 1.1). Supramolecular complexes (commonly referred to as non-covalently linked systems), on the other hand, do not undergo ET from the excited triplet, but rather an electron is transferred directly from the singlet excited state resulting in fast CS. Also, the non-covalent bonds of supramolecular complexes can be reversible, meaning that after ET the $D^{\bullet+} - A^{\bullet-}$ CS states can further diffuse, prolonging the charge-recombination (CR) process [32].

1.3.1 Supramolecular Fullerene-Porphyrin Complexes

Porphyrin

Porphyrin are polypyrroles and are a large conjugated planar molecule that absorbs light strongly in the visible region of the electromagnetic spectrum. The basic structure of porphyrin consists of four pyrrole rings connected by methine bridges with a total of 18-π electrons, thus making it aromatic. The four inner nitrogen atoms bond to form two pyrrole and two pyridine structures which distort the molecular symmetry such that the top and bottom

benzene rings become slightly skewed (figure 1.10). The vacant site in the

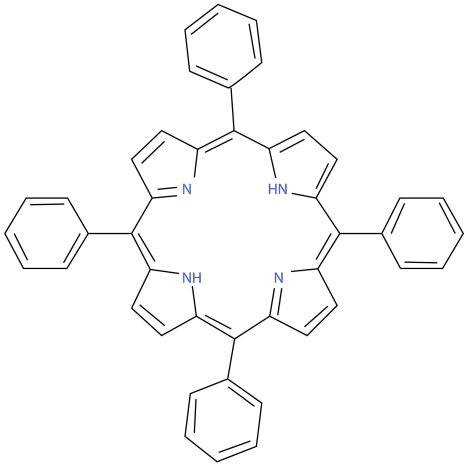

FIGURE 1.10: Molecular diagram of free-base porphyrin [33].

centre of the structure can be occupied by transition metals such as iron, zinc, manganese and many others. Metals are electrostatically held in the centre by the nitrogen atoms to form a metalloporphyrin structure. Each substituted metal species alters the photophysical and electrochemical nature of the molecule making it a versatile electron donor for use in a variety of photoinduced applications [34]. Porphyrins have characteristic spectroscopic features such as a strong absorption peak around 420 nm (Soret band) and smaller intensity $Q(x, y)$-bands occurring at $\sim 550 - 600$ nm which are due to $\pi \rightarrow \pi^*$ transitions of the aromatic porphyrin ligand in the x-y axial directions [35].

Fullerene

Fullerenes are polyhedral molecules consisting of carbon atoms bonded into a symmetrical, hollow spherical structure and exhibit a number of unique properties that make them excellent candidates as electron acceptors. Fullerenes C_n are mathematically possible for $n = 20$ and all even values $n \geq 24$ [36]. Buckminsterfullerene or C_{60} represents the most stable and most common

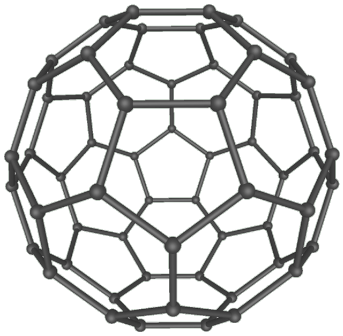

FIGURE 1.11: Molecular diagram for Buckminsterfullerene C_{60} (Michael Ströck, 2006).

fullerene molecule and consists of twenty hexagonal and twelve pentagonal rings such that no two pentagons share an edge (figure 1.11). Some unique characteristics include the ability to reversibly accept up to 6 electrons (due to the LUMO level being 3-fold degenerate), low electron re-organizational energies and the ability to assist in the rapid production of charge separated (CS) states. The symmetry of the C_{60} carbon cage allows accumulated electrons to diffuse across its surface and efficiently form bottleneck states which prolong the charge recombination (CR) process [37], a key characteristic for replicating the natural photosynthesis process [32]. Fullerene C_{60} has also proved to be useful as an organic semiconductor where its ability to readily accumulate charge makes it an excellent n-type semiconductor material [38].

Fullerene-Porphyrin Complex

An explanation of the fullerene-porphyrin non-covalent interaction is not easily described using conventional bonding arguments. The curved π-surface of the fullerene and the planar π-surface of the porphyrin interact strongly, producing centre-to-centre separation distance much shorter than the typical van der Waals range, suggesting strong $\pi \rightarrow \pi$ interactions to be involved (table 1.2). Theoretical modelling using density functional theory (DFT) revealed that a significant contribution (50-60%) of the attractive interaction is due to electrostatic interactions [39]. DFT simulations show that the 6:6

	$C_{60} - TPP$	$C_{60} - ZnTPP$
D_{cc}	2.743	2.770
ΔE_{int}	−17.33	−16.25
ΔV_{elstat}	−20.75	−29.51

TABLE 1.2: Centre-to-centre distances (Å) and interaction energies (*kcal/mol*) for supramolecular C_{60}-TPP and C_{60}-ZnTPP complexes [39].

(intersection of two hexagonal rings) bonds of the fullerene moiety are an electron-rich area, resulting in a highly negative potential energy in that region. Tetraphenylporphyrin (TPP) was found to have a localized negative electrostatic potential in the inner ring of the structure due to the nitrogen atoms while the tetraphenylporphyrinato-zinc (ZnTPP) displayed a greater negative electrostatic potential due to the presence of a metal (zinc) (figure 1.12). When both moieties are mixed in a non-polar solvent such as toluene,

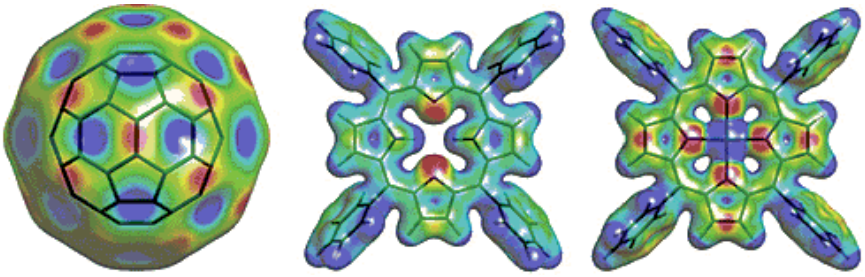

FIGURE 1.12: Molecular electrostatic potential diagram for C_{60} (left), TPP (middle) and ZnTPP (right). The colour scheme runs from red (negative potential) to blue (positive potential). Reprinted with permission from [39]. Copyright 2003 American Chemical Society.

the four nitrogen atoms of the TPP inner ring coincide with the centres of the four carbon rings (two-pentagonal and two hexagonal rings) which surround the 6:6 bond [39] (figure 1.13). Following a photoinduced ET from the porphyrin to the fullerene cage, the backward ET process occurs in the Marcus "inverted region", meaning that the rate constants decrease as the free energy ΔG^0 increases [41].

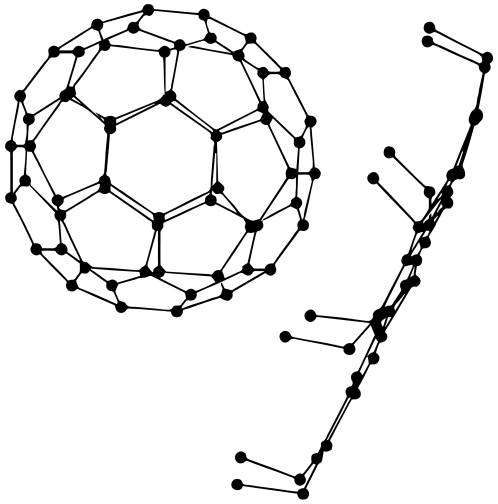

FIGURE 1.13: Molecular diagram of supramolecular fullerene-metalloporphyrin complex (C_{60}·2CoOEP). Reprinted with permission from [40]. Copyright 1999 American Chemical Society.

Aim

The aim is to investigate the dynamics of energy and electron transfer (i.e. charge-separation) processes within the proposed D-A supramolecular systems. To achieve this requires an assortment of spectroscopic measurements such as ground-state absorption, steady-state fluorescence, and femtosecond pump-probe, spectroscopy to spectrally identify and temporally resolve the various radiative and non-radiative processes which occur after photo-excitation. Performing the above mentioned spectroscopic experiments and subsequent data analysis requires a concrete understanding of physical principles which describe the various light-matter interactions with organic molecular systems, as well as an in-depth understanding of experimental methodologies which are necessary to perform advanced laser-based research.

Overview

In chapter 1, the fundamental principles of light-matter interactions relating to spectroscopy were introduced and provided the necessary basis to understand and interpret spectroscopic data. In chapter 2, the femtosecond pump-probe experimental technique is explained in detail. This includes a section on signal detection and temporal resolution which discusses important processes such as white-light generation, second-harmonic generation and pump-probe overlap geometry, as well as other resolution limiting factors which need to be considered. Chapter 3 provides a complete description of the new pump-probe system which was built and used to collect the transient absorption data presented in this dissertation, and also includes useful instructions for optimizing the system so that high-quality measurements can be performed. Chapter 3 also provides a brief description of the graphical user interface which was developed in `MATLAB` in order to control the hardware, a more thorough standard operating procedure manual is also available in Appendix A. In chapter 4, the femtosecond transient absorption results for the individual donor-acceptor molecules and the supramolecular complexes are presented and discussed, this includes the ground-state absorption and steady-state fluorescence spectroscopic data. Complete kinetic models for each system is then provided with kinetic rates obtained by performing a global kinetic analysis using `GloTaRAn`. The final chapter concludes the results of the experiment and also compares the charge-separation and charge-recombination kinetics to similar D-A systems.

Chapter 2

Fundamentals of Femtosecond Laser Spectroscopy

2.1 Introduction

The femtosecond laser system is the heart of any pulsed ultrafast transient absorption spectroscopy experiment and its operational characteristics will determine the type of peripheral instruments and optics one needs to perform successful measurements. Some of the important laser characteristics one needs to consider includes:

- Pulse Width - A shorter pulse width will improve temporal resolution but as the pulse duration decreases the peak intensity increases. High-intensity optical pulses can lead to multi-photon absorption, producing artifacts in the measured difference absorption data [42].
- Pulse Energy - The fundamental (original) femtosecond pulse that exits the laser often requires wavelength tuning before being used, for example as an excitation pulse. One particular method used for changing the wavelength of the fundamental pulse involves a second-order

light-matter interaction known as non-collinear optical parametric amplification (NOPA) where a broadband seed pulse is carefully amplified by a high energy narrow bandwidth pump pulse [43]. The fundamental pulse energy, therefore, needs to be sufficient enough to undergo wavelength alterations ($I_{out} \propto \sqrt{I_{in}}$) and still carry sufficient energy to overcome the general losses in further processes such as pulse compression and pulse shaping before finally exciting the sample (which requires at least a few mW of power).

- Pulse Repetition rate - The detection systems often need to be synchronized to the arrival time of each pulse so that integration over the detector is done efficiently and so that each individual pulse can be registered and binned accordingly. Current detection systems can efficiently integrate over pixel arrays in intervals as short as 1 μs which limits the maximum resolvable pulse frequency to 1 MHz.

2.2 Transient Absorption Spectroscopy

By exploiting their unique temporal characteristics, femtosecond pulsed laser systems offer a practical tool for investigating various ultrafast radiative and non-radiative processes, covering a diverse range, from naturally occurring to synthetic molecular systems. Advances in organic chemistry have led to a wide range of artificial photosynthetic systems that aim to mimic photon-absorption, energy-transfer, and charge-separation processes as they occur in the photosystems of natural light-harvesting complexes. The aim one day is to reproduce artificial systems that operate with the same "100% quantum efficiency".

The aim of a transient absorption measurement is to temporally resolve the formation and evolution of various excited states and reaction intermediates,

some lasting only a few femtoseconds, revealing the rate constants of the various radiative and non-radiative processes. To perform a transient absorption or pump-probe measurement, a high energy transform-limited pump pulse ($\tau_p \sim 150$ fs, $\Delta\lambda \sim 10$ nm) instantaneously excites the bulk ground state electrons into higher electronic and vibrational states from which various time-dependent energy dissipative processes can occur (table 1.1). The role of the pump beam is strictly to excite the molecules and is not recorded. A weaker intensity broadband optical pulse, known as the probe pulse, then passes through the excited region of the sample at a relative delay time (Δt) behind the pump pulse, thus capturing the absorption spectra of the excited sample at a specific time. The probe pulse is then (after interaction with the excited sample through absorption or stimulated emission) dispersed into individual wavelength components, using a dispersive grating, and recorded by an array of ultra-sensitive pixels. Time-zero is an important notion in the FTAS experiment ($\Delta t = 0$) and is defined as the moment when both probe and pump pulses overlap temporally (i.e arrive at the same time) (figure 2.1). The time delay between the pump and probe pulses can range from less than a femtosecond (limited by the pulse duration) up to a microsecond or more (depending on the repetition rate of the system) by using precision stepper motors set to small step angles:

$$\Delta t = \frac{d - d_0}{c} = \frac{\Delta d}{c}$$

The variable d represents the distance travelled by the delay line relative to d_0 which marks the position where both pulses overlap temporally at the sample. Δd, Δt and c represent the change in position, change in time and speed of light in a vacuum. To extract the molecules' absorption signal from the system absorption (molecule + solvent + scattering +...) an absorption measurement of the system in the unexcited state ($A_{pump-off}(\lambda)$) is performed and

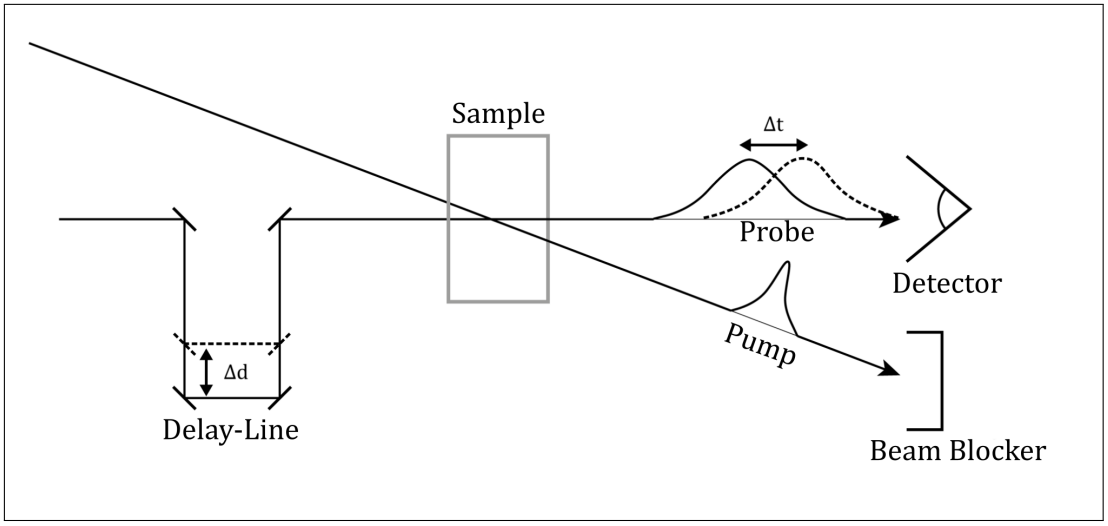

FIGURE 2.1: A simplified sketch depicting the relative change in arrival time between pump and probe pulses at the sample due to the change in position of the delay stage.

subtracted by an absorption measurement of the system in an excited state ($A_{pump-on}(\lambda)$) to reveal only the absorption changes related to the molecule itself and not the environment (solvent + scattering+...). Repeating this procedure for varying delay times between the probe and pump pulses, a 2D transient absorption matrix as a function of time and wavelength is generated (equation 2.1). The pump-on and pump-off measurements are performed shot-to-shot by using an optical chopper set to block every second excitation pulse [44]. The measured transmission intensity and difference absorption are related as follows:

$$\Delta A(\lambda, t) = A_{pump-on}(\lambda, t) - A_{pump-off}(\lambda, t) \tag{2.1}$$

Substituting into the Beer-Lambert law gives:

$$\Delta A = -\log\left(\frac{I_{pump-on}}{I_{pump-off}}\right) \tag{2.2}$$

where $I_{pump-on}$ and $I_{pump-off}$ represent the measured transmission intensity of the excited and unexcited sample states, respectively. The resulting equation (2.2) provides a simple method for relating the transmission intensity to the difference absorption. Information regarding the temporal and spectral evolution of radiative and non-radiative states can then be extracted from the data using global and target analysis software such as `GloTaRan` [45].

2.3 Excited State Dynamics

A time-resolved difference absorption matrix typically contains a dynamic combination of energetic processes such as photon absorption, energy relaxation, electron and energy transfer, charge-separation and product formation occurring across various time-scales [14]. These energetic processes will appear in the difference absorption spectra $\Delta A(\lambda, t)$ as one or more of the following signals (figure 2.2) [46].

1) Ground State Bleach.

At time-zero, when probe and pump pulses overlap temporally, there is an instantaneous moment when a sizeable fraction of ground state electrons are excited into higher energy states. A probe pulse interacting with the excited molecule immediately after excitation ($\Delta t \sim 0$) will encounter fewer electrons in the ground state (reducing the probability of absorption) causing the absorption from the unexcited spectrum to be larger ($A_{pump-off} > A_{pump-on}$). As a result, a negative ΔA signal is observed in the spectral region where absorption from the ground state takes place.

2) Stimulated Emission.

Moments after the molecule has been excited ($\Delta t > 0$), most excited electrons will remain in the excited state for a short period of time (femtoseconds to a few picoseconds) before radiative and/or non-radiative processes begin

to occur. When the probe pulse propagates through the sample during this period, stimulated emission occurs, resulting in the coherent propagation of two identical photons. The increased emission results in a decrease of the $A_{pump-on}$ absorption spectra and hence an overall negative ΔA signal is observed.

3) Excited State Absorption.

The excitation pump pulse is usually very intense, spectrally narrow ($\Delta\lambda \sim$ 10 nm) and tuned to strongly overlap with the ground state absorption transition wavelength. Electrons that have already been *pumped* into excited states can be further excited to higher electronic states by absorbing the lower energy (longer wavelength) photons contained in the broadband probe beam resulting in a positive ΔA signal.

4) Product absorption.

Upon photo-excitation, some molecular systems may form long-lived product states such as triplet states, charge-separated states, and isomerized states. The photo-absorption of these products states into higher states (e.g. $T_1 \rightarrow T_2$) is sometimes observed as positive signals in the difference absorption spectrum (similar to ESA), in addition to, a ground-state bleach signal in the spectral regions where ground-state absorption of the molecule takes place [14].

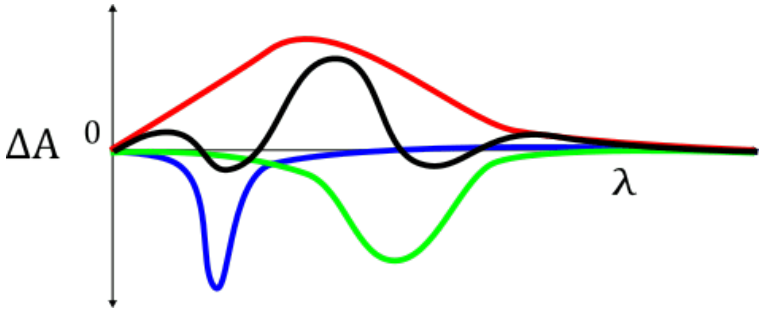

FIGURE 2.2: Three main contributions to a difference absorption signal ΔA: Ground state bleach (blue), Stimulated emission (green), Excited state/product absorption (red) and the total observed signal (black) [14].

2.4 Signal Detection and Optimization

Temporal Resolution

Modern lasers can produce light pulses as short as a few 100s of attoseconds which allow even the fastest photo-physical processes in nature to be resolved in almost real time. There are various physical processes which cause an ultrafast pulse to become stretched in time before it reaches the sample which ultimately reduces the achievable time resolution and general quality of data. Because of this, manufacturers have developed wide ranges of ultrafast optics specially designed to reduce group delay dispersion (chirping) of broadband femtosecond pulses. Silver coated dielectric mirrors offer high reflectivity (>95%) while compensating for phase distortions as the pulse travels through the optical system.

Second-Harmonic Generation

An electric field (**E**) interacting with a certain centrosymmetric non-linear crystal will cause macroscopic polarization of the material, which may give rise to parametric amplification processes or sum/difference frequency generation. A Taylor expansion of the induced polarization (**P**) reveals higher-order polarization terms, each weighted by a susceptibility coefficient χ:

$$\mathbf{P} = \chi^{(1)}\mathbf{E} + \chi^{(2)}\mathbf{EE} + \chi^{(3)}\mathbf{EEE} \tag{2.3}$$

The first-order term represents linear processes in optics (i.e. reflection, absorption, etc.) and the second and higher order terms represent non-linear processes, such as sum-frequency generation (SFG) processes (i.e. SHG, THG, OPA, ect.) as well as other processes such as cross-phase modulation (XPM)

and multi-photon absorption, respectively [8, 47]. Crystals made from barium borate (BBO) and lithium triborate (LBO) are good second order NL materials because they have especially large second order susceptibility coefficients $\chi^{(2)}$. The second-harmonic generation (SHG) process occurs when a single incident photon ($E = \hbar\omega$) is absorbed and two photons emerge with shared energy equal to that of the incident photon (figure 2.3). The inverse process can also occur, such that two energetically similar photons mix non-linearly inside the crystal to produce a single photon with combined energy [48]. These phenomena are utilized in quantum optics to generate entangled photon states. The conversion efficiency of the second harmonic process $I^{out}(2\omega)$ varies with the square of the incident intensity $\sqrt{I^{in}(\omega)}$. There are two types of non-linear crystals, types I and II. Type I crystals are used when the two incident photons have the same polarization state (i.e. both are linearly polarized) and type II crystals are used when they have orthogonal polarization states.

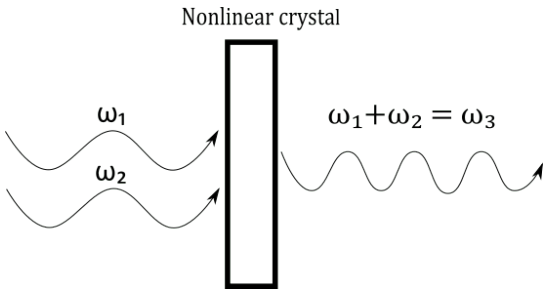

FIGURE 2.3: Sum-frequency generation in a nonlinear crystal with a high second order susceptibility $\chi^{(2)}$. If $\omega_1 = \omega_2$ (i.e. pumped by a monochromatic beam) then the parametric process is referred to as second-harmonic generation.

White Light Generation (WLG)

A femtosecond supercontinuum wave-packet is generated when a non-linear transparent medium is pumped by a high powered monochromatic femtosecond pulsed laser beam. The properties of the transparent media, the

pumping wavelength, and pulse duration will determine the spectral intensity and composition of the supercontinuum. WLG has been reported to occur in a wide range of materials ranging from common bulk laser materials to various gases and even liquids [49]. In the difference absorption equation (2.1), a transmitted intensity spectrum (probe-pulse) is required for both excited ($I_{pump-on}$) and unexcited ($I_{pump-off}$) sample states. In the ideal case, the frequency train of supercontinuum pulses emerging from the WLG process all have identical spectral shapes and intensities when they interact with the sample. Any slight variation in the pulse-to-pulse stability will produce an artificial ΔA signal, thus, the stability of the white-light determines the optical density resolution of the detection system. Common causes for an unstable white-light spectrum are:

- Pumping the WLG material well above the required energy threshold can lead to excessive self-phase modulation (SFM), which results in rapid periodic oscillations of the intensity in the WL spectrum [50]. The oscillations are spectrally broad and start near the pumping wavelength (e.g. 775 nm) and extend far into the IR region. A neutral density filter (NDF) can be used to attenuate the incident beam to the correct energy density for a stable WL spectrum.

- The intensity profile of the beam should be circular and uniform before it is focused into the medium. A non-uniform intensity can lead to the production of multiple filaments which result in an unstable, fluctuating spectral intensity envelope.

- An unstable laser often produces a pulse train that has a variation in the pulse-to-pulse intensity causing the WL to flicker.

- If the probe beam reflects off of a delay-line before the WLG process, any slight misalignment can cause the beam to "walk" as the delay-line moves, resulting in a varying pumping intensity. Ideally, the intensity

of the generated WL spectrum should be the same when the delay-line is in the *home* and *end* positions, respectively. If this is not the case, a near and far-field alignment can be performed by first moving the delay-line to the home position, then aligning in the far-field by monitoring the spectral intensity, then moving the delay-line to the end position and aligning the near-field to match the intensity spectrum obtained in the far-field.

Group Velocity Dispersion (GVD)

Propagation of femtosecond pulses inside transparent media induces dispersion (D), a chromatic aberration caused by the wavelength dependency ($\mathrm{d}\lambda$) of the refractive index of an optical material ($D = \frac{\mathrm{d}n}{\mathrm{d}\lambda}$). A transform-limited pulse propagating in a *normal dispersion medium* will become a *positively chirped* pulse because the higher frequencies (blue) travel slower than the lower (red) frequencies. In *anomalous dispersion media*, the opposite effect is observed and the pulse is said to be *negatively chirped* as the redder frequencies emerge behind of the bluer frequencies [47]. Extensive chirping leads to significantly broadened pulses, which reduce the temporal resolution of the detection system. The amount of temporal broadening can be quantified in terms of the width of the pulse spectrum ($\Delta\lambda$), the dispersion of the medium (D) and the length of propagation in the medium (l):

$$\Delta t_{broad} = \frac{\Delta\lambda\, l}{c} D$$

where c is the speed of light in vacuum.

Femtosecond pulses that undergo wavelength alterations through optical parametric amplification and supercontinuum generation are especially susceptible to pulse chirping because these processes require propagation in

highly condensed transparent media. The severe chirping of the probe pulses can lead to cross-phase modulation (XPM) artifacts, which can obscure the difference absorption data near time zero [51].

Pump-Probe Beam Overlap Geometry

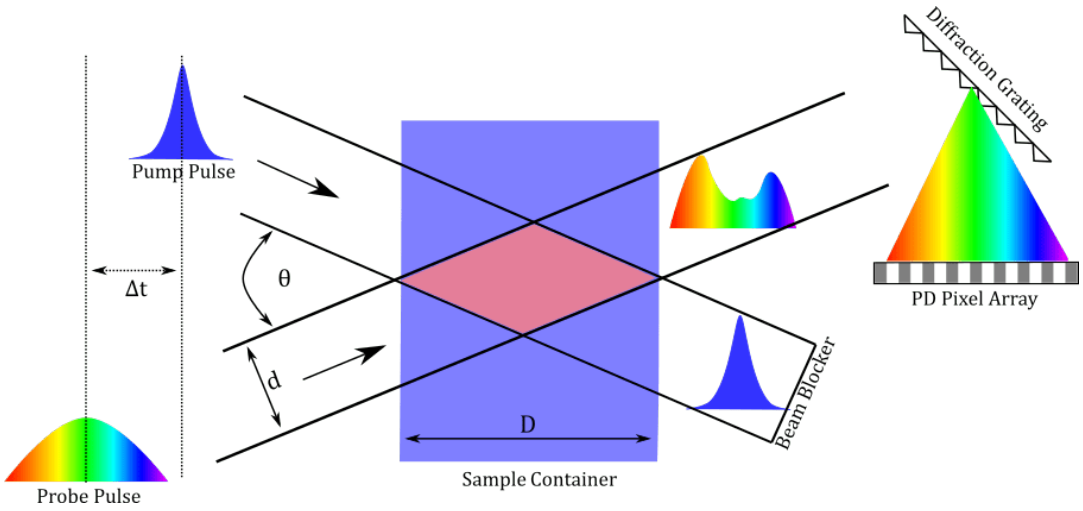

FIGURE 2.4: Overlapping geometry of pump and probe pulses of an equal pulse width. The pulses overlap temporally inside the red triangle near time zero

The laser pulse duration, beam spot size and the overlapping angle between the pump (excitation) and probe beams all have an effect on the temporal resolution of the detection system. When these pulses overlap inside the sample, complex spatial and temporal mixing processes occur. The ideal overlapping geometry has been derived by evaluating the convolution integral of both pulses, subject to constraints for maximum beam interaction and minimal loss in resolution [10]. The result is simplified to a single expression written in terms of the separation angle (θ), sample length (D), the focal spot size of probe-pulse (d) and pulse duration (τ) of the pump and probe beams:

$$D \sin\theta \leq d = c\tau \tag{2.4}$$

The pulse duration and focal spot size of the probe-pulse are fixed variables and only sample container size and overlap angle are variable parameters. The thickness of the liquid sample container ranges from <1 *mm* up to a few *cm*, the choice of which will determine the resulting OD (equation 2.2). Some samples require a longer interaction length, due to constraints in molar concentrations, in order to maximize the number of photo-molecular interactions. Once the container thickness has been decided, all known variables can be substituted into equation (2.4) to determine the correct overlapping angle. The focal spot size of the pump-pulse is often larger ($\sim$ 30%) than the probe to ensure that the probe-pulse path intersects exclusively with excited molecules (figure 2.4).

Sample Preservation

Photobleaching occurs when a fluorescing molecule (fluorophore) permanently loses the ability to fluoresce due to photon-induced chemical damage and cleaving of covalent bonds [52]. Photobleaching has a negative effect on the instrument detection sensitivity as fewer excitable molecules will contribute to the total measured intensity of the probe pulse. The total area of the cuvette is typically much larger than the area where the probe and pump beams overlap, rendering $\sim$ 99% of the sample unused during the measurement. There are various techniques available to reduce photobleaching effects such as placing the cuvette on an X-Y translation stage programmed to move the sample during the experiment, or by using a liquid flow-cell which circulates fresh sample continuously in the sample cell, or for ultra-sensitive experiments one can use a liquid flow jet which suspends a fine sheet of liquid in air without the need of a container.

Chapter 3

Experimental Set-Up

Overview

The National Laser Centre (NLC) at the Council for Scientific and Industrial Research (CSIR) currently houses a CPA-2110 fiber-seeded ultrashort pulse Ti:Sapphire regenerative amplifier laser system which was used in this experiment. In this chapter the term *fundamental beam* refers to the output beam of the laser system, with the following specifications:

Pulse Energy	1 mJ
Average Power	1 W
Repetition Rate	1 kHz
Pulse Width	150 fs
Wavelength	775 nm
Polarization	Horizontal

TABLE 3.1: CPA-2110 specifications obtained from Clark-MXR, Inc [53].

In this chapter a complete overview of the femtosecond transient absorption spectroscopy setup is provided with detailed descriptions of the experimental conditions needed for replication of results. Please see the standard operating procedure (SOP) in Appendix A for instructions on how to safely operate the laser system and other instruments.

3.1 Optical Configuration

The optical breadboard is the working surface for all laser experiments and is typically made from high-grade Aluminum, mounted on vibration isolating surfaces such as thick granite slabs or pneumatic isolators. The working surface is covered with threaded-holes, evenly spaced and manufactured with high precision, so that various optical elements (mirrors, lenses, crystals, etc.) can be mounted and aligned accurately. The complete optical layout of the fs laser laboratory is schematically depicted below. Some of the important components will be discussed in the following sections.

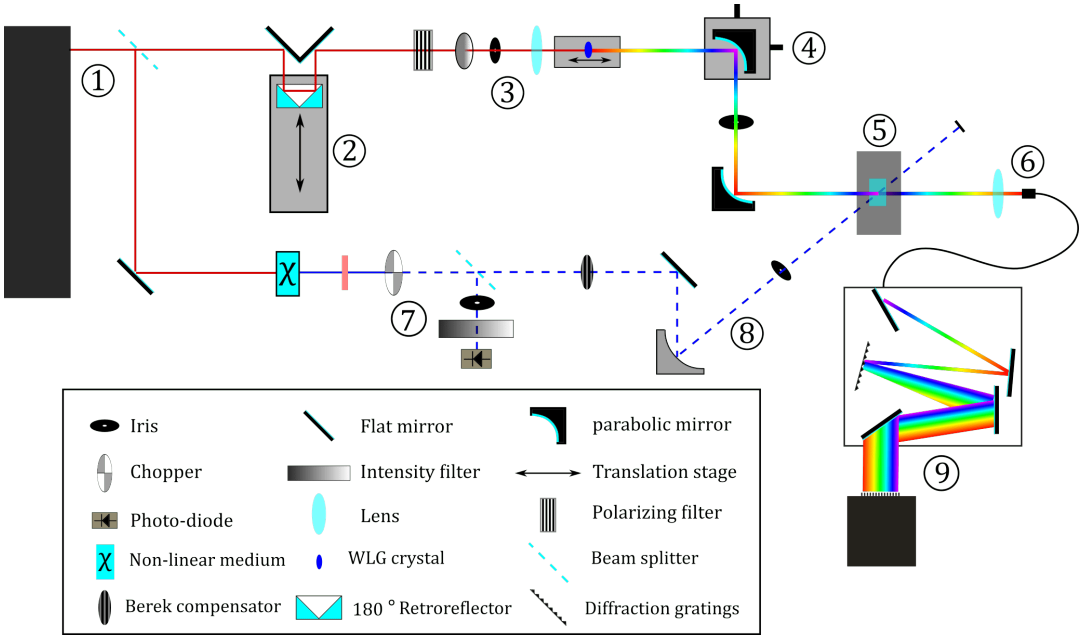

FIGURE 3.1: Optical layout of the pump-probe spectroscopy experiment. ① Fs laser source, ② retro-reflector mounted delay-line, ③ white light generation set-up, ④ 3D-axial collimating mirror mount, ⑤ active sample stage, ⑥ fibre optic input coupler, ⑦ second-harmonic generation and pulse synchronization, ⑧ pump-focusing and overlap geometry, and ⑨ spectrograph set-up with photo-diode array detection system.

3.2 Second-Harmonic Generation and Pulse Synchronization

This section corresponds to component 7 in figure (3.1). At the output of the laser, a beam splitter is used to split the fundamental beam into pump and probe portions. The reflected component ($P(\omega) \sim 300\,mW$) is used as the pump pulse and requires a frequency doubling parametric interaction to attain the correct excitation wavelength in the Soret region ($\pm\,400\,nm$). A 1 mm thin plate of β-Barium borate crystal (type I - phase matching angle $\pm\,32^{\circ}$) halved the incident wavelength of the fundamental pulses from 775 nm to 387.5 nm, while keeping the pulse durations short. The small thickness of the non-linear material induces a negligible amount of temporal pulse broadening $\Delta\tau_{broad} < 1$ fs [54]. The SHG output intensity varies with the square root of the input intensity ($I(2\omega) = \sqrt{I(\omega)}$) and requires a minimum threshold energy before SHG occurs. The conversion process is not 100% efficient and the remaining fundamental light at 775 nm is removed from the beam using a high optical density (OD $\sim$ 6) notch filter which blocks out all light in the 770 - 795 nm region. Thereafter, the repetition rate of the pump-pulse train is halved from 1kHz to 500Hz by an optical chopper to produce pump-on and pump-off states. The chopper is synchronized to the timing of the laser system through the SYNC 1 port on the back of the DT506 controller box. A thin glass plate is used to divert a small portion of the pump beam into a photo-diode (PD) which provides a trigger to the pulse-synchronizer unit to differentiate between pump-on and pump-off measurements. A BNC cable connects the photo-diode directly to the pulse-synchronization unit (see Appendix A). A neutral density filter is positioned in front of the PD to adjust the trigger level to within the correct voltage range ($\sim 250 - 500$ mV). The

trigger levels must be checked and adjusted regularly (before each measurement) as the alignment into the PD and the laser output power may vary with time.

3.3 White-Light Generation (WLG)

White-light generation, discussed in Chapter (2), is a critical resolution-limiting factor and greatly determines the quality of the difference absorption data. In figure (3.1), component 3 shows the required optics, which include (from left to right):

- A linear (horizontal) polarizing plate to remove the small percentage of vertical or randomly polarized light from the fundamental beam.
- Variable neutral density (ND) filter wheel to carefully control the intensity of the incident beam to avoid over pumping and/or burning of the crystal.
- A small iris to control the spot size and to clip the non-uniform outer edges of the beam until a uniform intensity is obtained.
- A doublet (f60) lens, specifically designed to tightly focus the fundamental beam.
- Finally, the non-linear WLG material (YAG, CaF_2 or Sapphire) is mounted onto a mechanical translation stage so that the crystal position relative to the focal point can be carefully controlled.

Optimization

Optimizing the supercontinuum is always necessary before performing any measurements. As a first step, the ND filter should be adjusted to allow only

50% of the beam to be transmitted. By placing a white paper behind the small iris one can check that the intensity of the beam is uniform (no aberrations, diffraction rings or spots should be visible). Using the mechanical translation stage, one should adjust the position of the crystal until the focal point of the beam is inside the crystal material, as close to the back as possible to reduce unnecessary propagation inside the material. Only then should the transmitted intensity of the pump beam be slowly increased (adjusting the ND filter) until a single bright filament is observed (figure 3.2). The `MATLAB Graphical User Interface (GUI)` has a `Raw Data Plot` mode which is useful for making real-time tweaks to the supercontinuum spectrum and to check that there is no excessive self-phase modulation or flickering. The white-light spectrum is considered optimal when it appears visually and graphically stable, while saturating the detector between 15,000 and 35,000 intensity counts. As a last resort, if the stability does not improve, consider making small changes to the Clark-MXR laser D1 and D2 timing unit as there might be an issue with the input and output coupling of the pulses caused by a mistiming of the Pockels cells which can cause temporal jitters.

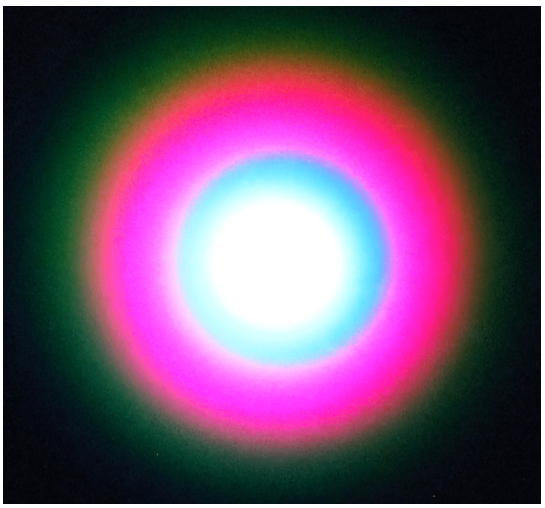

FIGURE 3.2: Optimized white-light filament generated in a 4 mm YAG crystal. The red outer circle is a remnant of the fundamental and should be cropped out using an iris.

3.3.1 Beam Collimation

The WLG setup which is described in this section refers to the recommended and improved low-GVD WLG system which uses a pair off-axis parabolic mirrors and is different to the on which was used at the time of the experiment. The previous WLG setup used thick transmissive optics to collimate and focus the supercontinuum beam which caused the probe pulses to become severely chirped resulting in a strong artifact in the transient absorption spectra near time-zero (will be discussed in the next chapter). The beam

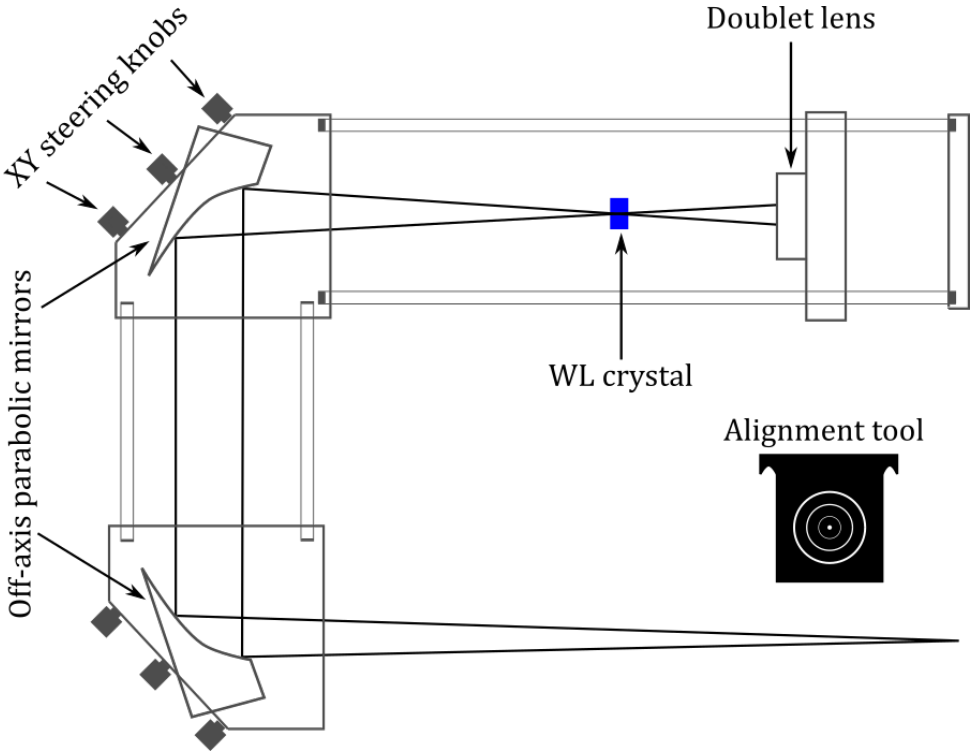

FIGURE 3.3: Diagram depicting the optical configuration of the WLG cage system.

that emerges from the WL crystal is spectrally broad and diverging. The beam is collimated and re-focused to pass through the sample using a pair of 90° off-axis parabolic mirrors that have dielectric silver coatings to compensate for GVD effects (figure 3.3). The parabolic mirrors and focusing doublet lens are mounted in a special cage system specifically designed to fix their positions at the correct focal distances. The collimating parabolic mirror has

a focal length of 10 cm, which is slightly longer than the 6 cm focal length of the doublet lens to increase the spot size of the WL so that it can be tightly re-focused. Once probe pulses interact with the sample there is no need to be over-stringent in the placement of specialized low-GVD optics. Since the detectors only record the average intensity of the probe pulses one does not need to preserve the temporal properties of the pulse for the remainder of the optical path, after the sample. The recommended method for aligning the WLG cage system is as follows:

- Remove the WL crystal from the system.
- Place the alignment tool onto the cage and make slight vertical and horizontal adjustments to the supporting posts until the cage is completely level, i.e. until the beam propagates through the centre of the alignment tool iris at every point along the cage and the input beam is well aligned to pass through the centre of the doublet lens. A small spirit level is also useful to establish a rough alignment before using the alignment tool.
- Loosen the "lock" screw on the back of the second off-axis mirror (the one that re-focuses the WL beam). Slowly and gently remove the mirror from the housing (held in place by magnets) and keep in a safe place.
- Place the WL crystal at the focal point of the doublet lens and adjust the ND filter and iris until a stable WL is generated (described in the section above) and collimated by the first off-axis parabolic mirror. Allow the WL beam to reflect off the collimating mirror into the far field (onto the wall $\pm$ 1 m). The appropriate far field alignment distance should be greater than the distance measured from the WLG crystal to the detector.
- Adjust the XY steering knobs on the collimating mirror mount until the projected WL beam is circular (figure 3.2). In cases where alignment

is especially bad, the WL beam will appear in the far field as highly astigmatic (folded).

- Return the focusing off-axis parabolic mirror to its original position. Use the number of magnets on the mirror mount (one side has 2 magnets and the other has 3) to correctly align the mirror into the housing and tighten the "lock" screw. Use the XY steering knobs of the mirror mount to make small adjustments to the WL spot in the far field behind where the sample would normally be. If the WL spot remains circular after the focal point then the setup is considered well aligned.

3.4 Active Sample Stage

The time duration of a typical pump-probe measurement can vary from 30 mins to a few hours. The pump and probe focal spot-sizes in relation to the total sample area is less than 1%. In order to minimize the negative effects caused by continuous illumination of the same sample region during a measurement, a programmable X-Y translation stage was built to continuously move the sample cuvette for the duration of the experiment. A ThorLabs motorized stage provided the horizontal motion onto which a linear rail stepper motor was mounted to provide the vertical motion. The linear rail translation stage was home-built with parts common to 3D printing systems, and the stepper motor was controlled using a `Synertronic Designs` controller module. The horizontal and vertical stages are controlled by two independent user interfaces, `ThorLabs - Kinesis` (horizontal stage) and `Synertronic Designs - Uragan Studio` (vertical stage). By programming each stage to move back and forth with different acceleration and velocity parameters, the resulting X-Y motion is completely arbitrary.

3.5 Detection System

The detection system as a whole, leading up to the final measurement (i.e. integration of the pixels to record the transmitted intensity) is not limited to the CMOS photo-diode sensors but includes other important peripheral instruments and devices such as; fibre cables and couplers, spectrograph, and pulse digitizer, all of which can be resolution limiting processes if left unchecked.

3.5.1 Fibre Coupling and Spectrograph

Components ⑥ and ⑨ in figure (3.1) represent the location of the fibre cables and spectrograph within the setup. The fibre cables are used to guide the probe beam, after interaction with the sample, into the spectrograph where the supercontinuum is linearly dispersed into spectral components using a diffraction grating. Transporting the multi-wavelength probe beam in this manner can become problematic because the transmission properties of fibre cables are not consistent over a large spectral region. Fibre cables are also known for inducing dispersion, especially for supercontinuum uses (the longer the cable the greater the dispersion). The intensity and shape of the transmitted beam are highly dependent on how well the beam is coupled into the fibre cable. Ideally, the divergence of the probe beam should match the recommended numerical aperture rating of the fibre cable (0.1 NA in this case). This is especially difficult when performing probe and reference measurements because both channels need to transmit light identically. For this reason, rather than using fibre guides, many pump-probe set-ups focus the probe beam directly into the spectrograph.

The spectrograph is a stand-alone unit supplied by `CDP Systems` and is operated by computer software. The system has an automated rotating turret

which allows the user to switch between two separate gratings centred at different wavelengths for the NIR ($\sim$ 900 nm) or visible ($\sim$ 500 nm) spectral regions, respectively. The central wavelength position of the turret can be changed from the `MSI 2001i` desktop application. Importantly, when changes are made to the central wavelength position of the grating in the `MSI 2001i` application the centre wavelength value in the `MATLAB GUI` must be manually updated. The inner mirrors of the spectrograph are fixed in position and adjustments (up, down, left or right) to the output position of the beam is made by altering the position of the fibre cable at the input of the spectrograph using the X-Y mount.

Optimization and Calibration

The numerical aperture of the fibre cable (0.1 NA) was specifically chosen to match the numerical aperture requirements of the spectrograph in order to function correctly. If the probe beam is focused at the correct acceptance angle into the fibre cable it will emerge as a uniform circular beam, diverging at an angle equal to the incident ($\Theta_{in} = \Theta_{out}$). To optimize, place a white paper at the output of the fibre and make small adjustments to the position of the input coupler (X-Y axis mount) until the light emerges as a circular beam with a uniform intensity (no diffraction rings or aberrations). If the light is focused correctly into the spectrograph then the orientation of the dispersion gratings will disperse the beam at a specific wavelength per mm value, determined by the dispersion curve of the grating being used. By knowing the number of pixels on the photo-diode array (pixels per mm) the wavelength per pixel correlation could be determined and programmed into the `MATLAB` software to automatically recalculate the wavelength scale. Final calibration to the wavelength axis can be made by using notch filters (which transmit a specific narrow region in the spectrum) or a well-characterised dye

such as rhodamine or porphyrin to offset the wavelength scale, if necessary (done within the `MATLAB UI`).

3.5.2 Camera Synchronization

The photo-diode array (PDA) uses CMOS semiconductor technology and is sensitive to photons across a broad wavelength range (400-1000 nm). The PDA is installed at the output of the spectrograph so that the linearly dispersed light falls across its entirety. In order to record and differentiate between single pulses ($\Delta\nu$ = 1kHz and Δt = 1ms), the system needs to be synchronized to the exact timing of the laser system. The timing structure of the system can be explained with the aid of a flow diagram shown in figure (3.4).

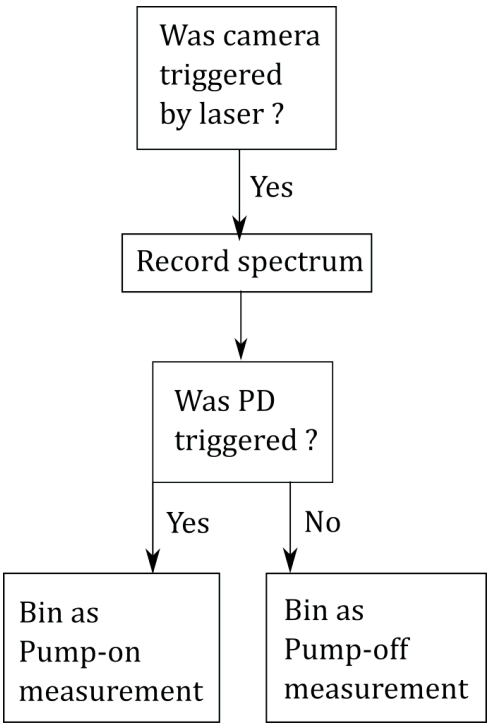

FIGURE 3.4: Signal level flow diagram for triggering of devices and sorting of measurements.

As mentioned previously in Section (2.2), each $\Delta A(\lambda, t)$ calculation requires one pump-on and one pump-off measurement to perform the necessary division in equation (2.2). The `Clark-MXR` laser provides a trigger-out port (labelled as SNYC 1), on the back of the DT-506 controller box, and is directly correlated to the fundamental pulse train frequency. Direct synchronization to the system is important because the laser repetition rate can vary over time between 999-1001 Hz. The laser trigger-out is connected directly to the trigger-in port on the back of the PDA device. As discussed in Section (1.2), a 500Hz pump-on trigger is generated at component ⑦ in figure (3.1) which

connects to the channel 1 port on the pulse digitizer unit. The time it takes for the trigger signal to travel from the DT-506 box to the camera inside the BNC cable is not equal to the time it takes for the laser pulse to physically transverse across the optical table at the speed of light and strike the camera. To account for the mismatch, a time-delay value is determined (see Appendix A) to account for the relative delay so that the trigger arrives before the pulse. Once the camera receives a trigger from the DT-506 box it waits for a specified delay time before collecting pixel values over a window period of 1 μs before the final integrated data is exported to the pulse synchronization box. During the 1 μs window period, if the pulse synchronization unit receives a trigger from the PD then it will associate the imported data as a pump-on measurement and save it accordingly; if no trigger is received during this window then it will be binned as a pump-off measurement. This process is repeated until a desired number of scans have been completed (i.e. 1000 scans = 500 pump-on + 500 pump-off) and finally the .dat array (size = pixels $\times$ scans) exported to the CPU for processing in `MATLAB`.

3.5.3 Pulse Rejection and Power Fluctuations

In theory, it is assumed that each probe pulse (corresponding to pump-on and pump-off states) is identical for each measurement. In practice, however, this is not the case and the pulse-to-pulse intensity and resulting signal to noise ratio (SNR) can fluctuate significantly (depending on the state of the laser system). Pulse rejection algorithms are commonly used to reduce system noise by actively rejecting measurements obtained for pulses that fall below a certain intensity threshold value. This can be done by monitoring the trigger levels from the PD (component 7 in figure 3.4) on an oscilloscope. Once a pre-set number of scans have been completed, the synchronization unit exports an array of PD values that correspond to the pump-pulse intensity for

each pump-on measurement. This data is then analysed element-by-element to reject measurements associated with the problem pulses. Another computationally less demanding method is to average the final PD values obtained for all the scans and then normalize/scale the difference absorption spectrum accordingly. Testing both of these algorithms under conditions of severe laser instability (intensity fluctuations >1%) yielded very similar results; in both cases the final ΔA spectrum showed the same degree of improved stability between time steps with reduced intensity fluctuations. However, the pulse-to-pulse sorting algorithm more than doubled the computational time required to perform the set number of scans. The PD averaging/normalization method did not have a noticeable effect on the measurement time. Performing the same tests again, but this time with a stable laser system (intensity fluctuations <0.01%), showed that the system performed better without the use of either the averaging or pulse sorting algorithms. This is possibly due to the internal error margin of the PD exceeding the OD resolution of the measurement ($< 1\times10^{-5}$ OD). Thus, it is recommended that the PD normalization algorithm is only used when the laser stability is not operating optimally or when conducting measurements that do not require high sensitivity ($> 1\times10^{-3}$ OD).

3.6 Graphical User Interface

The hardware components-dual CMOS PDAs, pulse digitizer unit and delay-line drivers-are supplied with a comprehensive list of `LabVIEW` executable .lib script files and .dll drivers to control the hardware remotely through a USB 3.0 connection. We decided to use `MATLAB` rather than `LabVIEW` for the final user interface because computationally `MATLAB` is faster and better suited for handling large arrays of data with the least amount of code required. One

drawback is that only `MATLAB 2015b` and older versions support access to shared C# dynamic-link library files (.dll) with very specific PC requirements such as `Win7 OS, .NET 4.5` framework and software development kit package $\texttt{SP}_1$. Once the .dll libraries are loaded successfully into `MATLAB` using the `"loadlibrary('GlazLib')"` command, all loaded executable functions can be viewed using `"libfunctionsview('GlazLib')"`, all the executable functions become callable through `"calllib"` and require a very specific pointer structure to work correctly. For example, the function that retrieves the vector containing all the pixel values of a measurement is called by the `"GetResult"` function and requires a pre-defined pointer of the correct size (1x2048) and data type (double) to pass through the function and extract the data.

XML Script Configuration

The `Synertronic Designs` © detection system makes use of flexible `XML` script files that define all camera calculations and pre-processing steps that need to be performed on the PC such as background subtraction, pixel calibration, pulse sorting, inverse Fourier transform, computational tasks (+,-,÷ and ×) and other initialization parameters. Consider figure (3.5) as an exam-

```
<config>
  <camera reverse="1" master="1" number="1" serial="SYBP012010003"/>
  <pd ch1="1" number="1" serial="SYBP006010009" window="10"/>
  <preprocessor camera="1" type="subtract_background"/>
  <calculation gatestate="1" name="PumpOn" pdgate="1:1">
    <measurement camera="1"/>
  </calculation>
  <calculation gatestate="0" name="PumpOff" pdgate="1:1">
    <measurement camera="1"/>
  </calculation>
</config>
```

FIGURE 3.5: Example of an XML script file.

ple of an XML file that performs a background subtraction (pre-processing) followed by a single camera measurement with pump-on (`gatestate = "1"`)

and pump-off (`gatestate = "0"`) binned states. Once the script file is executed the system stores the `PumpOn` and `PumpOff` measurements separately, which can then be accessed by `MATLAB`. As it turns out, performing the $\frac{I_{Pump-On}}{I_{Pump-Off}}$ division within the XML script file is not always successful. This is because some of the pixel values in the $I_{Pump-Off}$ array contains float values tending close to zero, which results in the subsequent division returning NaN (not a number) errors which crash the program. To avoid this error from occurring, the final division and logarithmic transformation is performed within `MATLAB` where it has a larger float memory.

MATLAB

`MATLAB 2015b` comes with built-in applications such as `GUIDE` (GUI development environment), which can be used to design user interfaces for custom laboratory applications. Using the `GUIDE` Layout Editor, one can graphically design one's own UI features such as push buttons, interactive plots, tables and much more. Once the UI is created in the Layout Editor, `GUIDE` automatically generates the `MATLAB` code for constructing the framework of the UI which can then be edited as required to perform specific functions. The features included in the pump-probe experiment UI were inspired by existing transient absorption spectroscopy software (`ExciPro`, feedback from fellow researchers and personal experience. After months of coding, testing, troubleshooting and debugging, the final user end-product is presented below in figure (3.6). The main UI features are highlighted and discussed below:

① **Plot Window**

The plot window is the focal point of the UI and is used to graphically display various forms of data, depending on what the user has selected, in real time, or it can be used to view data from previously saved measurements. The plot window has a few interactive features

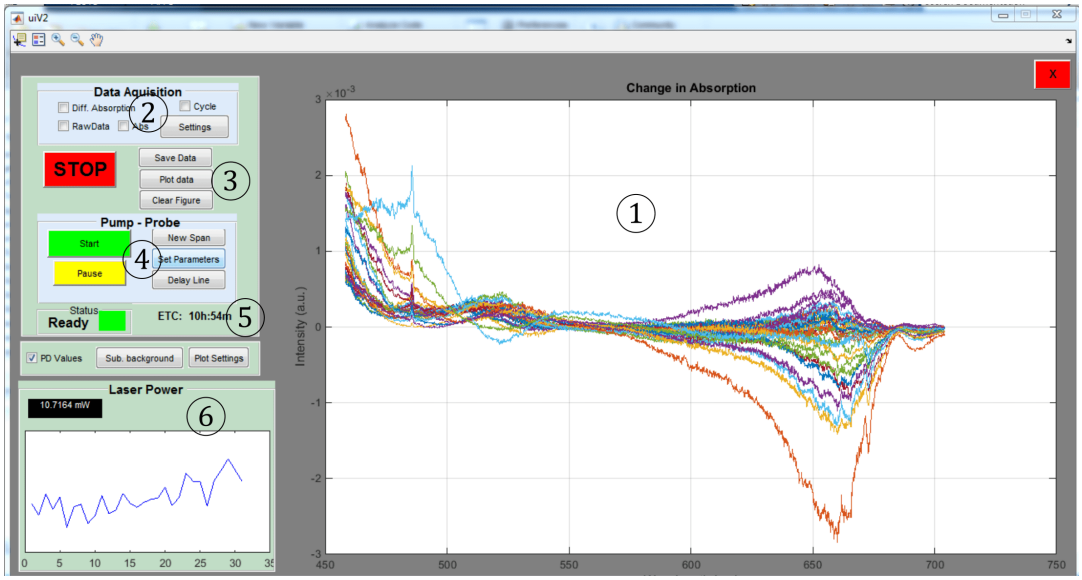

FIGURE 3.6: A screen grab of the femtosecond transient absorption spectroscopy UI developed with `GUIDE` to control the Syntronic Designs© hardware. Relevant components have been numbered for referral later on.

(located in the top left tool-bar) to assist with visual inspection of the data by resizing the display area to focus on a specific region, and/or to quantitatively inspect the data by using the data tool to probe values.

② Data Acquisition Tab

The first step in any pump-probe experiment is careful optimization of the detection system, which includes the quality of probe beam (white light generation), overlapping of pump-probe pulses, locating temporal overlap, coupling the probe light into the fibre cable, and detector saturation levels. There are two data feedback options under the `Data Acquisition Tab`, namely `RawData` and `Diff.Absorption`, accompanied with a `Cycle` check-box and a `Settings` push-button. Pressing the `Settings` button opens a dialogue box which allows the user to edit the system initialization parameters such as Dual or single camera modes, scan count, central wavelength, integration time, trigger delay time, pixel binning and clock-speed (scan-rate). For general use, it is recommended that the default settings are used.

When the `RawData` box is checked, the plot window will display the raw pixel intensities (Y-axis) corresponding to each pixel (X-axis) and will continuously be updated after the defined number of scans are completed. Typically, the scan count is set to 1000 scans, which equate to a 1-second interval (repetition rate = 1 kHz). This mode is particularly useful for optimizing the white-light spectrum by monitoring the plot window while making small adjustments to the WLG optical components and input fibre coupling until the saturation levels across the detector are between 40-60% (25,000-35,000 counts) and stable. When using the dual camera mode, for probe and reference beams, the pixel intensity spectra of both cameras are plotted simultaneously so that adjustments to fibre couplings can be made until both probe and reference beams saturate the detectors equally. Only the `STOP` button can be used to terminate the measurements: once `STOP` is pressed the check-box will automatically become deselected but the plot window will hold the last recorded spectrum. `Clear Figure` resets the plot window. When the `Diff.Absorption` check-box is ticked, the system performs a single ΔA measurement and is displayed in the plot window. If the `Cycle` check-box is ticked before activating `Diff.Absorption`, the system will continuously perform a ΔA measurement and display the result in the plot window until the loop is terminated with the `STOP` button. If there is no sample in the path of the probe beam, the recorded ΔA signal would represent the detection or optical density resolution of the system and is a good way to characterize the capabilities of the set-up before performing a measurement. The `Diff.Absorption` feature can also be useful for making small adjustments to the delay-line position (using the `Delay-Line` interface) until the exact location of time-zero is observed. A more general approach to finding the location of time-zero is discussed below.

③ **Data Tools**

To save the current `Raw Data` or `Diff.Absorption` data being displayed in the plot window the `Save Data` button should be pressed. To plot any data that has been previously saved, press the `Plot Data` button should be pressed to open a file navigation window, from which, one can then navigate to the specific file one wishes to display. `Clear Figure` resets the plot window.

④ **Pump-Probe Tab**

After the setup has been optimized using the `Data Acquisition Tab` the system is ready to perform Pump-Probe measurements. The `Pump-Probe` tab contains five press buttons:

New Span - Opens the `SpanSetting` dialogue box. The rows represent the span number (1-6) and the columns represent the start, step and stop time values (in ps) for each span number (see Appendix A). The values are stored once the `Save` button is pressed at which point a dialogue box will appear prompting the user to enter a unique span filename. The `Reset` button clears all entered values.

Set Parameters - The `Set Parameters button` is used to enter/alter various experimental parameters including, the central wavelength, number of scans, span filename, pixel binning, clock-speed, and single or double camera mode. `Ok` accepts the initialization parameters (see Appendix A).

Delay Line - The `Delay line` button launches the a stand-alone UI which allows for full control over the delay-line. To summarise, the delay-line UI can be accessed at any time (except for during a pump-probe experiment) and is used to accurately control the position of the

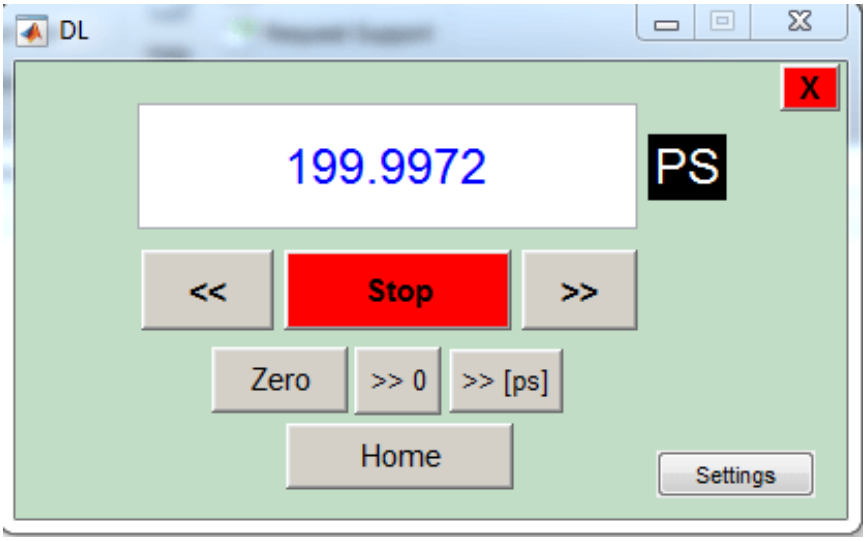

FIGURE 3.7: Delay-line user interface (see Appendix A for instructions).

delay line when looking for time-zero. When time-zero has been located (not always an easy task), the `Zero` button saves the exact location for future use. The `»0` button moves the delay-line into the previously stored zeroed position. `Home` moves the delay-line to the start limiting switch position and which also re-calibrates the delay-line system.

Start - Starts the pump-probe measurement.

Pause - Pauses the pump-probe measurement. The measurements will resume when `Ok` is pressed.

⑤ **Experiment Status**

There are four types of colour indicators that each represents the current state of the system:

`Green` - Ready. The system is ready to perform a measurement.

`Amber` - Delay-line. The delay-line is busy.

`Yellow` - Paused. The measurement has been paused.

`Red` - Busy. The camera is busy.

During a Pump-Probe measurement, an estimated time of completion (ETC) text will become visible. The ETC is an estimated time (local time) for when the measurement will be 100% completed.

⑥ **Laser Power Feedback**

The time duration of a typical Pump-Probe measurement can vary from a few minutes to a few hours. During this time, the output intensity of the laser typically fluctuates, especially over long periods, which can have negative effects on the outcome of the experiment. To keep track of the laser stability during the experiment, the PD values of the pump-pulse are recorded and plotted for each time-step and indicates the average pump-pulse excitation energy (mW) received by the sample. Once a measurement has run to completion, the pump-pulse PD values are automatically exported as a .dat file. If need be, this data can be used to explain any artifacts in the data which are related to an increased or decreased pump-pulse energy.

System performance

The new system was used by other MSc students to perform pump-probe spectroscopy with outstanding results. Figure (3.8) shows some raw time-resolved difference absorption data viewed in `GloTaRan`, showing the system capabilities using liquid (left) and solid-state (right) samples, respectively.

Figure (3.8) demonstrates the quality and capability of the pump-probe system which I built. The new system achieved remarkable resolution levels and could easily resolve changes in the difference absorption data as little as 0.1 mOD (achieved using 2000 scans), nearly two orders of magnitude better than the previous `ExciPro` system which was

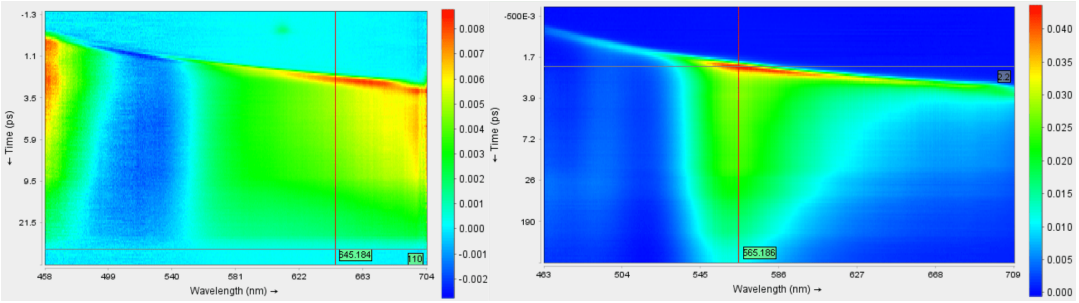

FIGURE 3.8: Time resolved pump-probe data obtained with the new set-up of a hematite coated on a silica substrate (right) and a heavy metal chromophore in hexane solvent (left). Data graphically displayed using `GloTaRan`.

purchased from `CDP Systems` in 2009. The new system offered many unique improvements such as a 50% reduction in measurement time, with close to 10× improved spectral resolution, full access over camera parameters and true raw data output (see Appendix A).

Chapter 4

Results and Discussion

Materials and sample preparation

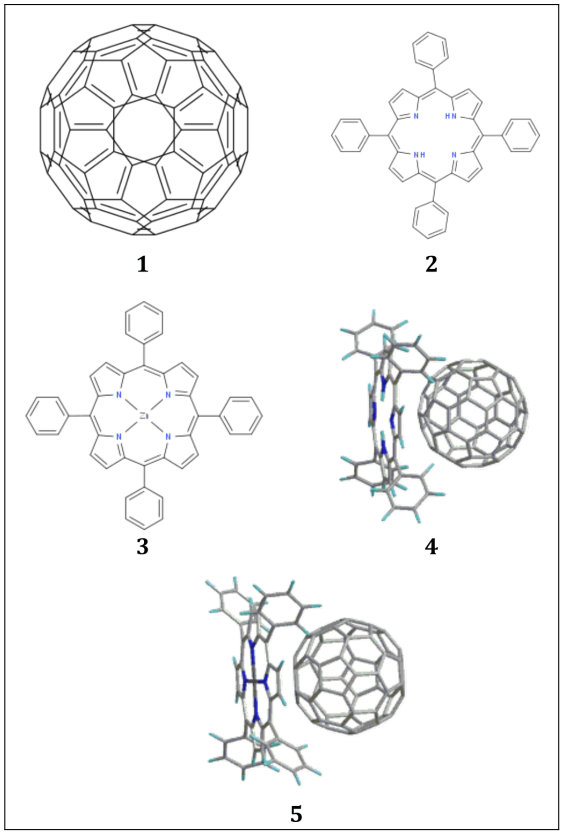

FIGURE 4.1: Molecular diagrams of pristine C_{60} (**1**), TPP (**2**), ZnTPP (**3**), TPP-C_{60} (**4**), and ZnTPP-C_{60} (**5**). Structures (**1** − **3**) were obtained from the ChemSpider free online database. The optimized structures (**4** − **5**) were generated using DFT modelling software `Turbomole 6.5`, reprinted with permission from [55] (Copyright 2015, Springer-Verlag Berlin Heidelberg).

The molecular compounds (powder form) of tetraphenylporphyrin (TPP), zinc tetraphenylporphyrin (ZnTPP), fullerene (C_{60}) and toluene solvent (99.98%) were purchased from Sigma-Aldrich at high purity and did not require additional purification protocols prior to use (figure 4.1). The porphyrins and fullerene were weighed and dissolved in toluene at higher concentrations ($1X10^{-4}$ M) before immediately being diluted into weaker concentrations. The solutions were stored in amber glass bottles with Teflon caps to reduce photo-induced degradation and plastic contamination (toluene reacts with all types of plastics except for PTFE). An algorithm was coded in `Python` to accurately determine the correct D-A mixing ratios. The input parameters for the program are the; type of donor (TPP or ZnTPP), dry sample weight (as measured on the balance scale), the desired volume of stock solution, and final sample volume (cuvette volume). Once these parameters are entered the `Python` program returns a mixing equation:

```
565 (C60) + 38 (ZnP) + 1397 (solv) = 2000 [microL]
```

The mixing equation contains the exact volumes to pipette from each stock solution. In this way, the accuracy of the donor-acceptor concentrations could be ensured for each iteration of the experiment. Both zinc and free-base porphyrins easily dissolve in toluene at room temperature within a few minutes. Fullerene, however, was left for up to 24 hours to dissolve completely. Using sonication or magnetic stirring to speed up the dissolving process was not adopted as it may lead to aggregation of C_{60} [56]. Both porphyrins and fullerene are susceptible to forming aggregates, even at low concentrations, which can affect the formation of the D-A complex [57]. Hence, the measurements were performed well below the critical aggregation concentrations of fullerenes and porphyrins. The final porphyrin and fullerene concentrations were 2×10^{-6} M and 5×10^{-5} M, respectively.

4.1 Absorption and Fluorescence Spectroscopy

UV/Visible ground-state absorption and steady-state fluorescence spectroscopy were performed to characterise the photophysical properties of the donor-acceptor complexes (figure 4.1). The absorption and fluorescence data were obtained using a Varian Cary 100 Bio UV VIS Spectrophotometer [58] (with solvent baseline subtraction) and a Horiba Fluoromax-4 Spectrofluorometer [59]. The samples were freshly prepared and careful steps were taken to avoid aggregation. Both spectroscopic measurements, absorption followed by fluorescence, were done consecutively in the same quartz cuvette (10 mm path length) to eliminate the possibility of cross-contamination of porphyrins.

4.1.1 Tetraphenylporphyrin

Ground-State Absorption

The ground-state absorption data of the TPP-C_{60} complex and the individual moieties are shown in figure (4.2). The absorption spectrum of TPP only (blue) shows a characteristic narrow peak in the Soret (B-band) region at 419 nm and represents a strong transition from the ground to the second electronic energy levels $S_0 \rightarrow S_2$. The next set of 4 distinct peaks appears in the Q-band region (500 - 650 nm) and is split into separate Q_x and Q_y singlet electronic states. The first and most intense of the four Q-band peaks appears at 514 nm and is assigned to the $Q_y(1,0)$ transition, where the number in parenthesis (u,l) indicates the vibrational mode which was populated in the upper u electronic state to or from a specific vibrational mode in a lower l electronic state [60].

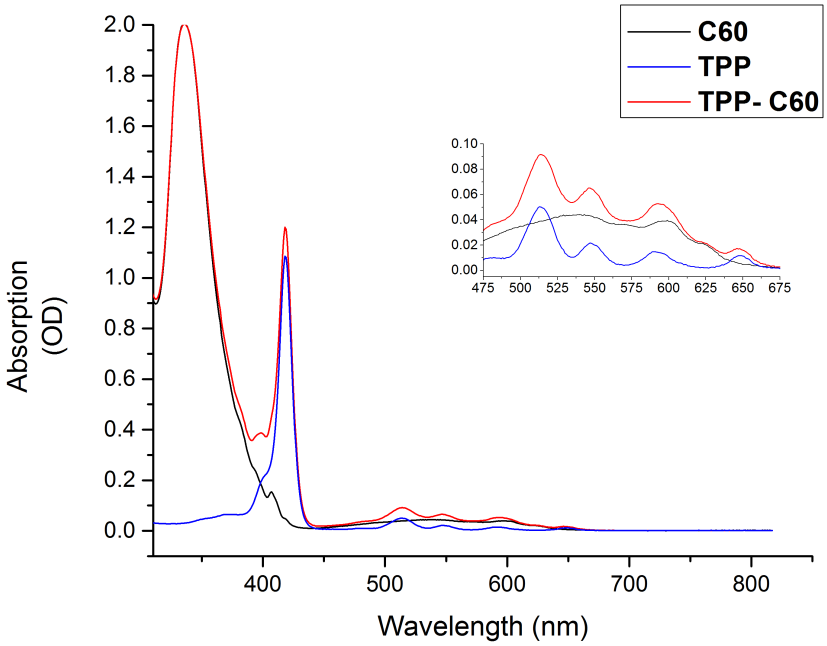

FIGURE 4.2: UV/Visible absorption spectra of C_{60} (black), TPP (blue) and C_{60}-TPP (red) in toluene solvent. Figure inset represents an enlarged view of the Q-band region between 475 - 675 nm.

Adjacent to the first Q_y transition at 514 nm, a second less intense peak appears at 549 nm and represents a $Q_y(0,0)$ transition from the lowest vibrational level in S_0 to the lowest vibrational level in S_1. Extending to the Q_x band region, two $S_0 \rightarrow S_1$ transitions appear at 593 nm ($Q_x(1,0)$) and 648 nm ($Q_x(0,0)$), respectively (see figure 4.2 inset), in good agreement with literature [61]. The ground-state absorption of C_{60} fullerene (figure 4.2, solid black) is dominated by two intense peaks in the deep UV region at 335 and 288 nm, respectively. The first peak at 288 nm is mainly caused by absorption of the toluene solvent and therefore has been cut-out of the spectra. The 335 nm peak is characteristic of fullerene and depicts a large absorption cross-section related to a $S_0 \rightarrow S_1$ transition, therefore, excitation of C_{60} in toluene by UV light populates the first excited singlet state S_1 [62]. A broad absorption band is also seen in the region between 475 - 600 nm (figure.4.2 inset), with

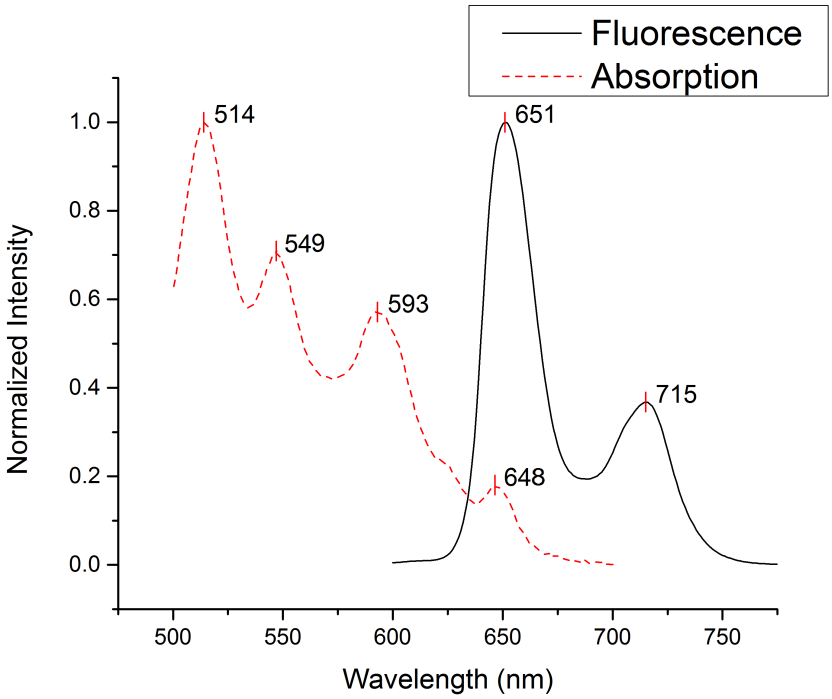

FIGURE 4.3: Normalized steady-state fluorescence emission spectrum (λ_{ex} = 420 nm) of TPP plotted (solid black) against the normalized steady-state absorption spectrum of the Q-band region (dashed red). The peak positions are indicated (in nm) and were determined using `Origin - Peak Analyser`.

an amplitude <2% than the maximum 335 nm S_1 peak. The broad ground-state absorption band occurs at energies lower than S_1, thus, it is most likely caused by absorption to a higher vibrational mode in S_0. In the absorption spectra of the supramolecular complex TPP-C_{60} (figure 4.2, solid red), absorption peaks of the Soret and Q-bands were observed with no evidence of peak positions having shifted, broadened, or any reduction in the absorption cross-section, suggesting that the electronic landscape and photophysical properties of both C_{60} and TPP were preserved during the formation of the compact D-A complex (centre-to-centre distances of only 2.7 Ångström).

Steady-State Fluorescence

In figure (4.3), the fluorescence spectrum of TPP shows two emission peaks occurring at 651 and 715 nm, respectively. The wavelengths of these two emission peaks are redshifted compared to $Q_x(0,0)$, suggesting that both peaks are attributed to emission from the lowest vibrational mode in S_1 to the lowest and first vibrational modes of the ground state i.e. $Q_x(0,0)$ and $Q_x(0,1)$. A Stokes shift of 5 nm is visible between the absorption and emission peaks of the $Q_x(0,0)$ transition. A detailed ultra-fast fluorescence investigation of tetraphenylporphyrin (TPP) by Baskin et al. [60] reported that in non-polar solvents, such as toluene, a small Stokes shift of the main emission peak is mainly caused by a solvent re-organization and thermal equilibration with the environment. No emission peaks could be attributed to the Q_y bands, a result which corresponds with literature that the Q_y excited states undergo rapid non-radiative relaxation to the Q_x bands, leading to ISC to form a long-lived triplet (T_1) state [60]. A weak (< 1% of maximum) fluorescence emission peak was observed at 454 nm and could possibly represent emission of the Soret peak at 419 nm to the ground state, this would, however, imply an unrealistically large Stokes shift of 35 nm. A recent article by Steer [63] addresses the common incorrect assignment of the $S_2 \rightarrow S_0$ emission in porphyrins and concluded that when a large Stokes shift occurs it is typically due to the formation of an aggregate state or impurities and is not true emission of the S_2 state. Comparing the emission data of TPP-C_{60} with that of the TPP moiety (figure 4.20), the spectral positions of the emission peaks coincide exactly at 651 and 715 nm but with a small reduction in the fluorescence peak intensities of 5,9% and 2,8%, respectively. The small amount of fluorescence quenching in TPP-C_{60} is possibly caused by a reduction in the electron population of higher electronic states. This can be

explained by electron-transfer occurring from Q_x to C_{60} leading to the formation of the charge-separated [$TPP^{+\bullet}$-$C_{60}^{-\bullet}$] state. Solvation effects, i.e. interactions between the complex and the solvent environment, can also reduce the emission intensities of the Q-bands.

4.1.2 Zinc Tetraphenylporphyrin

Ground-State Absorption

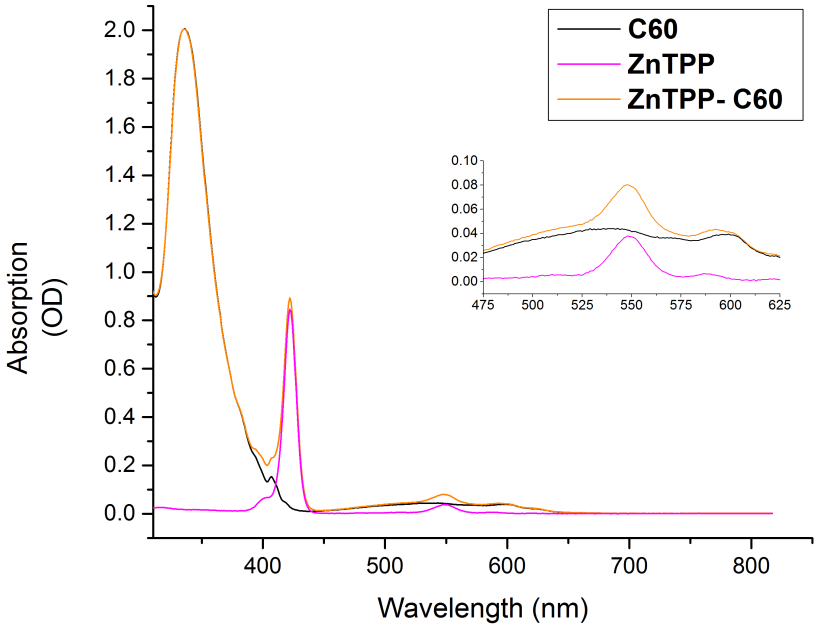

FIGURE 4.4: UV/Visible absorption spectra of fullerene (black), zinc tetraphenylporphyrin (magenta) and fullerene-zinc tetraphenylporphyrin (orange) in toluene. Figure inset represents a magnified view of the Q-band absorption region between 475 - 650 nm.

The ground-state absorption spectra of metal-porphyrin (ZnTPP) showed an intense $S_0 \rightarrow S_2$ transition in the Soret region at 422 nm (figure 4.4). At longer wavelengths, two Q-band $S_0 \rightarrow S_1$ transition peaks appear at 549 nm and 589 nm, corresponding to $Q(1,0)$ and $Q(0,0)$, respectively, in good

agreement with literature [64, 65]. The presence of the zinc metal in the centre of the porphyrin emphasises transitions between the two highest filled molecular orbitals and the lowest empty doubly degenerate anti-bonding orbital, thus, resulting in the intense B-band where the transition dipoles add constructively, and a weaker Q-band where the transition dipoles interfere destructively [57]. Ground-state absorption features of the supramolecular complex ZnTPP-C_{60} recovered all major peaks with no apparent spectral shifting, broadening, decreased absorption cross-section or formation of any intermediate states, as a result of the donor-acceptor complex formation.

Steady-State Fluorescence

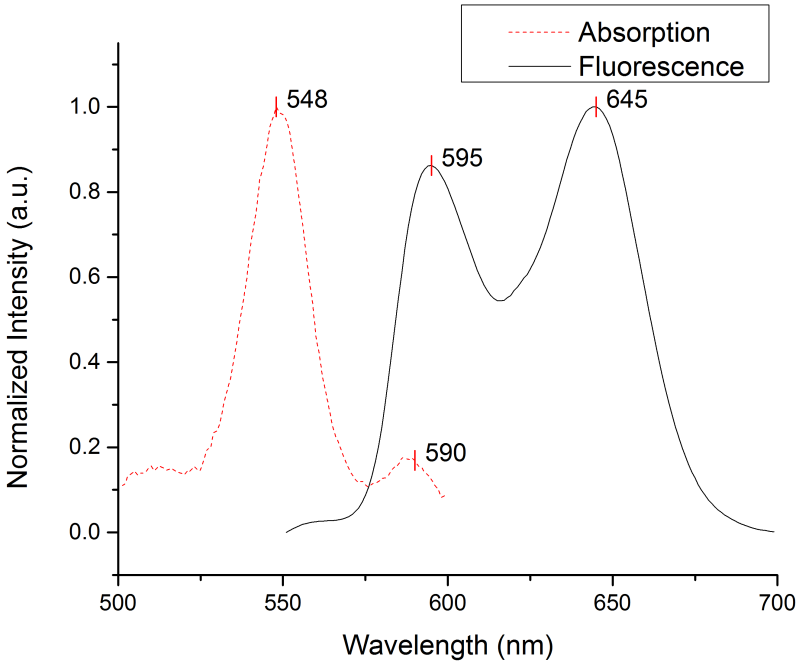

FIGURE 4.5: Normalized steady-state fluorescence emission spectrum (λ_{ex} = 400 nm) of ZnTPP (solid black) and the normalized steady-state absorption spectrum of the Q-band region (dashed red). The peak positions are indicated (in nm) and were determined using `Origin 9.0 - Peak Analyser`.

In figure (4.5), the absorption and emission spectra of zinc-substituted porphyrin (ZnTPP) are shown. At first glance, two strong emission peaks are seen at 595 and 645 nm, respectively, and occur at wavelengths energetically lower than the absorption of the Q-bands. The first emission band represents a $Q(0,0)$ transition and is Stokes-shifted by ± 5 nm to the right of the corresponding $Q(0,0)$ absorption transition. This small Stokes shift can be explained by the non-polar toluene solvent interacting with the complex. The second emission peak occurs 55 nm to the right of the nearest ground-state absorption feature, thus making it too large a difference to be a Stokes-shift process. Research done by Yu et al. [64] assigned this emission peak to a transition from the lowest vibrational level in S_1 to a higher vibrational level in the ground state, i.e. $Q(0,1)$. Comparison of the emission spectrum for the ZnTPP moiety and ZnTPP-C_{60} complex (figure 4.21) showed no change in emission peak positions, as was the case for TPP and TPP-C_{60}, with a small reduction in the fluorescence peak intensities of 5.6% and 2.5% for the 595 and 643 nm peaks, respectively. The exact mechanism of the quenching process is not exactly clear but it can be speculated that the electron transfer processes occurring between ZnTPP and C_{60} resulted in reduced S_1 electron population thus contributing less to the fluorescence spectrum.

4.1.3 Jablonski diagrams

Using the information gathered in the fluorescence and emission data, Jablonski diagrams could be constructed (figure 4.6) to schematically represent the various radiative energy pathways of free-base and zinc-metal porphyrins. The Jablonski diagram of C_{60} is not drawn because in the context of artificial photosynthesis it only acts as an electron acceptor and is not, purposefully, subject to direct excitation from the ground state. The Jablonski diagram

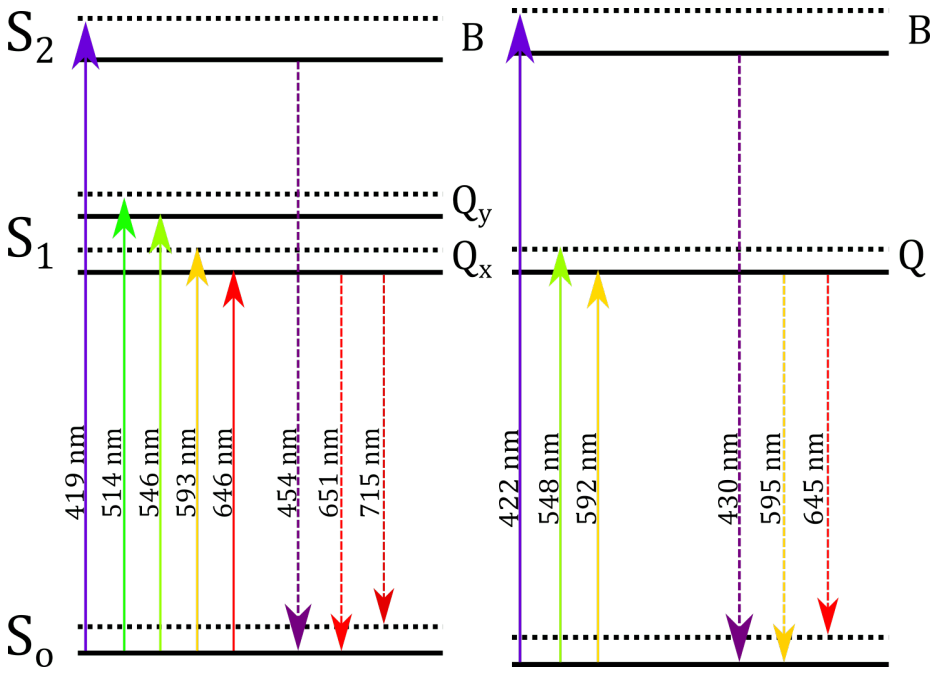

FIGURE 4.6: Schematic diagram showing the main radiative energy dissipative processes of TPP (left) and ZnTPP (right) in toluene. Absorption (solid vertical arrows) from the ground state to higher electronic (solid black) and vibrational (dashed black) states. Fluorescence (dashed vertical arrows) to the ground electronic state after excitation at $\lambda_{ex} = 400$ nm is included on the right of the diagram.

allows one to visualize the various energy dissipative pathways between vibrational levels and electronic states. For both TPP and ZnTPP porphyrins, the large absorption cross-section of the Soret peaks around 400 nm indicates a strong orbital overlap of the electronic and vibrational wavefunctions resulting in a high probability for $S_0 \rightarrow S_2$ transitions in the UV region. The first excited singlet states (Q-bands) reflect much weaker absorption cross-sections suggesting that the ground and singlet electronic and vibrational wavefunctions couple weakly.

4.2 Femtosecond Transient Absorption Spectroscopy

In this section, the femtosecond transient absorption data presented for the visible wavelength (450-700 nm) region was obtained on the home-built setup at the NLC. The transient absorption data for the near-IR region (900-1200 nm) was obtained at the University of Stellenbosch femtosecond-laboratory using a similar `Clark-MXR` laser source and optical layout as discussed in chapter (3). Since the measurements were conducted at different laboratories, slight differences in experimental parameters such as pump and probe fluency, instrument response function, and pulse chirp are unavoidable and careful attention to detail was given to match these parameters as best as possible. However, direct comparison of the near-IR and visible kinetic rates are expected to contain a small discrepancy.

Data Collection and Analysis

The measurements were repeated at least 3 times during the development and optimization of the pump-probe system, with reproducible results at varying levels of resolution, improving with each iteration. A large amount of time was required to optimize the pump-probe system by first identifying problems and applying appropriate fixes. For example, the active sample stage and off-axis mirrors were identified as solutions to photo-bleaching and cross-phase modulation (XPM) which caused artifacts in the data. Unfortunately, the laser system at the NLC was down for a few months and the final setup (figure 3.1) which included low GVD optics could not be tested.

Time-Resolved Kinetic Rate Analysis

A global kinetic analysis was performed on the visible and near-IR data separately, using `GloTaRan` time-resolved spectroscopic software. The visible and

near-IR spectral regions could not be analysed simultaneously for two main reasons. Firstly, because there was a 200 nm gap between the end of the visible and start of the NIR spectral windows; secondly, the instrument response function (i.e. dispersion curve) is different for the two experimental setups. If measurements from different spectral regions are to be analysed together they should be performed on the same setup. The kinetic models which converge with the fewest number of specified rates having the best overall fit and reduced error values were used for interpretation. During analysis of the near-IR region, there were cases where `GloTaRan` was not able to converge consistently and generated new rates each time an analysis was performed. For these cases, `Origin 9` was used to fit mono-exponential curves to specific wavelengths traces where charge-separation is known to occur. This provided a more accurate determination of the kinetic rates where `GloTaRan` could not be relied on.

Artifact

During the data analysis process, a strong spectral artifact around time-zero was observed. To determine whether the artifact was solvent or sample induced, a toluene only pump-probe measurement was performed (figure 4.7) and analysed. The artifact was identified to result from cross-phase modulation (XPM) and appeared as a predominantly positive W-shaped ΔA signal (figure 4.7) which obscured kinetics occurring at early times (0-2 ps) [51]. The artifact can be characterized in the spectral and temporal domains; in the spectral domain, a W-shaped Gaussian wavelet (FWHM = 15 nm) is seen progressing across the spectrum from shorter to longer wavelengths and decreases with intensity over time. In the time domain, the artifact also appears as a wavelet (FWHM = 0.5 ps) which progresses along the dispersion curve of the probe light. The severity of the artifact is correlated to: the amount of

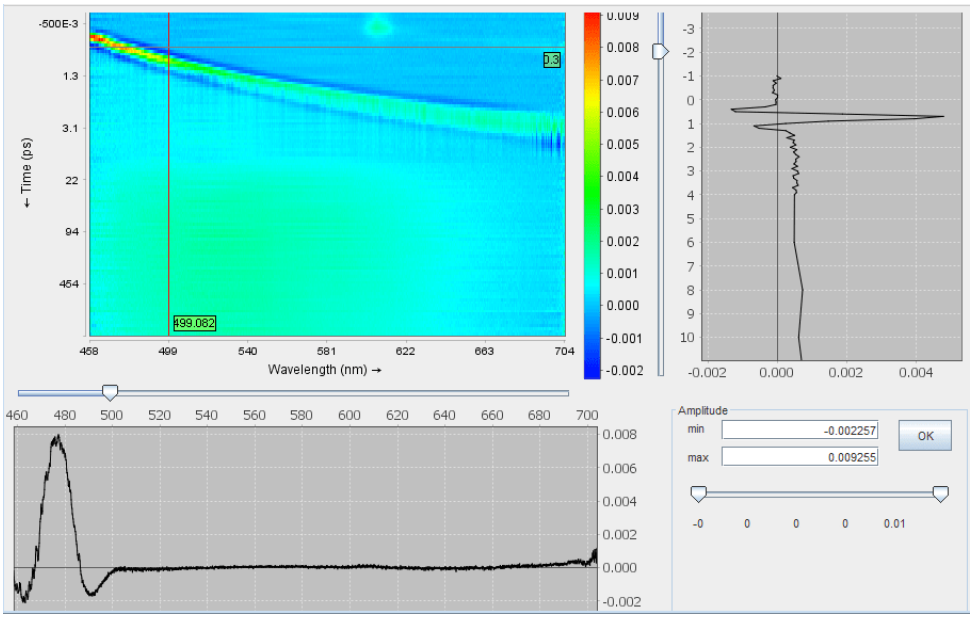

FIGURE 4.7: Time-resolved difference absorption spectrum of pure toluene solvent (top left), with corresponding spectra (bottom) and temporal (right) traces. Data graphically displayed using `GloTaRan`.

chirp in the supercontinuum probe, the difference in the refractive index between the quartz cuvette, and the polarity of the solvent in the cuvette [42]. Pump-probe measurements performed in non-polar solvents such as hexane showed little to no evidence of XPM even when the difference in refractive index was large ($n_{quartz} - n_{hexane} \sim 0.1$), suggesting that solvent polarity is the more critical factor in the cross-phase modulation phenomena (Chapter (3) - System Performance).

4.2.1 Fullerene

Upon photo-excitation of pristine C_{60} at 387.5 nm, the lower vibrational modes of the S_1^* electronic level are predominately populated by electrons from the ground-state S_0. The transient absorption data in figure (4.8) shows two broad absorption features: the first is between 475 nm and 575 nm, and the second from 650 nm extending past the 700 nm cut-off. The kinetic traces along the maximum of these two features (figure 4.9) shows direct evidence

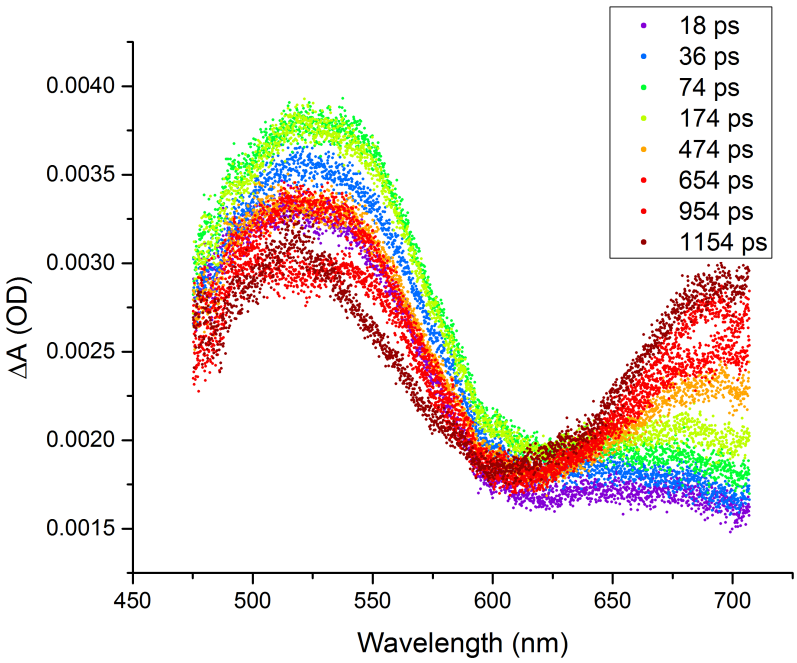

FIGURE 4.8: Visible transient absorption spectra of pristine C_{60} in toluene (5×10^{-5} M) excited at 387.5 nm with $\sim$4 μJ (1.02 mJ/cm^2) pulses at selected delay times.

of an energy dissipation process from one state, resulting in the formation of another state. The first positive ΔA signal at 520 nm is produced at time zero as a result of excited state absorption (ESA) from electronic level S_1 to higher electronic levels S_n [66]. Global analysis of the kinetic trace at 520 nm revealed a rise time of 27 ps, proceeded by a longer decay process with a life-time of 1296 ps (table 4.1). The 27 ps rise-time of the S_1 state is likely a result of vibrational relaxation from the initially populated vibrational modes S_1^*, down to the lowest vibrational mode of S_1. The S_1 state has two main decaying pathways: either non-radiatively through inter-system crossing (ISC) to the spin-forbidden triplet T_1 state, or a radiative decay directly to the ground state $S_1 \rightarrow S_0$. The S_1 and T_1 electronic levels of C_{60} have efficient spin-orbit coupling, thus favouring a non-radiative decay via ISC ($S_1 \rightarrow T_1$) versus non-radiative decay via internal conversion (IC) or direct fluorescence to the ground state ($S_1 \rightarrow S_0$) with quantum yields of $\phi_{ISC} = 0.96$, $\phi_{IC} = 0.39$ and

$\phi_f = 1 \times 10^{-4}$, respectively [67]. Ebbesen et al. [37] reported that the lifetime of the S_1 state is typically around 1.2 ns (table 4.1).

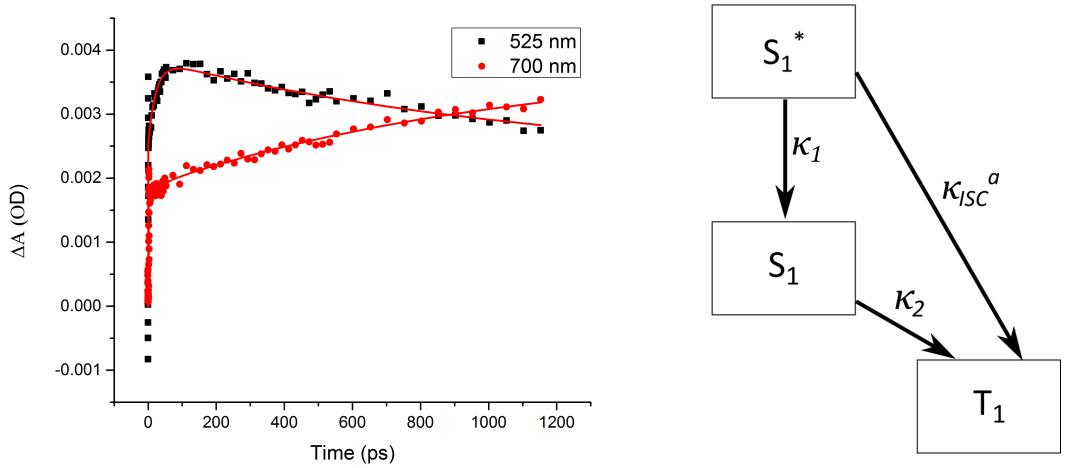

FIGURE 4.9: Difference absorption transients (left) at 520 nm (black squares, left), 700 nm (red dots) of pristine C_{60} in toluene (5×10^{-5} M) excited at 387.5 nm with corresponding kinetic model (right). Solid red lines (left) are the resulting fits to the experimental data obtained by performing a global kinetic analysis in `GLoTaRan`.

The second positive ΔA feature appearing around 700 nm is also attributed to an ESA process, this time, from the first excited triplet T_1 to the second excited triplet state T_2 [68]. The associated kinetic trace in figure (4.9) (red dots) shows a fast initial rise time of only 6.5 ps, suggesting that the T_1 state could have been populated directly from a higher vibrational mode ($S_1^* \rightarrow T_1$) during the fast relaxation after excitation, the details of which are still unrevealed in literature. After the fast initial population of T_1 a slower increasing component is observed lasting for 987 ps, which supports the hypothesis that ISC is likely involved. Due to the limited time window of the experiment (1.3 ns), the decay of the triplet state T_1 could not be measured. In literature, T_1 is known to have a long lifetime, between 40 and 280 μs, and decays radiatively via phosphorescence from T_1 to S_0 [60, 67]. The sharp spike in the ΔA kinetic data of figure (4.9) (left) at $t \sim 0$ is due to the XPM artifact and can be ignored.

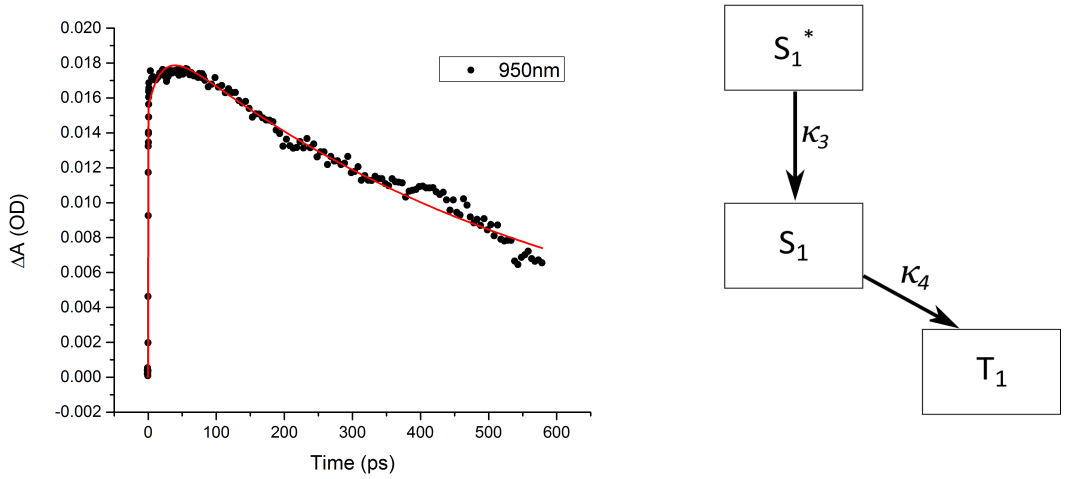

FIGURE 4.10: Difference absorption transients (left) at 950 nm (black dots) of pristine C_{60} in toluene (5×10^{-5} M) excited at 387.5 nm with corresponding kinetic model (right). Solid red line is the resulting fit to the experimental data obtained by performing a global kinetic analysis in `GLoTaRan`.

In the near-IR region (900 - 1300 nm), a broad positive signal appeared between 900-1100 nm and can be explained by a combination of two processes. The first process appears as a broad positive signal centred at 950 nm and is attributed to an ESA transition from the first excited state S_1 to the second excited state S_2 [68]. In figure (4.10) (right), the kinetic rates indicate a rise time of 21 ps followed by a mono-exponential decay lasting 898 ps. The second process is assigned to a $C_{60}^{-\bullet}$ product absorption signal centred around 1000 nm (table 4.1). Ideally, pristine C_{60} should not exhibit this electron decay channel, however; in most cases, C_{60} unavoidably accumulates a free electron from the environment due to an oxygen diatom bonding to C_{60} to form C_{60} oxide [69, 70]. This extra electron does not affect the formation or photophysical properties of the self-assembled complex and can be safely ignored in the subsequent analysis.

A kinetic model for pristine C_{60} (figure 4.11) can be constructed using the kinetic results obtained from the near-IR and visible transient absorption data (figures 4.9 and 4.10), respectively. Of particular interest, is the difference in

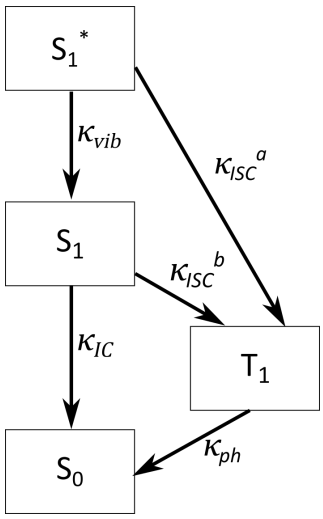

FIGURE 4.11: Pristine C_{60} kinetic model.

	Rate (s^{-1})	Time (ps)
κ_1	3.7×10^{10}	27
κ_2	7.7×10^{8}	1296
κ_3	4.0×10^{10}	21
κ_4	1.1×10^{9}	898
κ_T	1.0×10^{9}	987
κ_{vib}	4.2×10^{10}	24
κ_{ISC^a}	1.5×10^{11}	6
κ_{ISC^b}	9.1×10^{8}	1097
$\kappa_{IC}*$	8.3×10^{8}	1200
$\kappa_{ph}*$	2.5×10^{4}	4×10^{7}

TABLE 4.1: Pristine C_{60} kinetic rates.

the S_1 population times of 27 ps ($3.7\times10^{10}\ s^{-1}$) and 21 ps ($4.0\times10^{10}s^{-1}$), obtained from the 530 nm and 950 nm traces, respectively. Similarly, the decay rates of S_1 via ISC to T_1 varied with times of 1296 ps ($7.7\times10^{8}\ s^{-1}$) and 898 ps ($1.1\times10^{9}\ s^{-1}$), respectively. The slight discrepancy between these rates is likely due to differences in the two pump-probe experimental setups, as well as variations in the quality of the mixed samples at the time of the experiment. Because both the visible and near-IR kinetic models describe the population and decay of the same S_1 level, the kinetic rates of κ_{vib} and κ^b_{ISC} in the final model (figure 4.11) are calculated as the average so that, $\kappa_{vib} = \frac{\kappa_1+\kappa_3}{2}$ and $\kappa^b_{ISC} = \frac{\kappa_2+\kappa_4}{2}$. The final model then shows that upon initial excitation of S^*_1, vibrational relaxation occurred to the lowest vibrational mode of S_1 after 24 ps ($4.2\times10^{10}\ s^{-1}$), followed by ISC to the triplet lasting 1097 ps ($9.1\times10^{8}\ s^{-1}$). For completeness, the main $S_1 \rightarrow S_0$ decay via non-radiative IC ($\kappa_{IC}*$), and $T_1 \rightarrow S_0$ phosphorescence ($k_{ph}*$) kinetic rates of pristine C_{60}, obtained from Ebbesen et al. [37], are included in table (4.1) and in the final model (figure 4.11). The rate constant κ_T represents the rate of triplet state formation.

4.2.2 Tetraphenylporphyrin

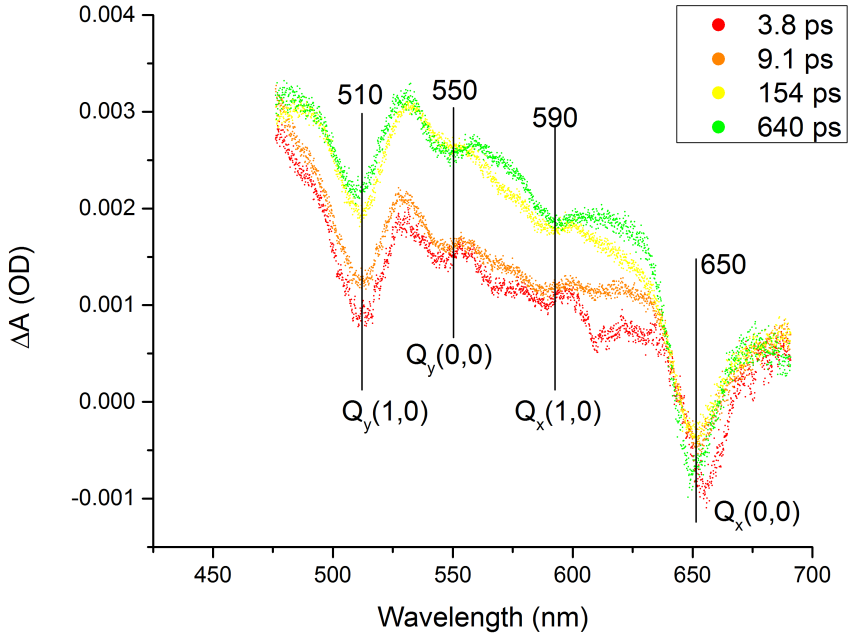

FIGURE 4.12: Difference absorption spectrum of TPP (2×10^{-6} M) in toluene excited at 387.5 nm with $\sim$4 μJ (1.02 mJ/cm^2) pulses at selected delay times. The spectral position of the Q_x and Q_y bands have been labelled (in nm).

The S_2 electronic state of TPP is directly populated by a photo-excitation at 387.5 nm and rapidly decays into S_1. The TAS measurements performed on pure TPP in toluene (figure 4.12) showed a broad positive signal between 475 - 625 nm and only appeared at delay times $t > 9$ ps. It is possible that this broad ΔA signal represents an ESA transition from S_1 to higher states S_n. A global kinetic analysis performed with `GloTaRan` on the visible region data (figure 4.12) yielded a single fast component lasting 20 ps which reflected the population time of S_1 via non-radiative IC from S_2 to S_1, as well as a very long-lived decaying component of 34 ns, which exceeded the window of the experiment, and represents the lifetime of the S_1 level. Other interesting features are two sharp depleted signals at 510 nm and 650 nm that align well with the $Q_y(1,0)$ and $Q_x(0,0)$ bands, as well as two smaller depleted

signals aligning with the $Q_y(0,0)$ and $Q_x(1,0)$ bands of TPP, respectively. These signals depict ground-state bleach (GSB) and stimulated emission (SE) processes occurring between the S_1 and S_0 electronic states. The depleted regions remained almost constant during the experiment, suggesting that S_1 is stable and remained populated for a long time (∼ns). This result corresponds well with literature, that porphyrin does not favour the production of bottleneck states and has a long-lived singlet state [60]. The near-IR region (figure 4.22) did not produce any clear signals during the time window of the experiment. Upon close inspection, there is a slight rise in the ΔA signal over time at around 1100 nm. Positive signals this far into the near-IR are usually caused by triplet-triplet excited state absorption processes. TPP is known to have a triplet state which forms, but due to the slow decay of the singlet and the short window of the experiment, there was not sufficient data determine the kinetic rate of the triplet state. Literature suggests that ISC occurs from $Q_x \rightarrow T_1$ within ~ 12 ns [60].

4.2.3 Fullerene - Tetraphenylporphyrin Complex

According to the optical density values of the ground-state absorption spectra for TPP-C_{60} (figure 4.2), the pump excitation wavelength of the experiment (λ_{ex} = 387.5 nm) does not overlap well with any absorption peaks of TPP. The total optical density of the TPP-C_{60} complex at 387.5 nm is 0.39, of which TPP contributes only 19%, implying that the majority (81%) of incident pump energy excited the C_{60} moiety. If a photon is absorbed by the C_{60} moiety and not TPP, then no charge-separation (CS) can occur because TPP is not an electron acceptor. If both TPP and C_{60} are excited simultaneously, charge-separation can still occur because C_{60} can reversibly accept up to 6 electrons. All of these excitation scenarios will occur simultaneously,

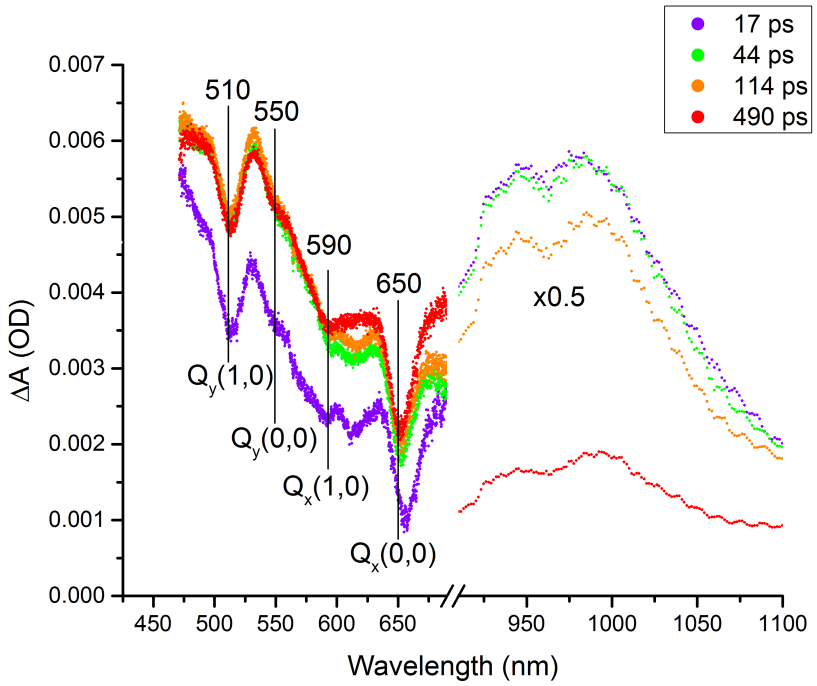

FIGURE 4.13: Difference absorption spectra of TPP-C_{60} supramolecular complex in toluene excited at 387.5 nm with $\sim$4 μJ (1.02 mJ/cm^2) pulses at selected delays. The near-IR data region has been scaled by a factor of 0.5 for visual representation.The spectral position of the Q_x and Q_y bands have been labelled (in nm).

therefore, the TAS data will contain a convolution of spectra belonging to different energy dissipative processes unique to TPP, C_{60}, and TPP-C_{60}. In the visible region of figure (4.13), upon photo-excitation at 387.5 nm, multiple peaks appear between 500-650 nm where GSB, SE and ESA of the Q-bands occur (figure 4.12). This observation shows that, in some cases, an excited electron in TPP relaxed down to the S_1 state without undergoing rapid electron transfer to C_{60}. Comparing this spectral data to that of pristine C_{60} (figure 4.8), similar broad ESA features are seen at 500 - 600 nm and 650- >700 nm, respectively, indicating that C_{60} underwent ISC from $S_1 \rightarrow T_1$. Moving towards the near-IR region, a broad positive signal between 900 - 1100 nm indicates product absorption of $C_{60}^{-\bullet}$ anion [32]. This broad signal is a characteristic indicator that charge-transfer has occurred from TPP to the C_{60} cage.

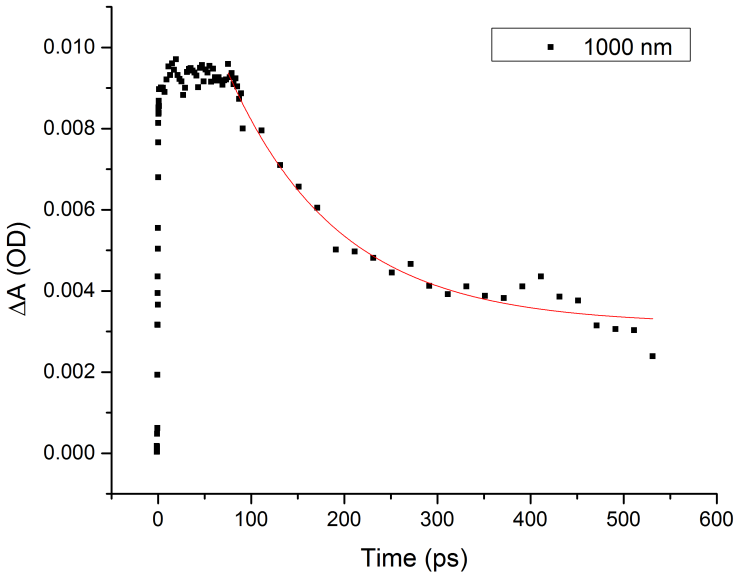

FIGURE 4.14: Difference absorption transients at 1000 nm of TPP-C_{60} in toluene excited at 387.5 nm. The solid red line represents a mono-exponential fit (χ^2= 1.28×10^{-7} and R^2 = 0.9774) to the raw experimental data (black squares) using an `Origin 9.0` exponential fitting algorithm.

A global analysis of the data using `GloTaRan` software showed that charge-separation (CS) occurred rapidly within 1.2 ps to produce the [$TPP^{+\bullet}$-$C_{60}^{-\bullet}$] radical ion pair (RIP); however, after numerous attempts `GloTaRan` was not able to reproducibly and accurately fit the decay component of the 1000 nm band. One explanation is that within the sample solution there are still a small fraction of C_{60} oxide molecules that did not bind to TPP, thus, producing an overlapping $C_{60}^{-\bullet}$ decay signal from two different systems. The decay

	Rate (s^{-1})	Time (ps)
κ_{CS}	8.3×10^{11}	1.2
κ_{CR}	8.4×10^{9}	119

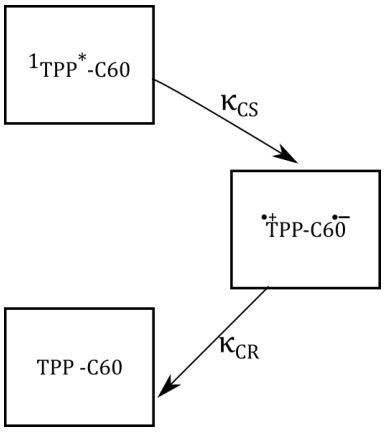

FIGURE 4.15: Charge-transfer kinetic rates (left) of TPP-C_{60} in toluene with corresponding model (right).

or charge-recombination (CR) rate was then determined in `Origin 9.0` by fitting a decaying mono-exponential function to the 1000 nm trace (figure 4.14) yielding a CR decay time of 119 ps (8.4×10^9 s^{-1}) (figure 4.15).

4.2.4 Zinc Tetraphenylporphyrin

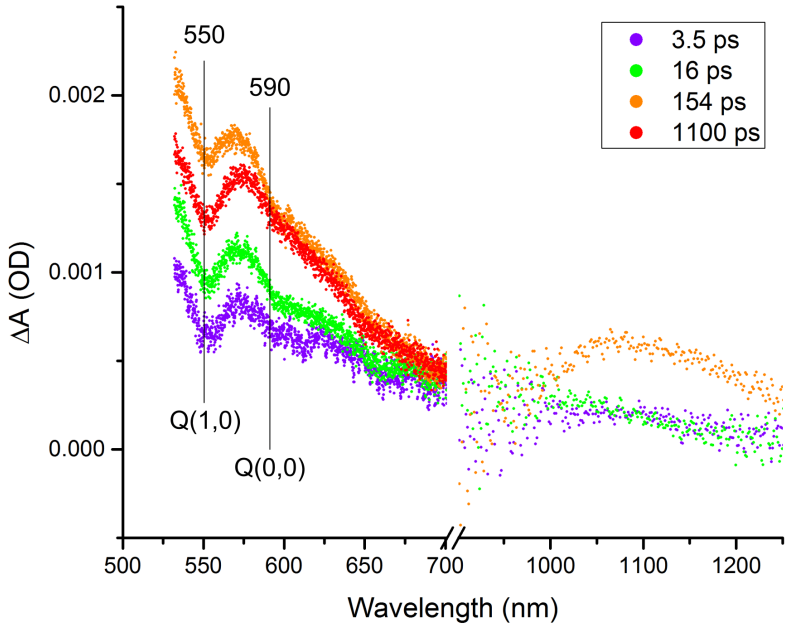

FIGURE 4.16: Difference absorption spectra of ZnTPP (2×10^{-6} M) in toluene excited at 387.5 nm with ~4 μJ (1.02 mJ/cm^2) pulses at selected delays. The location of the Q-bands have also been indicated (in nm).

Upon excitation at 387.5 nm, the S_2 state of ZnTPP is directly populated before decaying rapidly into S_1. TAS data of pure ZnTPP (figure 4.16) in toluene revealed detailed absorption features in the visible region between 525 - 600 nm, where the Q-bands absorb (figure 4.4), and a broad positive signal between 525-650 nm which is likely caused by ESA from S_1 to higher states S_n. A negative depleted signal is seen at 550 nm and aligns well with the $Q(1,0)$ transition (figure 4.6), indicating that GSB and SE occur between the first vibrational mode of S_1 and the lowest vibrational mode in the ground state S_0.

A small dip in the spectra at 590 nm aligns well with the $Q(0,0)$ transition, suggesting that much weaker GSB and SE process occur between the lowest vibrational modes of the S_1 and S_0 electronic states, respectively. The consistency of these GSB and SE signals for all delay times confirms that the S_1 state in ZnTPP is stable and long-lived. Global analysis of the data showed that the broad ESA signal (<500 - 600 nm) showed the singlet state S_1 decayed with a lifetime of 2.4 ns, in good agreement with literature [64]. During relaxation, it is expected that some of the excited S_n electrons in ZnTPP will undergo ISC to form the triplet state [64]. For the near-IR region, a weak, broad, positive absorption signal appeared at later times ($\sim$150 ps) and could have been caused by ESA between the first triplet state T_1 and higher triplet states T_n.

4.2.5 Fullerene - Zinc Tetraphenylporphyrin

For the ZnTPP-C_{60} supramolecular complex, the visible region of the difference absorption graph (figure 4.17) showed strong evidence of features that resemble the $S_1 \rightarrow T_1$ ISC processes which occurs upon photo-excitation of pristine C_{60} (figure 4.18). Absorption of the Q-bands in ZnTPP is revealed by two small shoulders in the spectra at 550 nm and 590 nm, in alignment with the $Q(1,0)$ and $Q(0,0)$ transitions. Analysis of the ZnTPP-C_{60} absorption spectra (figure 4.4) shows that the ZnTPP moiety contributes to only $\sim$4.5% of the total optical density at the excitation wavelength, with the remaining $\sim$95.5% being absorbed by C_{60}. The visible region of the ZnTPP-C_{60} transient data reflected the individual transient signals of pristine C_{60} (figure 4.8) and ZnTPP (figure 4.16) with no additional spectroscopic features which could be related to electron-transfer processes. In the near-IR region, the characteristic $C_{60}^{-\bullet}$ signal is observed. A broad peak between 900-1050 nm clearly indicates that an electron was transferred from ZnTPP to C_{60} resulting in a charge-separated state. Kinetic analysis along the peak at 1000 nm shows

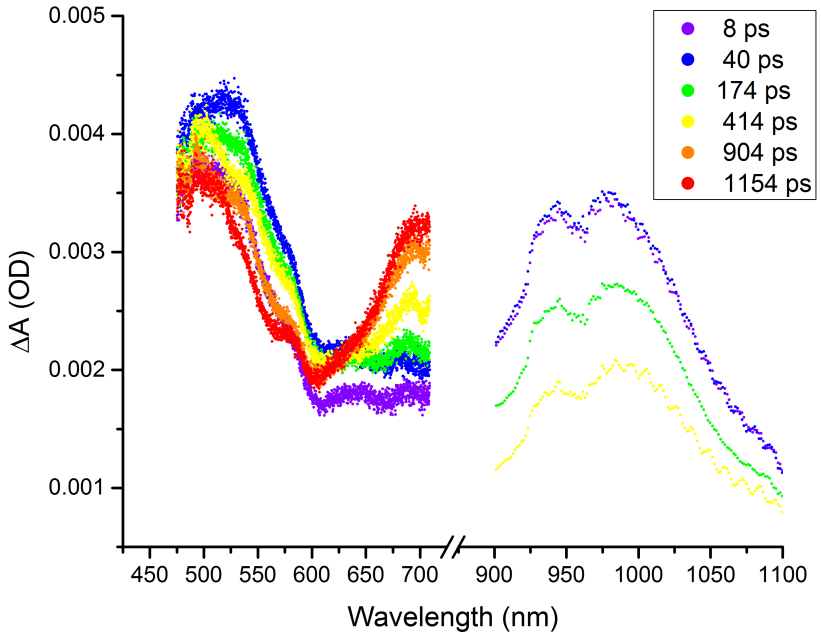

FIGURE 4.17: Difference absorption spectra of ZnTPP-C_{60} supramolecular complex in toluene excited at 387.5 nm with ~4 μJ (1.02 mJ/cm^2) pulses at selected delays. The locations of the Q-bands have also been drawn. The near-IR data region has been scaled by a factor of 0.6 for visual representation.

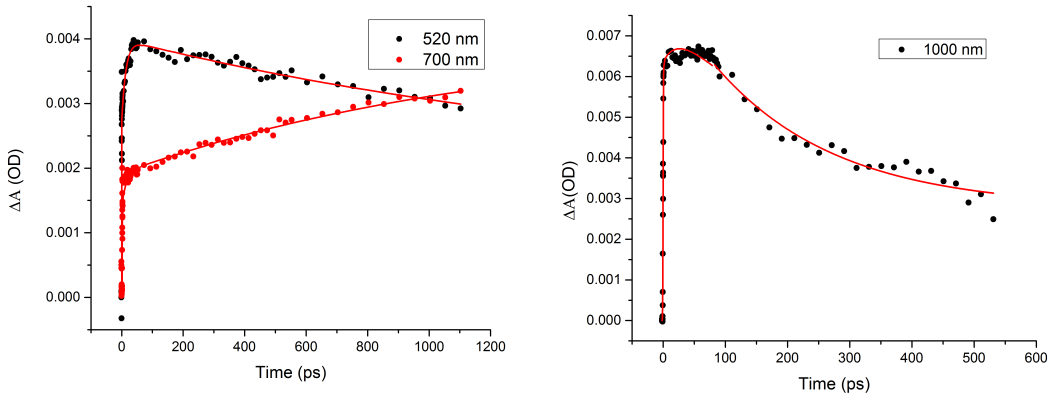

FIGURE 4.18: Difference absorption transients taken at 520, 700 nm (left) and 1000 nm (right) of ZnTPP-C_{60} complex in toluene excited at 387.5 nm. The solid red line (right) represents a mono-exponential fit (χ^2=4.9×10^{-8} and R^2 = 0.9681) to the raw experimental data (black dots) using an `Origin 9.0` exponential fitting algorithm. Solid red lines (left) are the resulting fits to the experimental data obtained by performing a global kinetic analysis in `GLoTaRan`.

the time of CS to be 1.8 ps followed by a much slower CR rate of 183 ps (figure 4.18). The CR rate was obtained using `Orgin 9.0` exponential fitting

	Rate (s^{-1})	Time (ps)
κ_{CS}	5.5×10^{11}	1.8
κ_{CR}	5.4×10^{9}	183

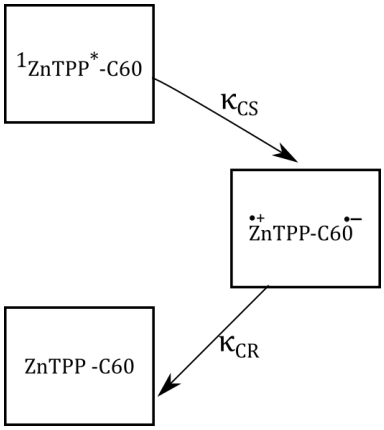

FIGURE 4.19: Charge-transfer kinetic rates (left) of ZnTPP-C_{60} in toluene with corresponding model (right).

algorithms which converged in less than 10 iterations indicating that the fits were of good quality, whereas the CS rate was extracted from the `GloTaRan` global kinetic model. Electron transfer occurred directly from the excited singlet state of ZnTPP (HOMO) to the cage of the fullerene (LUMO) before it recombined (figure 4.19).

Discussion

In the reviewed literature, most of the transient absorption spectroscopy experiments performed on these supramolecular complexes or similar dyad complexes were excited using frequency doubled fundamental pulses fixed at 400 nm or at longer wavelengths closer to the Q-band region of porphyrin around 550 nm, with varying pulse time durations (ns-fs) and detectable resolutions. There is no currently available literature which can be used as a reference to compare the obtained electron-transfer kinetic rates. The closest direct comparison can be made to fullerene-porphyrin supramolecular dyads which are covalently linked and have the same constituents but lack the non-covalent and close contact bonding arrangement which will alter the rates

significantly. The inclusion of important photophysical data such as ground-state absorption, steady-state fluorescence, and resulting Jablonski diagrams provided for the first time, a complete spectral characterization which served as valuable supporting information for analysing the results obtained from the femtosecond transient absorption experiment.

The charge-separation (k_{CS}) and charge-recombination (k_{CR}) rates were calculable from the product absorption radical-anion decay signal appearing around 1000 nm because it was spectroscopically isolated from the other excited state features, such as $S_1 \rightarrow T_1$ ISC of C_{60}, as well as GSB, SE and ESA of the porphyrins. Since the direct comparison of the individual kinetic rates (k_{CS} and k_{CR}) to literature is not possible, the ratio of $I = k_{CS}/k_{CR}$ (unit-less quantity) is used to describe the charge-separation efficiency of a donor-acceptor system, which can then be compared directly to other types of systems. Values of $I > 1$ indicate a long-lived recombination process, whereas values of $I < 1$ indicate that recombination occurs faster than separation, a result that is less than desirable for solar cell applications. Recently, charge-separation and recombination kinetic rates of ZnTPP-C_{60} supramolecular dyads were published by Das et al. [71] and reported an efficiency value of $I = 24$, i.e. electron recombination occurred 24 times slower than electron separation. For the TPP-C_{60} complex, results published by El-Khouly et al. [72] reported ET efficiency values of $I = 0.01$, however, the k_{CS} and k_{CR} kinetic rates in this article described electron-transfer from the triplet state of TPP to C_{60} and not from the singlet state, and thus has no comparative value. Since both TPP and ZnTPP porphyrins have similar excited state properties and electronic features, one can assume that the value I for TPP-C_{60} should be similar in magnitude to the value obtained for ZnTPP-C_{60} ($I = 24$) [71].

4.3 Additional Figures

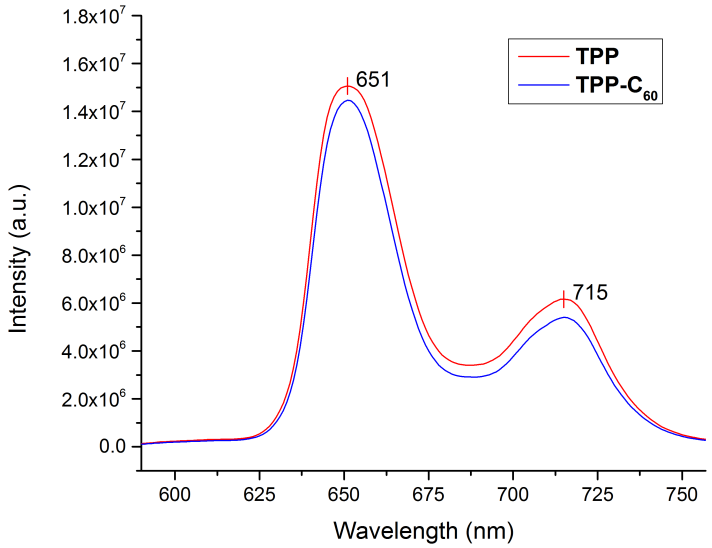

FIGURE 4.20: Fluorescence emission spectra of TPP (red) and TPP-C_{60} (blue) in toluene excited at λ_{ex} = 400 nm with optical density values of 0.21 and 0.38, respectively. Concentrations of TPP and C_{60} were $\sim 2 \times 10^{-6}$M and $\sim 5 \times 10^{-5}$M, respectively, in a 10 mm quartz cell.

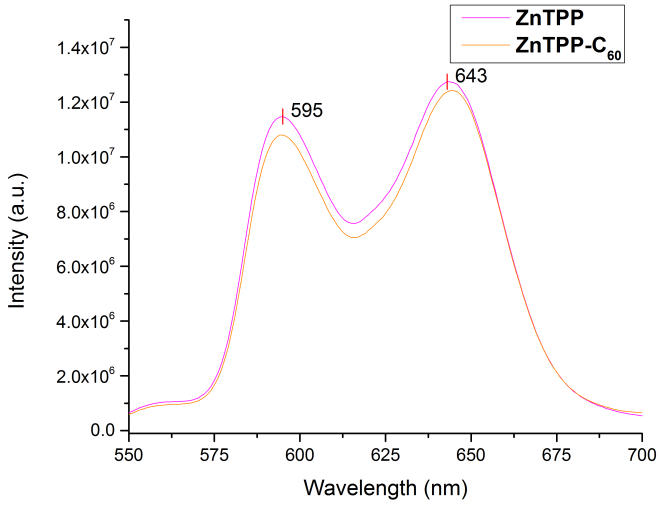

FIGURE 4.21: Fluorescence emission spectra of ZnTPP (magenta) and ZnTPP-C_{60} (orange) in toluene excited at λ_{ex} = 400 nm with optical density values of 0.06 and 0.23, respectively. Concentrations of ZnTPP and C_{60} were $\sim 2 \times 10^{-6}$M and $\sim 5 \times 10^{-5}$M, respectively, in a 10 mm quartz cell.

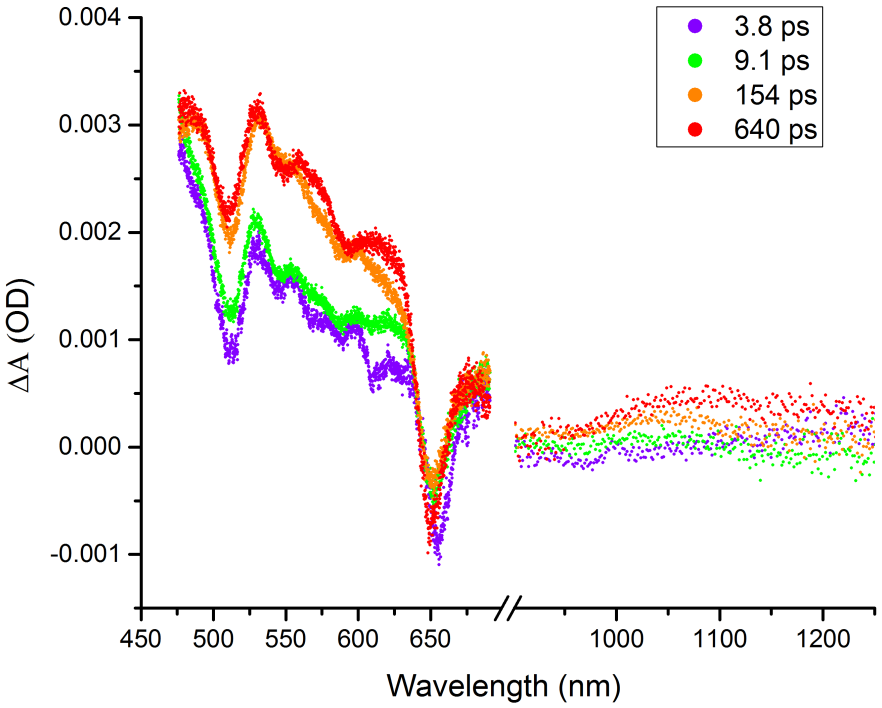

FIGURE 4.22: Difference absorption spectra of TPP (2×10^{-6} M) in toluene excited at 387.5 nm with ~4 μJ (1.02 mJ/cm^2) pulses at selected delay times.

Chapter 5

Conclusion

To conclude, before the femtosecond transient absorption spectroscopy experiments could be performed on the donor-acceptor complexes, a completely new system had to be developed in order to achieve the required optical density resolution ($< 1\times10^{-3}$). The new Pump-Probe system included sensitive CMOS photo-diode array detectors, delay-line controllers, pulse synchronizers, an optimized supercontinuum generation setup accompanied by low GVD optics, just to mention a few. All of the hardware components had to be programmed using `MATLAB` into a functional graphical user-interface that offers full control over the equipment and experiment. The completed system was successfully used to perform pump-probe spectroscopy on TPP-C_{60} and ZnTPP-C_{60} complexes at an optical density resolution of $\sim1\times10^{-4}$ OD, two orders of magnitude improvement over the old system.

For both the TPP-C_{60} and ZnTPP-C_{60} supramolecular assemblies, charge-separated states were successfully characterized under experimental conditions where the donor moiety was only marginally excited by the excitation pulse. The 775 nm fundamental output frequency of the laser fixed the excitation pulse to 387.5 nm (SHG) which is $\pm$32.5 nm below the main Soret peak of porphyrin S_2, which caused the resulting TAS data to contain a convolution of processes not related only to electron transfer processes, but also,

includes processes of the excited acceptor. Increasing the wavelength of the pump beam from 387.5 nm to longer wavelengths has a direct impact on the fraction of absorption cross-section shared between the porphyrins and C_{60} considerably. For example, in the case of ZnTPP-C_{60}, the absorption cross-section of the porphyrin ZnTPP increases from 4.5% at 387.5 nm to 27% at 400 nm, with maximum absorption of 95% occurring at the Soret band (420 nm). The remainder of the pump excitation is absorbed by C_{60} and thus does not contribute to charge-transfer processes. It is then worthwhile exploring the use of wavelength tunable systems such as a non-linear optical parametric amplification device, which allows one to generate almost any excitation wavelength in the visible to near-IR regions.

Finally, the TPP-C_{60} and ZnTPP-C_{60} complexes were measured to have charge separation rates of κ_{CS}=8.3$\times 10^{11}$ s^{-1} (1.2 ps) and κ_{CS}= 5.5$\times 10^{11}$ s^{-1} (1.8 ps), and recombination rates of κ_{CR}= 8.4$\times 10^{9}$ s^{-1} (119 ps) and κ_{CR}= 5.4$\times 10^{9}$ s^{-1} (183 ps), respectively. The electron-transfer kinetics equate to efficiency values of $I = 100$ and $I = 102$ for the TPP-C_{60} and ZnTPP-C_{60}, respectively, and shows that the efficiency I of electron-transfer in the ZnTPP-C_{60} supramolecular complex was extended by %400 when compared to a similar supramolecular dyad [71]. Comparing the metal and non-metal porphyrin-C_{60} complexes show that the free-base donor underwent fast separation and recombination, whereas its metal counterpart prolonged both separation and recombination processes. Ultimately, the TPP-C_{60} and ZnTPP-C_{60} complexes obtained similar and remarkably high efficiencies considering the compact nature of the system. These results show that these simple, self-assembled, non-covalently interacting porphyrin-fullerene complexes remain promising candidates for use as organic semiconductor materials in solar cell applications.

Future work

Soon after femtosecond lasers first appeared, ultrafast pulsed experiments such as pump-probe spectroscopy began incorporating pulse shaping devices such as a liquid crystal spatial light modulators [73] which are capable of performing precise phase and/or amplitude alterations to the excitation pulses. By incorporating a closed-loop feedback into the pump-probe experiment, a genetic learning algorithm is used to control the pulse shaping device so that after many generations (experiments) each iteration evolves from the previous in a "survival of the fittest" type strategy so that eventually, the algorithm arrives at the optimal pulse shape which optimized a specific energetic process. A benefit of the genetic algorithm is that it does not require any knowledge of the system and only measures the spectroscopic outcome of a particular pulse shape. Pulse shapes which have a desirable spectroscopic effect are favoured over those which have a negative spectroscopic outcome. The genetic selection parameters include the possibility for random mutations to take place which improves the accuracy of the algorithm greatly and avoids situations where only a local minimum is reached. For the pump-probe results presented in this dissertation, the excitation pulse had a sech^2 shape which provided a single instantaneous excitation event. Pump-probe spectroscopy experiments performed on porphyrin-fullerene supramolecular complexes using modified pulse shapes in a genetic algorithm have never been performed before and will shed new light on the nature and mechanism of the electron-transfer process occurring in these systems.

Appendix A

Standard Operating Procedures

This appendix is written in a user manual style and is intended to guide a new student through the normal laser operational procedures and MATLAB UI while providing useful information.

A.1 Getting started

The procedure is written in order of execution. Start at section 1. and work the way down the checklist carefully. Failure to do so will result in serious damage to the laser system and equipment! Always use appropriate safety gear and behave in a responsible way to avoid any accidents which could result in serious harm to the user and the laser source.

A.1.1 Switching on the laser

Step 1. Switch on the chiller for the large power supply. This chiller is located outside the main building on the 2_{nd} floor (outside the user facilities centre). Press the power button once and return to the femtosecond laboratory. The chiller water levels should be checked once a month

and topped up with distilled water only. Normal operating temperature is between 18 - 19 C°.

There are two ways to switch on the laser, either automatically (Step 2) or manually (Step 3 A-E). When the system is working well, then the automatic method is recommended. If the laser is not performing properly, then the manual method is recommended.

Automatically-Step 2. Once the chiller has been switched on, return to the CPA DT506 laser control box, turn the key into the "ON" position then navigate to the `Master tab` and press the `Start` button. Wait 1 - 2 hours for the system to warm-up, then press the `open shutter` button to allow the beam to exit the laser source.

Manually-Step 3 A. On the CPA DT506 laser control box, turn the key into the "ON" position. Navigate to the `Amplifier tab`, press the `Turn on HV power` button to activate the pockel cells (normal voltage values are HV1 = 3.33 KV and HV2 = 3.10 KV).

Manually-Step 3 B. Then, navigate to the `Pump Laser tab` and press `Turn On Main power`. After a few seconds the `Pump Start` button will become available, press the `Pump Start` button. After a few seconds the `Lamp On` button will become available, then press the `Lamp On` button and wait for 15 - 20 minutes.

Manually-Step 3 C. Press the `lamp current` setting button and set the current to a value between 20 - 21 Ampere. NB! Make sure that the `Feedback` button is OFF during start-up (feedback control automatically adjusts the current setting to maintain a constant power output and is set under the `Pump Power` setting button). If you can not access the `lamp current` or `Pump Power` setting buttons then navigate to the `Master tab` and press `Power Login` and enter the password (1234).

Manually-Step 3 D. Press the `Lamp Start` button. If the error "verify that oscillator is mode-locked" appears, quickly navigate to the `Oscillator` tab and press the "Verify that oscillator is mode-locked" button at the bottom of the screen and then return to the `Pump Laser` tab and clear the error message. If the current and power values display 0.000 then press `Turn Off Main Power` and start over at step 3-A. If the current and power values display correctly and no error messages appear the `Open ORC` and `Open injection` buttons will become available.

Manually-Step 3 E. Press `Open ORC` button followed by the `Open injection` button and wait for the system to warm-up (approx. 1-2 hours).

Step 4. Power on the oscilloscope located next to the CPA laser control box. Once the scope has turned on you should see a weak build-up trace on the oscilloscope. The recommended oscilloscope settings are as follows; time scale = 20 ns, termination resistance = 50 Ohms, voltage scale = 100 mV, bandwidth = 2.5GHz/s.

Step 5. Once the laser has warmed up, press the `Open Output` button and place a power meter at the output of the laser and make slight adjustments to the `Current settings` values until output power is suitable.

A.1.2 Connecting the instruments

This is typically done during the warm-up period.

Step 1. Switch on the PC located next to the measurement box and log in as a user (password: pumpprobe or justin).

Step 2. Switch on the plug connected to the delay-line power supply. You should see a green LED inside the power supply cage to indicate that it is on.

Step 3. On the USB hub, power on the devices you will need. If you are doing single channel (no reference beam) then you must power on; Cam1, PD and Delay-line. If are doing double channel measurements then you must power on; Cam1, Cam2 and PD. The camera(s) and PD device will show a green LED indicating they have been powered on successfully. If any of these devices are flashing or showing a red/amber colour then please go to the connected devices troubleshooting page.

Step 4. Power on the Thor Labs optical chopper, located on the upper section of the optical table. Press the power button once and then press the turning knob inward to select run. The chopper should now start rotating and the display should read Target: 500Hz -Locked. If there is an issue with this step please see the troubleshooting page.

Step 5. Power on the Thor Labs fast optical shutter that is mounted to the blue frame near the experimental box (a small red unit). A green LED will indicate the on/off status of the device. Press enable to open/close the shutter. This is used to block or transmit the pump-pulse into the experiment box.

A.1.3 Launching the UI on the PC

Only possibly after connecting and powering on the relevant components.

Step 1. On the PC desktop double-click on the MATLAB icon and wait for the terminal to appear.

Step 2. In the MATLAB terminal type; “uiV2” (User Interface Version 2.0), press enter and wait a few seconds for the UI to initialize the system and open.

Step 3. The GUI should now be visible and ready to use.

A.2 Pump-Probe UI

The graphic user interface (GUI) was developed with the sole intention of collecting high-resolution transient absorption data of various samples. Please read this section carefully in order to use the GUI correctly.

Troubleshooting

Due to the complex nature of the experiment, it is unavoidable that errors and crashes can occur which may result in permanent loss of data. `MATLAB` has the tendency to freeze or crash unexpectedly when this happens. In such a case, `MATLAB` should be closed completely and each USB device switched-off from the main hub, before systematically powering-up each USB device and reopening `MATLAB`.

A.2.1 Data Acquisition panel

This panel is used mainly for calibrating the system prior to performing any measurements. There are 4 buttons (3 checkboxes and a settings menu) which can be accessed from this panel.

Settings menu.

The settings menu has 7 input variables which are necessary to initialize the camera(s).

- Set central wavelength [400-600nm]
- Number of Scans [1-100000]
- Integration Time [1-100 us]
- Trigger Delay [ms]
- Pixel Bin (1,2,4)
- clock speed- full(0) half(1)

- Single or Double cam [s,d]
- Samples to Average

Once you are satisfied with the parameters press okay to initialize and continue.

Raw data check-box. The raw data check box is used to calibrate the white-light super-continuum before running a measurement. The success of a measurement depends highly on the quality of the white-light being used, so it is highly recommended that you make use of this function regularly before each measurement is performed. When using the raw data mode it is recommended that you use a low scan count (500-2000 scans) so that the plot updates frequently and any instability in the white-light can be noticed easily. An unstable white-light will result in a rapidly fluctuating intensity spectrum in the plot. If you use a fluctuating white-light continuum for a pump-probe experiment the data will be noisy and the SNR ratio will be very poor. Pressing the big red STOP button will break the data acquisition loop.

Diff. Absorption and cycle. If the Diff. Absorption button is checked the system will perform a single difference absorption measurement (-log10(PumpOn/PumpOff)) and plot the result in the plot window. If you want to plot the diff absorption data in a continuous loop the cycle check-box must be ticked. The plots will then be displayed simultaneously and only the Nth most recent plots will be displayed, you can change the number of plots to be displayed in the plot settings menu (default is N = 5 plots).

STOP and data plotter. Any measurement can be interrupted by pressing the STOP button. When you perform a measurement you will see, in the small panel called status, the colour of the indicator will turn red

and the text will say busy. This indicated that the system is busy performing the desired measurement and the plot window should show some results after a short time. When the stop button is pressed the loop will be terminated and the status box will return to green and the text will display ready indicating that the system is ready for the next operation. If you would like to plot and view previously recorded data that is saved onto the PC, you can press the plot data button and select the file you would like to view. Note that the graph has been made to hold all the plotted data until the user clears the figure by pressing the clear figure button. The save data button can be used to save any diff absorption data which is currently (most recent) plotted on the figure. Note that if you enable the cycle function then you must first press stop and then save data, at which point you will be prompted to enter a filename for the data to be saved as.

Pump-Probe experiment panel.

Time Span - When conducting a pump-probe experiment you need to set the time intervals at which you want to measure, to do this you first press the new span button which opens a menu where you can insert the desired time steps. The first column is for the "start time [ps]", second is for the "step size [ps]" and the third is for the "stop time [ps]" where each row indicates a new span. It is very important that you overlap the stop/start times when you move to a new span row. If you do not then you will have gaps in the time intervals. Once you are satisfied with the selection you then press save and enter a filename, the filename you choose now will also become the filename for your final pump-probe data, which is saved to the Data folder on the desktop in the Pump-Probe folder, so pick the name carefully.

Delay line - Please read the SOP for the delay line before using this button. Time zero should already be set.

Set Parameters - The function of this button is the same as the settings button in the data acquisition tab and is used to initialize the camera with various parameters for the pump-probe measurement. You will also be asked to enter the filename for the span set you want to use, here you should enter the filename which you saved your specific span set as in section 3.1). Start/Pause measurement - Once you have accepted and initialized the camera to the correct parameters for your experiment you can press the Start button. At this point you will see the status panel turn blue with text Delay indicating that the delay line is now active, this will then turn red once the delay has stopped and a measurement is in progress. This will happen each time the delay line moves into the next position and starts the measurement. At any point during the measurement, you can press the pause button if you want to pause the measurement for whatever reason, maybe to check the white-light stability. Note it can take a few moments for the pause to activate because the program needs to complete the current measurement before the pause can take effect, so please don't press the button multiple times. You will know when the system is paused because a dialogue box will appear indicating that you can press okay when you ready to continue with the experiment. Once the experiment has finished you can access the saved data in the desktop data folder, under pump-probe data.

A.3 Delay line and UI

A.3.1 Delay-Line Basics

Before using the system please familiarize yourself with these major components of the delay-line system:

Stepper motor - The stepping motor (model: 5704X-02, manufactured by Lin Engineering) is a 2-phase bipolar stepping motor which has a stepping angle of 0.45 degrees per full-step. One full shaft rotation (360 degrees) will be made after 800 full-steps.

Motor driver- The motor driver is the brain of the delay line and controls the motor. The motor driver is responsible for controlling parameters such as the stepping speed (velocity), driving current, micro-stepping value and most importantly configuring the limit switches. The driver is supplied by Synertronic designs© , for a complete `Uragan` user manual please use this link: http://www.synertronic.co.za/data/uragan-u/Uragan-u-Manual.pdf.

Mechanical limit switches - The limit switches are very important because they tell the motor to stop once it has reached the end/start of the delay-stage (platform on which the retro-reflector moves). Without a limiting switch, the motor has no way of knowing that is has reached the end of the track and will cause serious damage to the equipment!

Worm drive - The drive train is the mechanical drive which transforms the rotational drive of the motor shaft to a linear motion. In our system, the worm drive is in a 1:1 configuration which means that we are not using

gears to step up/down the rotational-linear motion. Put simply, if the shaft rotates 10 mm around its axis then the delay platform will move 10mm forward/back.

A.3.2 Setting up and connecting the delay-line to PC

At this stage, you should be aware that the pump-probe experiment has been built so that the user can switch between the older `ExciPro` and the newer `Uragan` detection systems. In order to connect the delay-line to the new system, the following procedure must be followed exactly and in the correct order.

Switching from the `ExciPro` to the `Uragan` driver

Before using the delay-line, first, make sure that the stepper motor and the limiting switches are connected to the `Uragan` driver controller unit.

Step 1. Open the black lid covering the set-up and remove the white metal plate on the side of the delay line so that you have easy access to the cables located near the motor.

Step 2. You should have a clear view of two sets of Molex connectors which are connected and two other unconnected Molex connectors.

Step 3. The Molex connectors for the limit switches are marked with a pink colour and the stepper motor has a green coloured mark.

Step 4. Disconnect both sets of Molex clips.

Step 5. Reconnect the limit switch connector to the previously unconnected pink Molex clip.

Step 6. Reconnect the stepper motor to the previously unconnected green clip.

Step 7. CHECK! At this stage, all the cables coming out of the small black box on top of the delay-line should be completely unconnected, and the two sets of cables coming from the `Uragan` device should be connected (green-green and pink-pink).

Step 8. CHECK! Make sure that the delay stage is not already touching the start limit switch, you should see some space between the stage and the switch. If they are in contact then you must turn the dial, on the side of the delay line, so that you manually move the stage until you see at least 1 cm of free space between the switch and the stage. (this is only important for the first time you reconnect the system)

A.3.3 Connecting `Uragan` driver to the PC

The `Uragan` stepper controller communicates to the PC via a USB connection. There is a central USB 3.0 hub which links the controller to the PC.

Step 1. Make sure that a USB cable is connected to the `Uragan` controller and the USB hub.

Step 2. Make sure that the USB hub is connected to the PC.

Step 3. At the USB hub, press the `Delay Line` power button.

Step 4. Once a connection is made, the `Uragan` device will momentarily flash a green LED and then disappear.

A.3.4 Calibration

Calibrating the delay line is necessary each time you configure the set-up (switch over from `ExciPro`), this is because the `Uragan` is unable to track the absolute position of the `ExciPro` system, so when you launch the UI it will assume that you are at the position where you left off previously (which is incorrect). To calibrate is simple. Once the UI is completely open, the display might show an arbitrary number but ignore this (it is the previously stored position), press the `Home` button and wait for a dialogue box to notify that the delay is homed. Once the notice appears press `Okay`. The delay is now calibrated and the display should now read 0.0000. The system is now calibrated.

A.3.5 UI buttons

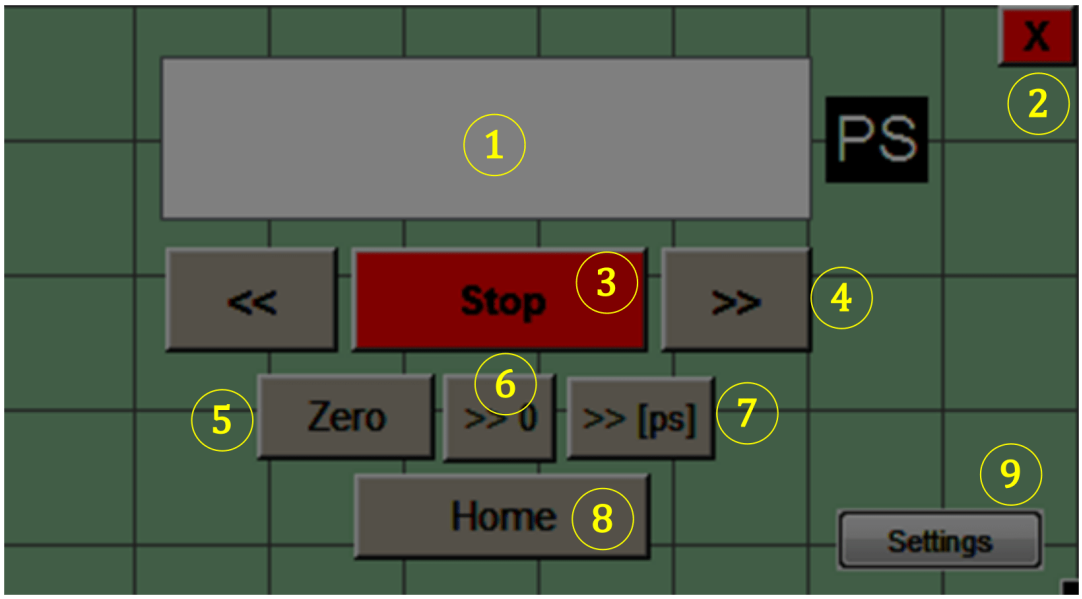

FIGURE A.1: Delay-line UI buttons.

①.Display — Shows the position of the delay-line in units of picoseconds.

②.Exit - Closes the program and saves the absolute position. DO NOT use the general exit button as this will not save the absolute position and you will have to re-calibrate the delay the next time you use it.

③.Stop - Stops the delay-line when in motion.

④.Forward/Backward – Moves the delay-line forward/backwards by an increment step. (default step size is 10 ps).

⑤.Zero – Set the current position as zero. The display will automatically be reset.

⑥.Move To Zero – Moves the delay line to the zero set position.

⑦.Move to - Moves the delay line to the specified picosecond value (relative to the location of zero).

⑧.Home – Moves the delay-line into the start position.

⑨.Settings – Change the picosecond step size from the default setting to any another value (integer).

Bibliography

[1] James P. Mulligan, *Carbon Dioxide Emissions Energy policies, politics and prices* (Nova Science Publishers, 2010), p. 160.

[2] M. Laine, *Managing without Growth: Slower by Design, Not Disaster*, Vol. 31, 1 (Edward Elgar Publishing, 2011), pp. 105–106.

[3] A. J. Cavallo, "Hubbert's petroleum production model: an evaluation and implications for World Oil Production Forecasts", Natural Resources Research **13**, 211–221 (2004).

[4] J. P. Dorian, H. T. Franssen, and D. R. Simbeck, "Global challenges in energy", Energy Policy **34**, 1984–1991 (2006).

[5] R. Buick, "When did oxygenic photosynthesis evolve?", Philosophical Transactions of the Royal Society B: Biological Sciences **363**, 2731–2743 (2008).

[6] R. E. Blankenship, "Early Evolution of Photosynthesis", PLANT PHYSIOLOGY **154**, 434–438 (2010).

[7] A. F. Collings, and C. Critchley, *Artificial photosynthesis: from basic biology to industrial application*, Vol. 91 (Wiley & Sons, Incorporated, 2005), pp. 399–404.

[8] D. J. Griffiths, *Introduction to Electrodynamics*, 3rd, Vol. 73, 6 (Pearsons Education Inc, San Francisco, June 1997), pp. 1–69.

[9] D. H. Bailey, and P. N. Swarztrauber, "A Fast Method for the Numerical Evaluation of Continuous Fourier and Laplace Transforms", SIAM Journal on Scientific Computing **15**, 1105–1110 (1994).

[10] J.-C. Diels, and W. Rudolph, *Ultrashort Laser Pulse Phenomena*, 2nd (Elsevier, 2006) Chap. 1, pp. 623–624.

[11]W. S. Steven, "The scientist and engineer's guide to digital signal processing", California Technical Pub **23**, 392–394 (1997).

[12]M. Born, and E. Wolf, *Principle of optics: Electromagnetic Theory of Propagation, Interference and Diffraction of Light*, Vol. 301 (1983), p. 257.

[13]N. Zettili, *Quantum Mechanics: Concepts and Applications*, 2nd (John Wiley & Sons, Ltd, 2009).

[14]R. Berera, R. van Grondelle, and J. T. M. Kennis, "Ultrafast transient absorption spectroscopy: principles and application to photosynthetic systems", Photosynthesis Research **101**, 105–118 (2009).

[15]D. A. McQuarrie, and J. D. S. P. Chemystry, *A molecular approach* (University Science Books, 1997), p. 1270.

[16]E. R. G. Govindjee, "Photosynthesis", in *Photosynthesis* (Wiley & Sons, Incorporated, 1969) Chap. 10.

[17]A. J. W. G. Visser, and O. J. Rolinski, "Basic photophysics", Wageningen University & Research (2010).

[18]M. Mischenko, L. Travis, and A. Lacis, "Scattering, absorption, and emission of light by small particles", NASA Goddard Institute for Space Studies, 1–128 (2002).

[19]T. G. Mayerhöfer, H. Mutschke, and J. Popp, "Employing Theories Far beyond Their Limits-The Case of the (Boguer-) Beer-Lambert Law", ChemPhysChem **17**, 1948–1955 (2016).

[20]N. Bohr, "XXXVII. On the constitution of atoms and molecules", The London, Edinburgh, and Dublin Philosophical Magazine and Journal of Science **26**, 476–502 (1913).

[21]R. C. Hilborn, "Einstein coefficients, cross sections, f values, dipole moments, and all that", American Journal of Physics **50**, 982–986 (1982).

[22]A. Einstein, "Strahlungs-emission und absorption nach der quantentheorie", Deutsche Physikalische Gesellschaft **18**, 318–323 (1916).

[23]J. McEwen, "Jablonski diagram", physical chemistry, 10 (2016).

[24]P. T. So, and C. Y. Dong, "Fluorescence Spectrophotometry", Encyclopedia of Life Sciences, 1–4 (2001).

[25]H. H. Jaffe, and A. L. Miller, "The fates of electronic excitation energy", Journal of Chemical Education **43**, 469 (1966).

[26]P. N. Off, V. Relaxation, I. Conversion, I. Crossing, T. Scale, and O. Links, "Jablonski diagram", 1–7 (2011).

[27]D. Gust, T. A. Moore, and A. L. Moore, "Molecular Mimicry of Photosynthetic Energy and Electron Transfer", Accounts of Chemical Research **26**, 198–205 (1993).

[28]J. G. Vos, R. J. Forster, and T. E. Keyes, *Interfacial Supramolecular Assemblies* (John Wiley & Sons, Ltd, 2003), pp. 10–21.

[29]R. Pyati, and M. M. Richter, "ECL - Electrochemical luminescence", Annual Reports on the Progress of Chemistry - Section C **103**, 12–78 (2007).

[30]D. M. Guldi, "Fullerene–porphyrin architectures; photosynthetic antenna and reaction center models", Chemical Society Reviews **31**, 22–36 (2002).

[31]A. Rivadossi, G. Zucchelli, F. M. Garlaschi, and R. C. Jennings, "Light Absorption by the Chlorophyll a–b Complexes of Photosystem II in a Leaf with Special Reference to LHCII", Photochemistry and Photobiology **80**, 492 (2004).

[32]M. E. El-Khouly, O. Ito, P. M. Smith, and F. D'Souza, "Intermolecular and supramolecular photoinduced electron transfer processes of fullerene-porphyrin systems", Journal of Photochemistry and Photobiology C: Photochemistry Reviews **5**, 79–104 (2004).

[33] Alsosaid1987, *Wikipedia Image: Porphyrin*, 2017.

[34]I. Okura, *Photosensitization of Porphyrins and Phthalocyanines* (Gordon and Breach publishers, Amsterdam, 2000), pp. 45–51.

[35]J. H. Wang, "Porphyrins and Metalloporphyrins", in *The yale journal of biology and medicine*, Vol. 37, 2 (Elsevier, 1964) Chap. Chapter 1, p. 170.

[36]G. Brinkmann, and A. W. Dress, "A Constructive Enumeration of Fullerenes", Journal of Algorithms **23**, 345–358 (1997).

[37]T. W. Ebbesen, K. Tanigaki, and S. Kuroshima, "Excited-state properties of C60", Chemical Physics Letters **181**, 501–504 (1991).

[38]M. H. Yun, J. W. Kim, S. Y. Park, D. S. Kim, B. Walker, and J. Y. Kim, "High-efficiency, hybrid Si/C_60 heterojunction solar cells", Journal of Materials Chemistry A **4**, 16410–16417 (2016).

[39]Y.-B. Wang, and Z. Lin, "Supramolecular Interactions between Fullerenes and Porphyrins", Journal of the American Chemical Society **125**, 6072–6073 (2003).

[40]M. M. Olmstead, D. A. Costa, K. Maitra, B. C. Noll, S. L. Phillips, P. M. Van Calcar, and A. L. Balch, "Interaction of Curved and Flat Molecular Surfaces. The Structures of Crystalline Compounds Composed of Fullerene (C_60 , C_60 O, C_70 , and C_120 O) and Metal Octaethylporphyrin Units", Journal of the American Chemical Society **121**, 7090–7097 (1999).

[41]I. R. Gould, R. Moody, and S. Farid, "Electron-transfer reactions in the Marcus inverted region: differences in solvation and electronic coupling between excited charge-transfer complexes and geminate radical ion pairs", Journal of the American Chemical Society **110**, 7242–7244 (1988).

[42]M. Lorenc, M. Ziolek, R. Naskrecki, J. Karolczak, J. Kubicki, and A. Maciejewski, "Artifacts in femtosecond transient absorption spectroscopy", Applied Physics B: Lasers and Optics **74**, 19–27 (2002).

[43]E. Riedle, M. Beutter, S. Lochbrunner, J. Piel, S. Schenkl, S. Spörlein, and W. Zinth, "Generation of 10 to 50 fs pulses tunable through all of the visible and the NIR", Applied Physics B: Lasers and Optics **71**, 457–465 (2000).

[44]N. V. Tkachenko, "Steady State Absorption Spectroscopy", Optical Spectroscopy: Methods and Instrumentations **Chapter 5**, 89–106 (2006).

[45]J. J. Snellenburg, S. P. Laptenok, R. Seger, K. M. Mullen, and I. H. M. van Stokkum, "Glotaran : A Java -Based Graphical User Interface for the R Package TIMP", Journal of Statistical Software **49**, (2012).

[46]D. Zigmantas, Y. Ma, E. Read, and G. Fleming, "Nonlinear Femtosecond Optical Spectroscopy Techniques in Photosynthesis", in *... techniques in photosynthesis* (2008) Chap. 11, pp. 201–222.

[47] Nikolai V. Tkachenko, "Optical Spectroscopy", in *Book*, 1st Editio (2005) Chap. 2.

[48]P. J. Campagnola, and C. Y. Dong, "Second harmonic generation microscopy: Principles and applications to disease diagnosis", Laser and Photonics Reviews **5**, 13–26 (2011).

[49]M. Bradler, P. Baum, and E. Riedle, "Femtosecond continuum generation in bulk laser host materials with sub-μJ pump pulses", Applied Physics B: Lasers and Optics **97**, 561–574 (2009).

[50]A. M. Weiner, R. H. Stolen, and J. P. Heritage, "Self-phase modulation and optical pulse compression influenced by stimulated Raman scattering in fibers", Journal of the Optical Society of America B **5**, 364 (1988).

[51]K. Ekvall, P. Van Der Meulen, C. Dhollande, L. E. Berg, S. Pommeret, R. Naskrecki, and J. C. Mialocq, "Cross phase modulation artifact in liquid phase transient absorption spectroscopy", Journal of Applied Physics **87**, 2340–2352 (2000).

[52]B. Herman, M. J. Parry-Hill, and I. D. Johnson, *Fluorescence Microscopy Interactive Tutorials: Photobleaching*, 2003.

[53]I. Clark-MXR, *CPA-Series Fiber-seeded Ultrashort Pulse Ti:Sapphire Regenerative Amplifier*, tech. rep. (2018), pp. 1–2.

[54]J.-y. Zhang, J. Y. Huang, H. Wang, K. S. Wong, and G. K. Wong, "Second-harmonic generation from regeneratively amplified femtosecond laser pulses in BBO and LBO crystals", Journal of the Optical Society of America B **15**, 200 (1998).

[55]F. Montiel, L. Fomina, and S. Fomine, "Charge transfer complexes of fullerene with porphyrins as molecular rectifiers. A theoretical study", Journal of Molecular Modeling **21**, 1–8 (2015).

[56]A. Cid, Ó. A. Moldes, M. S. Diniz, B. Rodríguez-González, and J. C. Mejuto, "Redispersion and Self-Assembly of C 60 Fullerene in Water and Toluene", ACS Omega **2**, 2368–2373 (2017).

[57] J. E. Falk, "Porphyrins and Metalloporphyrins: A New Edition Based on the Original Volume", in *Porphyrins and metalloporphyrins* (Elsevier Scientific Publishing Company, 1975), p. 590.

[58] Varian Cary, *Varian Cary 100 bio User Manual*, 2012.

[59] HORIBA scientific, *Fluoromax Operation Manual*, 2011.

[60]J. S. Baskin, H.-Z. Yu, and A. H. Zewail, "Ultrafast Dynamics of Porphyrins in the Condensed Phase: I. Free Base Tetraphenylporphyrin †", The Journal of Physical Chemistry A **106**, 9837–9844 (2002).

[61]R. R. Valiev, E. G. Ermolina, R. T. Kuznetsova, V. N. Cherepanov, and D. Sundholm, "Computational and experimental studies of the electronic excitation spectra of EDTA and DTPA substituted tetraphenylporphyrins and their Lu complexes", Journal of Molecular Modeling **19**, 4631–4637 (2013).

[62]D. M. Guldi, and M. Prato, "Excited-State Properties of C 60 Fullerene Derivatives", Accounts of Chemical Research **33**, 695–703 (2000).

[63]R. P. Steer, "Concerning correct and incorrect assignments of Soret (S_2 –S_0) fluorescence in porphyrinoids: a short critical review", Photochem. Photobiol. Sci. **13**, 1117–1122 (2014).

[64]H. Z. Yu, J. S. Baskin, and A. H. Zewail, "Ultrafast dynamics of porphyrins in the condensed phase: II. Zinc tetraphenylporphyrin", Journal of Physical Chemistry A **106**, 9845–9854 (2002).

[65]M. Uttamlal, and A. Sheila Holmes-Smith, "The excitation wavelength dependent fluorescence of porphyrins", Chemical Physics Letters **454**, 223–228 (2008).

[66]J. M. D.K. Palit, A.V. Sapre, "Photophysical properties of the fullerenes, C_60 and C_70", Journal of the American Chemical Society **195** (1992).

[67]J. W. Arbogast, A. P. Darmanyan, C. S. Foote, F. N. Diederich, R. L. Whetten, Y. Rubin, M. M. Alvarez, and S. J. Anz, "Photophysical properties of sixty atom carbon molecule (C60)", The Journal of Physical Chemistry **95**, 11–12 (1991).

[68]D. M. Guldi, and M. Prato, "Excited-State Properties of C_60 Fullerene Derivatives", Accounts of Chemical Research **33**, 695–703 (2000).

[69]A. F. Benedetto, and R. Weisman, "Unusual triplet state relaxation in C60 oxide", Chemical Physics Letters **310**, 25–30 (1999).

[70]M. Fujitsuka, C. Luo, O. Ito, Y. Murata, and K. Komatsu, "Triplet Properties and Photoinduced Electron-Transfer Reactions of C 120 , the [2+2] Dimer of Fullerene C 60", The Journal of Physical Chemistry A **103**, 7155–7160 (1999).

[71]S. K. Das, B. Song, A. Mahler, V. N. Nesterov, A. K. Wilson, O. Ito, and F. D'Souza, "Electron Transfer Studies of High Potential Zinc Porphyrin–Fullerene Supramolecular Dyads", The Journal of Physical Chemistry C **118**, 3994–4006 (2014).

[72]M. E. El-Khouly, O. Ito, P. M. Smith, and F. D'Souza, "Intermolecular and supramolecular photoinduced electron transfer processes of fullerene–porphyrin systems", Journal of Photochemistry and Photobiology C: Photochemistry Reviews **5**, 79–104 (2004).

[73]A. M. Weiner, D. E. Leaird, J. S. Patel, and J. R. Wullert, "Programmable femtosecond pulse shaping by use of a multielement liquid-crystal phase modulator.", Opt Lett **15**, 326 (1990).